12-2014

Automated Doppler Broadening of Cross Sections for Neutron Transport Applications

Shane William Daniel Hart
University of Tennessee - Knoxville, shart6@vols.utk.edu

To the Graduate Council:

I am submitting herewith a dissertation written by Shane William Daniel Hart entitled "Automated Doppler Broadening of Cross Sections for Neutron Transport Applications." I have examined the final electronic copy of this dissertation for form and content and recommend that it be accepted in partial fulfillment of the requirements for the degree of Doctor of Philosophy, with a major in Nuclear Engineering.

G. Ivan Maldonado, Major Professor

We have read this dissertation and recommend its acceptance:

Ondrej Chvala, Steve E. Skutnik, Robert Grzywacz

Accepted for the Council:
Carolyn R. Hodges

Vice Provost and Dean of the Graduate School

(Original signatures are on file with official student records.)

12-2014

Automated Doppler Broadening of Cross Sections for Neutron Transport Applications

Shane William Daniel Hart
University of Tennessee - Knoxville, shart6@vols.utk.edu

To the Graduate Council:

I am submitting herewith a dissertation written by Shane William Daniel Hart entitled "Automated Doppler Broadening of Cross Sections for Neutron Transport Applications." I have examined the final electronic copy of this dissertation for form and content and recommend that it be accepted in partial fulfillment of the requirements for the degree of Doctor of Philosophy, with a major in Nuclear Engineering.

G. Ivan Maldonado, Major Professor

We have read this dissertation and recommend its acceptance:

Ondrej Chvala, Steve E. Skutnik, Robert Grzywacz

Accepted for the Council:
Carolyn R. Hodges

Vice Provost and Dean of the Graduate School

(Original signatures are on file with official student records.)

Automated Doppler Broadening of Cross Sections for Neutron Transport Applications

A Dissertation Presented for the

Doctor of Philosophy

Degree

The University of Tennessee, Knoxville

Shane William Daniel Hart

December 2014

Acknowledgements

There are many people to whom I wish to express my sincere gratitude. Their invaluable aid during my doctoral studies allowed me to navigate and arrive at the dissertation I have today.

Foremost of all I would to thank my advisor Dr. G. Ivan Maldonado, who took a chance on me when I strolled into his office at the university back in April 2008. I would also like to thank my dissertation committee: Dr. Steven Skutnik, Dr. Ondrej Chvala, and Dr. Robert Grzywacz for their support and assistance.

There are a large number of people who helped me during my research at Oak Ridge National Laboratory, even with their demanding and busy schedules. Dr. Cihangir Celik served as a mentor of sorts, and helped give me direction and focus. Dr. Dorothea Wiarda assisted me greatly whenever I ran into trouble using the AMPX code package. Dr. Bradley Rearden, the current leader of the SCALE program, came through with support for me and an interesting project that turned into my dissertation. I would also like to thank Dr. Mark Williams, Dr. Kursat Bekar, and Dr. Bryan Broadhead at ORNL for their help with my work.

I would also like to thank those compatriots of mine who graduated before me: Dr. Brenden Mervin and Dr. James Banfield; letting me watch them go through this process has aided me greatly. Others in the "student room" at ORNL, including Dr. Chris Perfetti, have also provided assistance and light-hearted discussions when needed. Special thanks go out to Carole Zasowski for suffering through reading this dissertation and offering her insight and corrections.

Finally, and most importantly, I would like to thank my family for their continuous support. I will always remember the incredulous voice and face of my mother, Pamela Peterson, when I told her I was going back to school.

Abstract

This dissertation discusses the research and development of new cross section temperature handling techniques for the SCALE computer code, which is developed and maintained at Oak Ridge National Laboratory. In particular, methods will be added to the KENO Monte Carlo code.

Areas of interest include: neutron scattering off of heavy isotopes in the epithermal energy range, implementation of Doppler pre-broadening of continuous energy one-dimensional cross-section data, implementation of interpolation on the continuous energy two-dimensional cross sections, and implementation of the direct $S(\alpha, \beta)$ [S alpha beta] method for thermal neutron scattering and interpolation on that data.

Accurate cross section scattering off of heavy isotopes is crucial for accurate neutronics modeling and simulation of actual reactor cores during operational conditions. Scattering off of heavy isotopes such as ^{238}U [Uranium 238] will have a greater impact on core neutronics behavior as reactor temperatures increase. Ensuring that the cross-section data used by Monte Carlo codes is obtained at the correct temperature will allow more accurate modeling of operating reactors that do not operate at current cross-section library temperatures.

A review of the current approaches used for scattering and Doppler broadening was performed, and the current limitations of these approaches were examined. By examining the limitations of current approaches, new methods were developed and implemented into KENO. First, the Doppler Broadened Rejection Correction algorithm was added to KENO to allow for more accurate scattering off of heavy

isotopes. Next, a methodology allowing for accurate cross section pre-broadening of all cross section types was developed and implemented. Finally, as a comparison against existing and new, the direct $S(\alpha, \beta)$ method was implemented into KENO.

To test the impact of the new methods, a large variety of test cases were run and unit tests showcasing the relevant coding sections were developed. These test cases are representative of cases that will be encountered during production code operation and will serve as good examples of the new functionality going forward. In addition, a select number of benchmarks from the Criticality and Reactor Physics Handbooks were selected to verify that the additions to the KENO code were accurate.

Table of Contents

1 Introduction **1**

1.1 Organization of Dissertation 1

1.2 Objective 2

1.3 Motivation 5

2 Background **6**

2.1 Cross Sections 6

2.2 Doppler Broadening 9

2.3 Continuous Energy Cross-Section Libraries 11

2.3.1 Collision Probabilities 11

2.3.2 Probability Tables 12

2.4 Resonance Processing 13

2.4.1 Bondarenko Method 14

2.4.2 Pointwise Solution Method 16

2.5 Radiation Transport Theory 17

2.6 Thermal Neutron Scattering 20

2.6.1 Double Differential Scattering Cross Section 20

2.6.2 Calculation of the Thermal Neutron Spectra 23

2.7 Monte Carlo 24

2.7.1 Probability Functions 25

2.7.2 Analog Simulation of Neutron Transport 26

2.7.3 Statistical Estimation and Variance Reduction 28
2.7.4 Tallies 30
2.7.5 Criticality Problems 31
2.8 KENO 31
2.8.1 Transport Equation 32
2.8.2 Collision Site Selection and Treatment 33
2.8.3 KENO Scattering Selection 35
2.8.4 Thermal Scattering Effects in KENO 37

3 Literature Review and Previous Research 40
3.1 Development of a New Scattering Kernel 40
3.2 Development of the DBRC Method 42
3.3 Improving Multigroup results using DBRC 44
3.4 One-Dimensional Doppler Broadening 46
3.5 Kinematics Doppler Broadening 48

4 Doppler Broadened Rejection Correction Method 50
4.1 Free Gas Thermal Treatment 51
4.1.1 Sampling the Velocity of the Target Nucleus 51
4.1.2 Doppler Broadened Rejection Correction 54
4.2 Implementation into KENO 55
4.2.1 read_pointwise 56
4.2.2 nuclide_type 57
4.2.3 sample_reaction 57
4.2.4 sample_freegas 57
4.3 Results 57
4.3.1 Becker LWR Pin Cell 58
4.3.2 CASL LWR Pin Cell 60
4.3.3 CANDU Bundle 64
4.3.4 Mosteller Benchmark 67

5 One-Dimensional Problem Dependent Doppler Broadening 71

5.1 Finite Difference Method for Doppler Broadening 72

5.1.1 Correcting Limitations 73

5.2 Probability Tables 76

5.3 Implementation into KENO 78

5.3.1 Modifications to Existing Routines 78

5.3.2 New Routines 80

5.4 Results 81

5.4.1 CASL Pin Cell 82

5.4.2 Radial and Axial Temperature Effects 83

5.4.3 3D Assembly 85

5.4.4 Aluminum Infinite Homogeneous Model 86

6 Two-Dimensional Problem Dependent Doppler Broadening 89

6.1 Interpolation Method on Double Differential Probability Data 90

6.1.1 Implementation into KENO 92

6.1.2 Results 93

6.2 Interpolation Method on $S(\alpha, \beta)$ Data 99

6.2.1 Implementation into KENO 99

6.2.2 Results 102

7 Direct $S(\alpha, \beta)$ Scattering Implementation 105

7.1 Direct $S(\alpha, \beta)$ Method 105

7.1.1 Interpolation on $S(\alpha, \beta)$ CDFs 109

7.2 Implementation 109

7.2.1 Creation of α and β CDFs 109

7.2.2 Implementation into KENO 111

7.3 Results 113

7.3.1 Scattering Results 114

7.3.2 KENO Results 118

8 Benchmark Calculations **126**

8.1 Criticality Safety Benchmarks 127

8.1.1 LEU-COMP-THERM-078 Evaluation 127

8.1.2 LEU-COMP-THERM-026 Evaluation 129

8.2 Reactor Physics Benchmarks 133

8.2.1 KRITZ-LWR-RESR-001 Evaluation 133

8.2.2 KRITZ-LWR-RESR-002 Evaluation 135

9 Conclusions **150**

9.1 Summary of Conclusions 150

9.2 Suggestions for Future Work 152

References **154**

Appendix **161**

A S$\alpha\beta$RE Binary File Format 162

Vita **163**

List of Tables

2.1 ENDF thermal scattering law data 38

3.1 Capture reaction rates of LWR pin cell at 1200 K 44
3.2 Upscatter percentage at 1000 K 46
3.3 Reactivity effect of exact scattering kernel 46

4.1 DBRC - Temperature Results 60
4.2 DBRC Extra Istopes Results 62
4.3 DBRC Results for CASL Pin Cell 62
4.4 DBRC Results for Depleted CASL Pin Cell 63
4.5 Mosteller Benchmark UO_2 Results 69

5.1 Eigenvalue results for pin cell depletion at different temperatures. . . 83
5.2 Eigenvalue results for pin cell with different radial temperatures. . . . 84
5.3 Eigenvalue results for pin cell with different axial and radial temperatures. 86
5.4 3D assembly problem-dependent Doppler broadening results. 86
5.5 Infinite homogeneous aluminum model results. 88

7.1 Timing results for direct $S(\alpha, \beta)$ cases. 124
7.2 Size of library for direct $S(\alpha, \beta)$. 124

8.1 Benchmark results LEU-COMP-THERM-078 ($\sigma = 0.0002$). 129
8.2 Sample calculation results LEU-COMP-THERM-026. 130

8.3 Sample calculation results LEU-COMP-THERM-026 (with direct $S(\alpha, \beta)$). 133
8.4 Experimental, Measured, and Benchmark-model k_{eff} for KRITZ-LWR-RESR-001. 136
8.5 Benchmark results for KRITZ-LWR-RESR-001. 137
8.6 Fission rates (from benchmark and calculated) normalized to rod (14,14) for KRITZ-LWR-RESR-001 cold case. 138
8.7 Fission rates (from benchmark) normalized to rod (14,14) for KRITZ-LWR-RESR-001 hot case. 139
8.8 Fission rates (calculated) normalized to rod (14,14) for KRITZ-LWR-RESR-001 hot case. 140
8.9 Experimental, Measured, and Benchmark-model k_{eff} for KRITZ-LWR-RESR-002. 142
8.10 Benchmark results for KRITZ-LWR-RESR-002. 143
8.11 Fission rates (from benchmark) normalized to rod (22,23) for KRITZ-LWR-RESR-002 hot case. 148
8.12 Fission rates (calculated) normalized to rod (22,23) for KRITZ-LWR-RESR-002 hot case. 149

A.1 Data file format for S$\alpha\beta$RE binary file. 162

List of Figures

2.1 An Example of Cross Sections and Energy Dependence 7
2.2 Example of Doppler Broadening 10
2.3 Probability Tables 13
2.4 Resonance Self-Shielding Effects 15
2.5 Cross-section hierarchy for particle interactions in KENO. [1] 34
2.6 Interpolation diagram for secondary angle-energy data. 39

3.1 A plot of the first six Legendre moments computed by Arbanas compared to those via the Monte Carlo method. 43

4.1 Routines for cross section preparation and collisions in KENO. 56
4.2 DBRC algorithm in KENO. 58
4.3 LWR Pin Cell (NEWT). 59
4.4 DBRC KENO results. 61
4.5 DBRC KENO results for CASL Pin Cell. 64
4.6 CANDU 1/4 Bundle. 65
4.7 Multi Group DBRC Steps. 66
4.8 CANDU - DBRC depletion results. 67
4.9 Mosteller fuel pin. 69
4.10 Doppler defect for Mosteller UO_2 Benchmark. 70

5.3 Differences in ^{16}O σ_t cross sections with new and old methods. 75
5.4 Differences in ^{1}H σ_t cross sections with new and old methods. 77

5.5 Cross-section processing routines. 79

6.1 Interpolation between two-dimensional panels. 91
6.2 2D interpolation results from CASL pin cell (hydrogen in water). . . 95
6.3 2D interpolation results from CASL pin cell (water). 96
6.4 Bragg edges in graphite. 97
6.5 2D interpolation results from graphite sphere. 100
6.6 2D interpolation results from polyethylene sphere. 101
6.7 2D interpolation results on $S(\alpha, \beta)$ for CASL pin cell. 103
6.8 2D interpolation results on $S(\alpha, \beta)$ for graphite sphere. 104

7.1 Program flow of S$\alpha\beta$RE. 110
7.2 Neutron scattering off of hydrogen in water at $E_{\text{in}} = 1$ eV, $T = 450$ K. 115
7.3 Neutron scattering off of hydrogen in water at $E_{\text{in}} = 0.01$ eV, $T = 450$ K. 116
7.4 Neutron scattering off of hydrogen in water at $E_{\text{in}} = 9$ eV, $T = 450$ K. 117
7.5 Neutron scattering off of graphite at $E_{\text{in}} = 0.001$ eV, $T = 700$ K. . . 119
7.6 Neutron scattering off of graphite at $E_{\text{in}} = 1$ eV, $T = 700$ K. 120
7.7 Neutron scattering off of graphite at $E_{\text{in}} = 3$ eV, $T = 700$ K. 121
7.8 Direct $S(\alpha, \beta)$ results for CASL pin cell (water). 122
7.9 Direct $S(\alpha, \beta)$ results for graphite sphere. 125

8.1 Cut-away view of the critical assembly core tank (case two) for LEU-COMP-THERM-078. 128
8.2 Configuration of the critical assembly for LEU-COMP-THERM-26 (dimensions in mm). 131
8.3 KENO 3D representation of case two for evaluation LEU-COMP-THERM-026. 132
8.4 KENO 3D of bottom of fuel pins for LEU-COMP-TERM-026 case two. 136
8.5 Schematic top view of the KRITZ-2:19 core. 141

8.6 Numbering of the fuel-rod columns and rows for the KRITZ-2:19 core. 144
8.7 Schematic top view of the KRITZ-2:1 core. 145
8.8 Cut-away of KRITZ-2:1 core done in KENO 3D. 146
8.9 Numbering of the fuel-rod columns and rows for the KRITZ-2:1 core. 147

Chapter 1

Introduction

Chapter 1 provides an overview of the research documented in this dissertation. The following sections describe the organization of this document, the overall objectives of this research, and the motivation behind the research presented within this manuscript.

1.1 Organization of Dissertation

The first chapter, Chapter 1, is an introductory chapter which describes the objectives and motivation for this research. Chapter 2 presents a background of relevant methodologies and equations in order to give the reader a brief understanding of the theory behind this dissertation. Topics covered include neutron cross sections, Doppler broadening, resonance processing, radiation transport theory, neutron thermal scattering, and a quick overview of Monte Carlo transport codes. A short overview of the codes used in this dissertation is also presented.

Chapter 3 builds on the material from Chapter 2 by presenting the reader with current research on the topics to be covered in this dissertation. Papers and research that have been presented at recent conferences and in recent journals indicate the direction in which the pertinent field the research is moving, and how it relates to

the topics of this dissertation. Older literature is included when it is relevant to the discussion, but the focus is placed upon current research on related topics.

The next chapter, Chapter 4, discusses the implementation of the Doppler Broadened Rejection Correction (DBRC) method into the KENO computer code. Theory behind the DBRC method is presented, and how it integrates into the KENO computer code is explained. Results given from using the code with the DBRC method enabled are shown and discussed, and future steps to improve the efficiency of the DBRC method are mentioned.

Chapters 5 and 6 discuss the implementation of Doppler broadening one-dimensional and two-dimensional (kinematics) data, respectively. Equations and theory behind the methods are explained, and results are shown and discussed showing the impact of the more accurate cross sections on various models. To further improve the accuracy of the two-dimensional Doppler broadening, Chapter 7 discuses the implementation of a direct $S(\alpha, \beta)$ method for thermal neutron scattering in KENO.

Chapters 8 demonstrates the accuracy of the methods herein described by modeling some common benchmark problems from international evaluation handbooks. In particular, the KRITZ reactor is chosen because of the availability of elevated temperature results with which to compare the developed Doppler broadening methodology. Other critical systems are also benchmarked, with an emphasis on those that are at a temperature that currently doesn't exist in the SCALE cross-section libraries.

This document is concluded, in Chapter 9, with an assessment of the progress towards the initial goals set out by this research and proposes a path moving forward.

1.2 Objective

The overall goal of this research is to improve the accuracy of Monte Carlo-based neutronics for a wide variety of problems. The problems addressed in particular are:

- Addressing assumptions in the scattering of neutrons off of heavy isotopes such as ^{238}U,
- The inability of code developers to ship every cross-section library at every possible temperature, and therefore the inability of the user to select an arbitrary temperature at which to run their problem.

For scattering of neutrons off of target nuclei, there have typically been two approaches:

1. For thermal moderators, use $S(\alpha, \beta)$ tables that have been created that give data on scattering to certain angles and energies,
2. for other isotopes, create a thermal distribution using a free gas approximation that assumes that a material can be modeled as a free or proton gas in thermal equilibrium at some temperature.

It is this second approach that is currently used for the majority of isotopes, including heavy isotopes such as ^{238}U. Most Monte Carlo codes sample from this free gas approximation and make the assumption that the scattering cross section doesn't vary with energy. For isotopes with strong resonances, this assumption can be proven to be invalid and further sampling must be done. The approach implemented into KENO is discussed further in Section 4.1.2.

Cross-section libraries shipped with Monte Carlo codes typically include some small number of temperatures. This is, for Continuous Energy (CE) codes, due to the large amount of disk space and memory required by these CE cross sections. For example, the computer code SCALE (developed at Oak Ridge National Laboratory (ORNL)) generally includes only six temperatures for most isotopes: 293K, 565K, 600K, 900K, 1200K, and 2400K. KENO uses the closest temperature to the temperature that the user selects. As can be expected, if the user picks a temperature that is some distance away from a library temperature, errors in the eigenvalue can quickly arise.

To address these issues, this research involves building the necessary infrastructure to read in the CE cross-section libraries that are available and broaden them to whatever temperature is desired by the user. Accomplishing these goals required a multistep research and development process, which included the following tasks (all implemented in KENO):

1. Researching the current methods used for On-The-Fly (OTF) Doppler broadening of 1D cross sections,
2. implementing a method of Doppler pre-broadening 1D cross sections,
3. implementing a method of Doppler pre-broadening probability table data for the unresolved resonance region,
4. development and implementation of Doppler pre-broadening the thermal moderator 2D cross-section data,
5. investigation and implementation of the direct $S(\alpha, \beta)$ method of thermal scattering and Doppler pre-broadening of the data.

Accomplishing these tasks involved developing the algorithms to accurately Doppler broaden the cross sections, as well as a framework for implementing this logic into KENO. Research was conducted to identify the common issues with other OTF Doppler broadening methods, and to develop ways to avoid some of these pitfalls in the new methodology. While work has been done previously on OTF Doppler broadening of 1D cross sections, work on broadening the thermal moderator data (typically $S(\alpha, \beta)$ data) is still in the nascent stage. In this regard, a new methodology has been developed to broaden the thermal moderator data in the format that it is found in in KENO. These algorithms are coded directly into the SCALE Monte Carlo library so that they can be used by all versions of KENO. They are coded in Fortran, with a small part coded in C++.

Eventually, KENO developers might desire to move to a "true" OTF Doppler broadening solution. This could evolve to capture advances in Graphics Processing

Unit (GPU) technology to allow for fast broadening on the GPU cores. One main draw of using OTF broadening instead of the current approach of pre-broadening is that the amount of data shipped can be greatly reduced. The current approach is to pre-broaden and interpolate from the closest two data libraries. By switching to "true" OTF one could potentially remove all data except the OTF data.

1.3 Motivation

Nuclear power is a viable and well-established technology for carbon-free energy production on a large scale. Due to the large cost and time investment of carrying out nuclear experiments, computer codes have become an increasingly important tool in the design and verification of nuclear reactor cores and other criticality experiments. Any limitations and approximations that exist in our reactor simulation tools will result in higher safety margins and less trust in computational results. By increasing the accuracy of our tools, and refining some assumptions that have been made in code development, we can improve the accuracy and trust in our results.

ORNL has been a long-time leader in the nuclear field. By developing the SCALE code package, they have created a long-standing suite of tools that can be used in a large variety of nuclear related applications. The mission of ORNL to continually improve their codes, and the funding provided by sponsors like the U.S. Department of Energy (DOE) and the US Nuclear Regulatory Commission (NRC), has led to research to improve the temperature dependency of the KENO computer code. This work aims to make more accurate results available for the whole KENO user community.

Chapter 2

Background

This chapter presents a brief background on neutron transport theory and the Monte Carlo approach to solving radiation transport problems. Particular emphasis is placed on discussing neutron cross sections and current scattering methods, as those are the areas that are improved with the research documented in this dissertation. Current approaches to Doppler broadening are also discussed.

This chapter is not intended to educate the reader completely on advanced reactor theory, but rather to provide a brief review and overview of basic theory relevant to the new methods. More information can be found in one of many related textbooks on the subjects [2–4].

2.1 Cross Sections

For accurate modeling of a complex system like a nuclear reactor, accurate data is required. An integral part of these data are the neutron cross sections. In simple terms, a neutron cross section (σ) is the probability of a nuclear reaction taking place. Cross sections are available for a variety of nuclear reactions, the most important of which are usually fission, absorption, and scattering. The units of σ are area, which help visualize the concept of σ as an effective cross sectional area presented to the neutron by the nucleus. As an example, the fission cross section (σ_f) is a measure

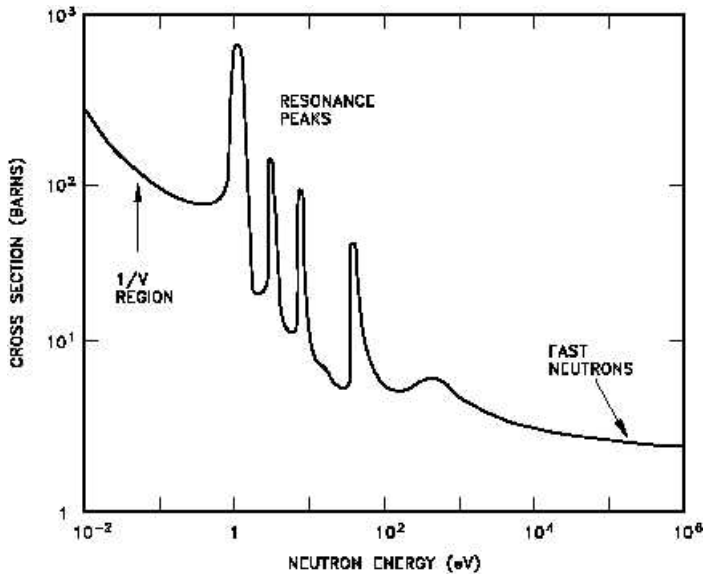

Figure 2.1: An Example of Cross Sections and Energy Dependence

of the probability that a neutron and a nucleus interact to form a compound nucleus which will then undergo fission. As shown in Figure 2.1, cross sections are dependent on energy and can vary wildly as the neutron energy changes.

Published experimental and theoretical cross sections for neutron-nuclear reactions are collected by several collaborating nuclear data agencies worldwide. This nuclear data must be evaluated before it can be used confidently in reactor physics calculations. This evaluation consists of inter-comparison of data, use of the data to calculate benchmark experiments, critical assessment of statistical and systematic errors, checks for the internal consistency and consistency with standard neutron cross sections, and the derivation of consistent preferred values by appropriate procedures. Several large evaluated nuclear data files are maintained in the U.S., such as the Evaluated Nuclear Data File (ENDF/B) at Brookhaven National Laboratory [5] and the Evaluated Nuclear Data Library (ENDL) of the Lawrence Livermore National Laboratory (LLNL). Outside of the U.S. a popular choice is the Japanese Evaluated Nuclear Data Library (JENDL), among others.

The evaluated data files contain the following data:

1. $\sigma(E_i)$ tabulated pointwise in energy at low energies below the resonance region,
2. resolved resonance parameters and background cross sections in the resolved resonance regions,
3. unresolved resonance statistical parameters and background cross sections in the unresolved resonance region,
4. $\sigma(E_i)$ are tabulated pointwise in energy at energies above the resonance region,
5. scattering transfer functions $p(E_i, \mu_s)$ are tabulated pointwise in energy and either pointwise in angle (μ_{sj}) or as Legendre coefficients.

In order to use these cross sections in neutron transport codes, work is usually done to convert the pointwise cross sections into a group format, where the energy range is usually spanned by dozens to a few hundred groups. Each energy group will then have cross sections associated with it. This is done to speed up the computationally intensive nuclear transport codes, and to lower the memory requirements needed for storing cross section data. Generally, codes which prepare multigroup libraries do so by numerically calculating integrals of the type

$$\sigma^g = \frac{\int_{E_g}^{E_{g-1}} \mathrm{d}E\, \sigma(E) W(E)}{\int_{E_g}^{E_{g-1}} \mathrm{d}E\, W(E)} \tag{2.1}$$

$$\sigma_n^{g \to g'} = \int_{E_g}^{E_{g-1}} \mathrm{d}E\, \sigma_s(E) W(E) \frac{\int_{E_{g'}}^{E_{g'-1}} \mathrm{d}E' p_n(E')}{\int_{E_g}^{E_{g-1}} \mathrm{d}E\, W(E)}, \tag{2.2}$$

where $W(E)$ is some specified weighting function (either constant, $1/E$, $\chi(E)$, etc.). Equation 2.1 is for averaging 1D cross sections, and Equation 2.2 is for averaging 2D

cross sections. Equations 2.1 and 2.2 are usually used to generate a fine- or ultra-fine group structure. Once this structure is generated, then a corresponding fine- or ultra-fine flux spectrum (ϕ) is calculated and problem dependent cross sections can be determined. This is shown in Equations 2.3 and 2.4.

$$\sigma_k = \frac{\sum_{g \in k} \sigma^g \phi_g}{\sum_{g \in k} \phi_g} \tag{2.3}$$

$$\sigma_n^{k \to k'} = \frac{\sum_{g \in k} \sum_{g' \in k} \sigma_n^{g \to g'} \phi_g}{\sum_{g \in k} \phi_g} \tag{2.4}$$

Note that resonances must be treated specially, as discussed later in this document. One code that can take evaluated nuclear data and create multigroup cross sections libraries is AMPX [6]. It generates cross section files for use with the SCALE [7] code package.

2.2 Doppler Broadening

Cross sections depend on the relative speed between the neutron and the target nucleus. Since the nuclei themselves are in thermal motion, this relative speed may be either greater or less than the neutron speed. This difference in neutron speeds gives rise to a "Doppler shift" effect in resonance cross section behavior.

The effect is that as temperature increases the resonance broadens while its peak magnitude decreases. For this reason, one frequently refers to resonance cross sections that have been averaged over the distribution of nuclear velocities as "Doppler broadened" cross sections. An example of this Doppler broadening is shown in Figure 2.2.

In 1976, Cullen and Weisbin devised a method for calculating the exact Doppler broadened cross sections [8]. One of the goals of their exact method was to ensure that, after being broadened, the cross sections were still able to be linear-linear interpolated; this was necessary because many of the codes of the time relied on that fact for their

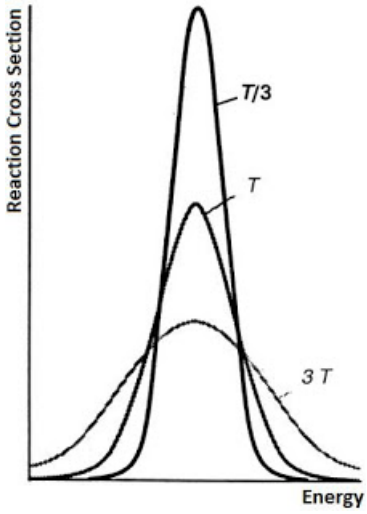

Figure 2.2: Example of Doppler Broadening

cross section processing. The exact equation developed by Cullen is:

$$\sigma(y, T_2) = \frac{1}{y^2}\frac{1}{\pi}\int_0^\infty [\sigma(x, T_1)] \times x^2\{\exp[-(x-y)^2] - \exp[-(x+y)^2]\}\,\mathrm{d}x\,, \qquad (2.5)$$

where

$$y^2 = \alpha E = \beta V^2$$
$$x^2 = \alpha E_r = \beta V_r^2$$
$$\alpha = \frac{A}{k(T_2 - T_1)}$$
$$\beta = \frac{M}{2k(T_2 - T_1)}$$

and $\sigma(y, T_2)$ and $\sigma(y, T_1)$, are the broadened and base cross sections at T_2 and T_1 respectively. The terms y and x are velocity-like and are related to the incoming neutron velocity V and the relative velocity V_r respectively.

Unfortunately, due to the presence of complementary error functions in the solution for sigma, a discretized form of this exact Doppler broadening would require

an unacceptable amount of computing time. Therefore, no modern codes have done OTF exact Doppler broadening although work is being done on approximate methods (see Sections 3.4 and 5.1).

2.3 Continuous Energy Cross-Section Libraries

Instead of integrating cross sections over different energy groups, current Monte Carlo codes usually use CE libraries. CE libraries usually contain every energy point that is available in the original raw ENDF/B data. By interpolating between the points, a cross section can be associated with any possible neutron energy. Most Monte Carlo codes ship with CE libraries in addition to any multigroup (MG) libraries. For example, SCALE ships ENDF/B-VII.0 CE and multiple MG libraries. CE libraries are usually Doppler broadened to the same temperatures as the MG libraries. In addition to the cross section data itself, the SCALE CE libraries contain some other data that is useful in Monte Carlo transport and that are quickly discussed in the sections that follow.

2.3.1 Collision Probabilities

The SCALE Monte Carlo code KENO [9] uses collision probability data to determine some of the kinematic details after a neutron has undergone a collision. The kinematic data includes speed and direction. Collision probability data is relatively straightforward, but pre-calculating and storing it on the cross-section library allows for some small time savings at the expense of memory.

There are three main types of collision probabilities shown in Equation 2.6. In addition, $(n, 2n)$ and $(n, 3n)$ reaction probabilities are also saved if those reaction

cross sections exist for a given nuclide.

$$
\begin{aligned}
P^i_{nabs}(E) &= \frac{\sigma^i_s(E)}{\sigma^i_t(E)} \\
P^i_{abs}(E) &= \frac{\sigma^i_a(E)}{\sigma^i_t(E)} \\
P^i_f(E) &= \frac{\nu^i(E)\sigma^i_f(E)}{\sigma^i_t(E)}
\end{aligned}
\tag{2.6}
$$

P_{nabs} is the non-absorption collision probability and is merely the sum of all non-absorption reactions divided by the total cross section for the particular energy point i. P_{abs} is the absorption collision probability and is the absorption cross section divided by the total cross section. Finally, P_f is the fission collision probability, and is the fission cross section, multiplied by the average number of neutrons released per fission, divided by the total cross section.

2.3.2 Probability Tables

In recent years it has proven advantageous to create "probability tables" for use in the unresolved resonance region (URR) instead of using the cross sections directly. In the resolved resonance region (RRR), resonances are modeled explicitly, and, by using a large number of energy points, can be portrayed in the cross section data files quite accurately. However, resonances don't stop when the URR is reached, only our ability to explicitly model them. In order to combat this lack of cross section data, probability tables that can be sampled to get cross sections to use for the collision are used. This is illustrated in Figure 2.3 and explained below.

Probability tables work similarly to histograms, where each table works over a small energy range. Within each table there are cross sections associated with a probability. Usually the probability of each cross section is uniform (that is, there is an equal probability of each cross section being chosen), but this is not always the case. Figure 2.3 illustrates probability tables where each bin within a probability table has an equal chance of being chosen, but the probability tables at different

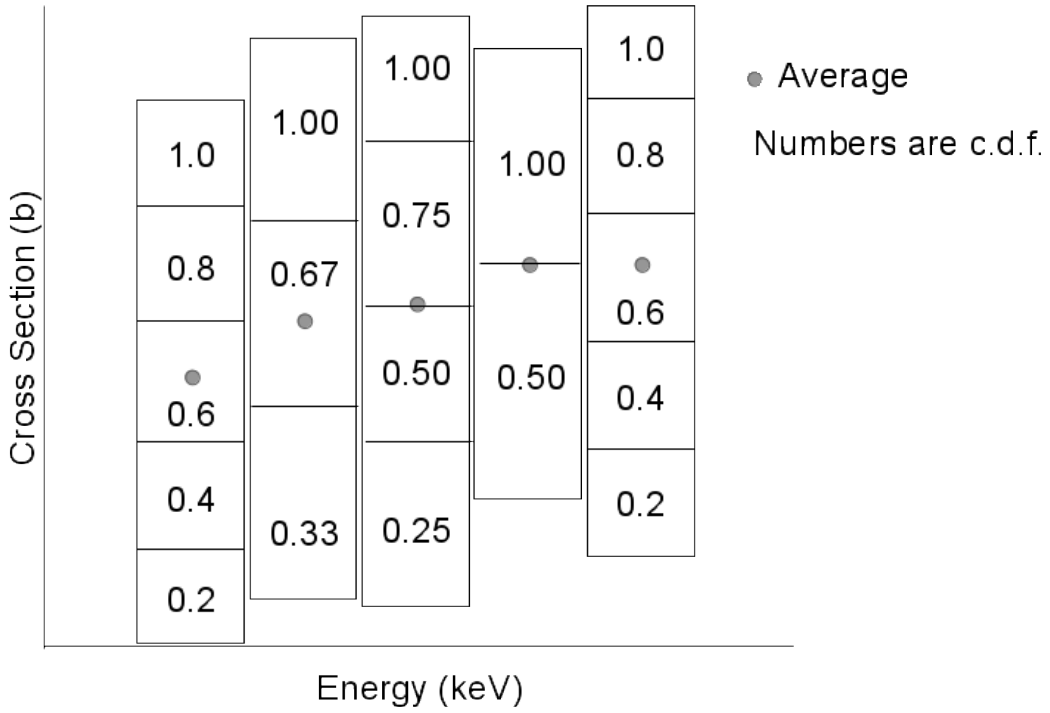

Figure 2.3: Probability Tables

energies have a different number of bins. The average cross section, indicated by the dot, is the 1D cross section for the reaction type and is also stored on the cross section library.

2.4 Resonance Processing

All multigroup libraries need to undergo problem dependent resonance processing. During the resonance processing, spatial and energy self-shielding of the cross sections is computed using a variety of methods. Two methods common in SCALE are the Bondarenko method (used by the BONAMI [10] code) and solving an approximation of the problem using point-wise cross sections (used by the CENTRM [11] code). BONAMI will be the focus of this discussion, but the approach used by CENTRM will be discussed for completeness.

2.4.1 Bondarenko Method

Similar to calculating the multigroup cross sections (see Equation 2.3), in multigroup resonance self-shielding calculations the effective cross sections are integrated over all energies as weighted by the flux. The cross sections are generally known as input data, therefore the resonance self-shielding involves a determination of the flux, $\phi(u)$ (flux per unit lethargy, u). For the Bondarenko method, the flux is based on a very simple expression for the flux in an infinite homoegeneous medium:

$$\phi(u) \approx \frac{1}{\Sigma_t(u)} \,. \tag{2.7}$$

Applying this to Equation 2.3, we get

$$\overline{\sigma_g^i} = \frac{\int_g \mathrm{d}u \dfrac{\sigma^i(u)}{\Sigma_t(u)}}{\int_g \mathrm{d}u \dfrac{1}{\Sigma_t(u)}} \,. \tag{2.8}$$

This can be changed to

$$\overline{\sigma_g^i} = \frac{\int_g \mathrm{d}u \dfrac{\sigma^i(u)}{N_i\sigma_t^i(u) + \sum_{j\neq i} N_j\sigma_j^i(u)}}{\int_g \mathrm{d}u \dfrac{1}{N_i\sigma_t^i(u) + \sum_{j\neq i} N_j\sigma_j^i(u)}} \,, \tag{2.9}$$

where i is the nuclide of interest, N is the nuclide number density, and σ_t is the microscopic total cross section.

By defining

$$\sigma_0^i = \sum_{j\neq i} N_j\sigma_t^j(u)/N_i \,, \tag{2.10}$$

we can obtain

$$\overline{\sigma_g^i} = \frac{\int_g \mathrm{d}u \dfrac{\sigma^i(u)}{\sigma_t^i(u) + \sigma_0^i(u)}}{\int_g \mathrm{d}u \dfrac{1}{\sigma_t^i(u) + \sigma_0^i(u)}} \,, \tag{2.11}$$

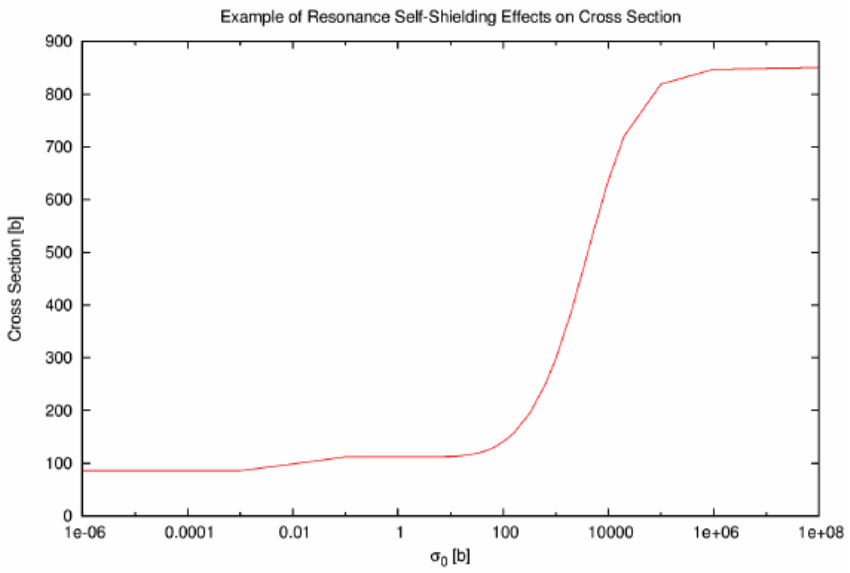

Figure 2.4: Resonance Self-Shielding Effects

where σ_0^i is the cross section per atom of the nuclide i for all nuclides in the mixture other than i itself. By using a constant value for σ_0 within each energy group, the Bondarenko method ignores the fine group structure. However, one can then pre-calculate cross sections without having to know the detailed composition in which they are used. For σ_0 being infinite (for infinitely dilute), Equation 2.11 reduces to

$$\bar{\sigma}_g \mathrm{ID} = \frac{\int_g \mathrm{d}u \sigma(u)}{\int_u \mathrm{d}u} \,. \tag{2.12}$$

Now, for any value of σ_0 and temperature, the self shielding cross sections can be simply calculated by

$$\bar{\sigma}_g(\sigma_0, T) \equiv F_g(\sigma_0, T) \bar{\sigma}_g \mathrm{ID} \,, \tag{2.13}$$

where F_g is known as the F-factor, or "Bondarenko factor." These factors are pre-calculated and placed in a lookup table on the cross-section library. The effect of a decreasing σ_0 is that of a more heavily shielded cross section. This is illustrated in Figure 2.4.

As mentioned, the above process can be used directly for the homogeneous case. However, for heterogeneous cases the effects of leakage must be considered. This is done by including an additional effective escape cross section in the σ_0 term. This is due to the second equivalence theorem of resonance escape which states that a heterogeneous lattice characterized by an escape cross section σ_e has the same resonance integral as a homogeneous mixture with a background cross section of $\sigma_0 + \sigma_e$. [10] An approximation of the escape cross section is

$$\sigma_e = \frac{1}{\bar{l} N_i}\,, \tag{2.14}$$

where l is the mean chord length in the body and N_i is the number density of the nuclide being calculated.

Most reactors have a regular geometry of repeating cells and the presence of these cells will affect the flux seen by an individual cell. This will result in additional self-shielding of the resonance cross sections. To account for this, l can be modified by using Dancoff factors. There are several different Dancoff expressions that can account for different geometries, but they are beyond the scope of this document.

2.4.2 Pointwise Solution Method

As computers have become more powerful, it has become more practical to solve an approximation of the problem using a very fine group structure. The fluxes obtained from this solution can then be used to calculate the multigroup, problem specific, cross sections. Modules within the SCALE computer code such as CENTRM will calculate the problem specific fluxes given an approximation of the geometry, while PMC [12] will do the multigroup processing to create the multigroup data.

Since this method requires a pointwise energy structure, it isn't feasible to run a complex geometry; it would take far too long. Generally CENTRM will treat a simplified 1D problem, which is usually acceptable for pin cells and infinite homogeneous media. By running CENTRM multiple times on the different materials

and geometries present, one can create self-shielded multigroup cross sections for all materials in a problem. Above the resolved energy range, CENTRM will use multigroup data. In particular, codes applying the Bondarenko method (like BONAMI) still need to be run because CENTRM will use corrections based on the shielded mutligroup cross sections for the URR.

2.5 Radiation Transport Theory

The most general representation of radiation transport theory starts with solving the neutral particle Boltzmann transport equation. This equation is, in its most basic form, a conservation of particles where particle inventory is kept using some form of the neutron density distribution throughout the core, $N(\vec{\mathbf{r}}, E, t)d^3rdE$. This neutron density represents the expected number of neutrons in d^3r about $\vec{\mathbf{r}}$, energies in dE about E, at time t [2]. Most computational calculations of the radiation transport equation ignore time (i.e. assume steady-state) and use what is called the angular flux, $\psi(\vec{\mathbf{r}}, E, \hat{\mathbf{\Omega}})$. Angular flux represents the neutron density at position, $\vec{\mathbf{r}}$, energy, E, and direction, $\hat{\mathbf{\Omega}}$, within the phase space $(d\vec{\mathbf{r}}, dE, d\hat{\mathbf{\Omega}})$. This time-independent, general form of the neutral particle Boltzmann transport equation is given by

$$\begin{aligned}\vec{\nabla}\cdot\hat{\mathbf{\Omega}}\psi(\vec{\mathbf{r}}, E, \hat{\mathbf{\Omega}}) + \Sigma_t(\vec{\mathbf{r}}, E)\psi(\vec{\mathbf{r}}, E, \hat{\mathbf{\Omega}}) = \\ \frac{\chi(E)}{4\pi}\int_0^\infty dE'\int_0^{4\pi}\hat{\mathbf{\Omega}}'\nu(E')\Sigma_f(\vec{\mathbf{r}}, E'\to E, \hat{\mathbf{\Omega}}'\to\hat{\mathbf{\Omega}})\psi(\vec{\mathbf{r}}, E', \hat{\mathbf{\Omega}}') \\ + \int_0^\infty dE'\int_0^{4\pi} d\hat{\mathbf{\Omega}}'\Sigma_s(\vec{\mathbf{r}}, E'\to E, \hat{\mathbf{\Omega}}'\to\hat{\mathbf{\Omega}})\psi(\vec{\mathbf{r}}, E', \hat{\mathbf{\Omega}}') \\ + Q(\vec{\mathbf{r}}, E, \hat{\mathbf{\Omega}})\,, \quad (2.15)\end{aligned}$$

where

ψ angular flux at $\vec{\mathbf{r}}$ per unit volume, in direction $\hat{\mathbf{\Omega}}$ per unit solid angle, and at energy E per unit energy

Σ_t total macroscopic cross section for interaction at $\vec{\mathbf{r}}$ and energy E

χ energy of fission neutrons emitted from fission reactions induced by neutrons with energy E

ν average number of fission neutrons emitted from fission reactions induced by neutrons with energy E'

Σ_s scattering cross section at $\vec{\mathbf{r}}$ from energy E' and direction $\hat{\mathbf{\Omega}}'$ to energy E and direction $\hat{\mathbf{\Omega}}$.

In Equation 2.15 the mechanisms for neutron loss are on the left-hand side of the equation and the mechanisms for neutron production are on the right-hand side of the equation [13]. The terms can be broken down into their respective components as shown. The streaming rate of loss from the phase space,

$$\vec{\nabla} \cdot \hat{\mathbf{\Omega}} \psi(\vec{\mathbf{r}}, E, \hat{\mathbf{\Omega}}) \,, \tag{2.16}$$

the rate of loss from nuclear interactions within the material(s),

$$\Sigma_t(\vec{\mathbf{r}}, E) \psi(\vec{\mathbf{r}}, E, \hat{\mathbf{\Omega}}) \,, \tag{2.17}$$

the rate of neutron production from fission reactions,

$$\frac{\chi(E)}{4\pi} \int_0^\infty dE' \int_0^{4\pi} \hat{\mathbf{\Omega}}' \nu(E') \Sigma_f(\vec{\mathbf{r}}, E' \to E, \hat{\mathbf{\Omega}}' \to \hat{\mathbf{\Omega}}) \psi(\vec{\mathbf{r}}, E', \hat{\mathbf{\Omega}}') \,, \tag{2.18}$$

the rate of neutrons emerging from scattering reactions,

$$\int_0^\infty dE' \int_0^{4\pi} d\hat{\mathbf{\Omega}}' \Sigma_s(\vec{\mathbf{r}}, E' \to E, \hat{\mathbf{\Omega}}' \to \hat{\mathbf{\Omega}}) \psi(\vec{\mathbf{r}}, E', \hat{\mathbf{\Omega}}') \,, \tag{2.19}$$

and an external source term (if present),

$$Q(\vec{\mathbf{r}}, E, \hat{\mathbf{\Omega}}) \,. \tag{2.20}$$

Key quantities that can be determined by solving the Boltzmann transport equation include neutron flux, energy deposition, isotopic inventory of various reactor materials, and reaction rates. Knowledge of the neutron distribution, in particular the reaction rate distribution, is of importance since it allows us to solve for energy deposition in a material, time-dependent rate of change of nuclide densities, and to calculate k_{eff}.

There are two main categories in which computer codes solving the transport equation can fall into: deterministic and stochastic. In general, deterministic methods utilize several approximations and discretizations of the independent variables (such as space, energy, and direction) and apply one or more numerical methods to solve the Boltzmann transport equation (Equation 2.15) for the average particle behavior. Some deterministic methods include Discrete Ordinates (S_N), the integral transport method, Method of Characteristics (MOC), and diffusion theory. Stochastic methods include the Monte Carlo method, which involves simulating particle transport by randomly sampling the many mathematical distributions or probability density functions that define neutron transport and neutron interactions with a material. Results are obtained by recording information from these individual"particle walks" to provide mean values for average particle behavior. The most general comparison between these two methodologies is that deterministic solutions provide exact solutions to approximate models whereas stochastic methods give approximate solutions to exact models.

2.6 Thermal Neutron Scattering

Outside of the thermal range, neutrons can always be assumed to only downscatter – that is, always lose energy in a collision. However, in the range of a few eV, the thermal motion of the nuclei can no longer be ignored and neutrons can easily gain energy in a collision. For certain moderating materials, such as hydrogen in water, one also has to acknowledge that a neutron will tend to interact with an aggregate of atoms rather than a single nucleus. These atoms can be in molecular or crystalline materials, and this further complicates the scattering process. [5] Various types of scattering in the thermal range are described below.

2.6.1 Double Differential Scattering Cross Section

Coherent Elastic Scattering

For coherent elastic scattering, the double differential scattering cross section from a powdered crystalline material may be represented as

$$\frac{d^2\sigma}{dE'd\Omega}(E \to E', \mu, T) = \frac{1}{E}\sum_{i=1}^{E_i<E} s_i(T)\delta(\mu - \mu_i)\delta(E - E')/2\pi\,, \tag{2.21}$$

where

$$\mu_i = 1 - \frac{2E_i}{E}\,. \tag{2.22}$$

In Equation 2.21, and the following scattering formulas, the following definitions are used:

E incident neutron energy (eV),

E' secondary neutron energy (eV),

μ cosine of the scattering angle,

T moderator temperature (K),

E_i energies of the Bragg edges (eV),

s_i proportional to the structure factors (eV·barns),

μ_i characteristic scattering cosines for each set of lattice planes.

The Bragg edges and structure factors can be calculated from the properties of the crystal lattice and the scattering amplitudes for the various atoms in the unit cell [5].

Incoherent Elastic Scattering

Elastic scattering can be treated with the incoherent approximation for partially ordered systems such as ZrH_x and polyethylene. The differential cross section in this case is given by:

$$\frac{d^2\sigma}{dE'd\Omega}(E \to E', \mu, T) = \frac{\sigma_b}{4\pi} e^{-2EW'(T)(1-\mu)} \delta(E - E') \,, \tag{2.23}$$

where

σ_b is the characteristic bound cross section (barns),

E' is the DebyeWaller integral divided by the atomic mass (eV^{-1}),

and all the other symbols have their previous meanings. The integrated cross section can be easily obtained as

$$\sigma(E) = \frac{\sigma_b}{2} \left(\frac{1 - e^{-4EW'}}{2EW'} \right) \,. \tag{2.24}$$

Incoherent Inelastic Scattering

Inelastic scattering is generally represented by the thermal scattering law and is defined for a moderating molecule or crystal by

$$\frac{d^2\sigma}{dE'd\Omega}(E \to E', \mu, T) = \frac{\sigma_b}{4\pi kT} \left(\frac{E}{E'} \right)^{1/2} \exp\left(-\frac{\beta}{2} \right) S(\alpha, \beta, T) \,, \tag{2.25}$$

where σ_b is the scattering cross section for a neutron incident on a bound nucleus, and $S(\alpha, \beta)$ is a scattering function that depends on the detailed dynamics and structure

of the scattering material, where α and β in the scattering function are defined as

$$\alpha \equiv \frac{E' + E - 2\mu_0\sqrt{E'E}}{AkT}, \beta \equiv \frac{E - E'}{kT}$$

The simplest model of neutron thermalization is for neutrons scattering from a monatomic gas of unbound nuclei distributed in energy, according to a Maxwellian distribution, for which the scattering function is

$$S(\alpha, \beta) = \frac{1}{2(\pi\alpha)^{1/2}} \exp\left(-\frac{\alpha^2 + \beta^2}{4\alpha}\right) . \tag{2.26}$$

This yields (using Equation 2.25)

$$\Sigma_S(E' \to E, \mu_0) = \left(1 + \frac{1}{A}\right)^2 \frac{\Sigma_f}{4\pi} \left(\frac{E}{E'}\right)^{1/2} \left(\frac{A}{2\pi kT\hbar^2\kappa^2}\right)^{1/2} \times \exp\left[-\frac{A}{2kT\hbar^2\kappa^2}\left(\epsilon - \frac{\hbar^2\kappa^2}{2A}\right)^2\right] , \tag{2.27}$$

where A is the atomic mass (amu) of the target nuclei, σ_f is the total scattering cross section for a neutron incident on a free nucleus, and

$$\epsilon \equiv E' - E$$
$$\hbar^2\kappa^2 = 2m(E' + E - 2\mu_0\sqrt{E'E}) .$$

The quantum mechanical theory for neutron scattering from a system of bound nuclei leads to an expression for the double differential scattering function for

scattering from energy E' to energy E and from direction $\mathbf{\Omega}'$ to direction $\mathbf{\Omega}$:

$$\Sigma_s(E' \to E, \mathbf{\Omega}' \to \mathbf{\Omega}) = \frac{\Sigma_{\text{coh}}}{4\pi\hbar}\sqrt{\frac{E}{E'}}\frac{1}{2\pi}\int_{-\infty}^{\infty}\int e^{i(\kappa\cdot\boldsymbol{r}-\epsilon t/\hbar)}G(\boldsymbol{r},t)\,\mathrm{d}\boldsymbol{r}\,\mathrm{d}t + \frac{\Sigma_{\text{inc}}}{4\pi\hbar}\sqrt{\frac{E}{E'}}\frac{1}{2\pi}\int_{-\infty}^{\infty}\int e^{i(\kappa\cdot\boldsymbol{r}-\epsilon t/\hbar)}G_s(\boldsymbol{r},t)\,\mathrm{d}\boldsymbol{r}\,\mathrm{d}t\,, \tag{2.28}$$

where

$\hbar$	is the reduced Planck's constant,
$\hbar\kappa = m(\boldsymbol{\nu}' - \boldsymbol{\nu})$	is the neutron momentum exchange vector,
$\epsilon = E' - E$	is the neutron energy change, and
Σ_{coh} and Σ_{inc}	are the bound coherent and incoherent macroscopic cross sections.

For many bound thermal moderators, it has proven beneficial to use calculated $S(\alpha,\beta)$ tables. These tables can be used to calculate the double differential scattering cross sections by using Equation (2.25). For a certain moderator, such as hydrogen in heavy water, these lookup tables will be in addition to the normal cross section data used to calculate the scattering effects.

2.6.2 Calculation of the Thermal Neutron Spectra

$S(\alpha,\beta)$ tables are generally only calculated and used for thermal moderators, so there are still many other nuclides that require thermal treatment; this is usually accomplished by using the free gas approximation. In this approximation the reactor core can be modeled as a free or proton gas that is in thermal equilibrium at some temperature. Most schemes for calculating the thermal neutron spectra directly solve the infinite medium spectrum equation for the thermal energy range

$$\Sigma_t(E)\phi(E) = \int_0^{E_c}\mathrm{d}E'\,\Sigma_S(E' \to E)\phi(E') + S(E), \quad 0 < E < E_c\,, \tag{2.29}$$

where S is the slowing down source and E_c is high enough that no upscatter occurs outside of this range.

In 1944, E. Wigner and J. Wilkins [14] published a simplification of the above equation. By assuming a proton free gas at thermal equilibrium, they could integrate over all final neutron energies quite easily. They then noticed that the structure of this scattering kernel is quite similar to that of Green's functions of second-order differential equations. Therefore, Equation 2.29 can be written in the form

$$\alpha(x)\phi(x) = \int_a^b \mathrm{d}x'\, G(x,x')\phi(x')\,, \tag{2.30}$$

Wigner and Wilkins then used their knowledge of Green's functions to convert Equation 2.29 into a differential equation for $\Phi = \phi(E)/[EM(E)]^{1/2}$

$$-\frac{\mathrm{d}}{\mathrm{d}x}\left\{\frac{1}{P(x)}\frac{\mathrm{d}}{\mathrm{d}x}[V(x)+\Gamma]\Phi(x)\right\} + \left\{W(x)[V(x)+\Gamma] - \frac{r}{\sqrt{\pi}}\right\}\Phi(x) = 0\,, \tag{2.31}$$

where

$$\begin{aligned} W(x) &= \frac{x^2}{P(x)} - \frac{e^{-x^2}}{P^2(x)}, \quad x \equiv \left(\frac{e}{kT}\right)^{1/2}, \\ P(x) &= e^{-x^2} + \sqrt{\pi}\, x\, \mathrm{erf}(x)\,, \\ \Gamma &= \frac{\Sigma_a(kT)}{\Sigma_{\mathrm{fr}}^H} = \frac{N_a\gamma}{\nu_T N_H \sigma_s^H}\,. \end{aligned}$$

The equation can be further modified into a nonlinear first-order differential equation (akin to a Ricatti equation) which is suitable for numerical integration.

2.7 Monte Carlo

Since this dissertation focuses mostly on Monte Carlo methods, a brief description of Monte Carlo will be given here. At a fundamental level, neutron transport through matter is formulated as an essentially stochastic process. The total cross section is

a probability that a neutron will have a collision while traversing through a certain spatial interval. If a collision does occur, then the other cross sections (scattering, radiative capture, fission, etc.) are probabilities that a specific type of event will occur. In essence, the Monte Carlo method directly simulates neutron transport as a stochastic process. This section is not meant to be an exhaustive overview of the Monte Carlo method; interested readers should consult a Monte Carlo text such as [3] for more information.

2.7.1 Probability Functions

An important type of function in Monte Carlo codes are probability distribution functions (PDFs). PDFs give the probability of what x will be, given an interval $a \leq x \leq b$. In other words, there exists a PDF, $f(x)$, such that $f(x)\,\mathrm{d}x$ is the probability that a variable takes on a value within dx about x. The normalization is usually chosen such that

$$\int_a^b f(x)\,\mathrm{d}x = 1\,. \tag{2.32}$$

In general, $f(x) \geq 0$ wil not be a monotonically increasing function of x, which means that a given value for f does not correspond to a unique value of x.

More useful is the cumulative probability distribution function (CDF), $F(x)$. It is the probability that the variable x takes on a value less than or equal to x,

$$F(x) = \int_a^x f(x')\mathrm{d}x'\,. \tag{2.33}$$

Therefore we can get the probability of a neutron having a value of x between x and $x + \mathrm{d}x$ as

$$F(x + dx) - F(x) = f(x)\mathrm{d}x\,. \tag{2.34}$$

If κ is a random number distributed between 0 and 1, the values of x determined from $F(x) = \kappa$ will be distributed as $f(x)$. As can be seen, since cross sections can

be taken as a form of probability, it should be easy to convert them into a table of CDFs for sampling.

As an example of sampling from a distribution, we will look at generating a series of random numbers that are distributed according to the number of mean free paths between collisions. The mean free path is the mean distance that a particle will travel before a collision. We know from the number of mean free paths, x, that a particle can travel before a collision is $0 < x < \infty$. The PDF can be given as

$$f(x) = e^{-x}\,, \tag{2.35}$$

and the CDF as

$$F(x) = 1 - e^{-x}\,. \tag{2.36}$$

Physically, $f(x)\mathrm{d}x$ is the probability that a particle starting at $x = 0$ will have a collision between x and $x + dx$, while $F(x)$ is the probability that it will have a collision within the distance x. For this simple relationship, we can invert to directly obtain

$$x = -\ln(1 - \xi) = -\ln\xi\,, \tag{2.37}$$

where ξ is a random number.

2.7.2 Analog Simulation of Neutron Transport

We can trace the path of an individual neutron as it traverses matter and consider the various effects that might affect its history. By doing this, we can understand how a Monte Carlo calculation simulates the stochastic nature of neutron transport. To begin with, we must first determine the source of neutrons in a nuclear reactor, which is predominantly (if not entirely) the fission source. The fission source has distributions in space, in energy given by the fission spectrum, and in direction that is isotropic. Each of these distributions can be characterized by a PDF and a CDF.

By generating a random number and selecting from the various CDFs, we can define all of the characteristics of the source particle (space, energy, and direction).

Once "launched", the source neutron will travel in a straight line until it has a collision. The probability that a neutron has a collision at a distance x along the flight path is

$$T(x) = \Sigma_t(x) \exp\left[-\int_0^x \Sigma_t(x')\mathrm{d}x'\right], \tag{2.38}$$

which is the PDF for the collision distance x. Generating a random number ξ and selecting x from the CDF

$$-\ln \xi = \int_0^x \Sigma_t(x')\mathrm{d}x' \tag{2.39}$$

locates the position of the first collision. However, this is complicated by the fact that the neutron may transverse a nonuniform geometry. It becomes necessary to know the composition at the point of first collision. We can treat the medium as piecewise homogeneous and define the lengths of each uniform segment of the straightline flight path as x_j. If

$$\sum_{j=1}^{n-1} \Sigma_{tj} x_j \leq -\ln \xi < \sum_{j=1}^{n} \Sigma_{tj} x_j \,, \tag{2.40}$$

the collision occurs in the nth region at a distance

$$x'_n = \frac{1}{\Sigma_{tn}} \left(-\ln \xi - \sum_{j=1}^{n} \Sigma_{tj} x_j\right) \tag{2.41}$$

beyond the entrance of the flight path into region n. Perhaps unexpectedly, the majority of the time spent in Monte Carlo tracking is in the geometry portion. Determining where the neutron is in a geometry, and where the next collision is going to occur, is an important part of any Monte Carlo code and has likely been optimized as such.

Now that the location of the collision has been determined, it is necessary to determine what type of nuclide and what type of reaction are involved. The

probability for a reaction of type x with a nuclide of species i is

$$p_{ix} = \frac{N_i \sigma_{ix}}{\sum_{i,x} N_i \sigma_{ix}}\,, \tag{2.42}$$

where N_i is the number density of nuclide i in region n, and σ_{ix} is the microscopic cross section for reaction x for nuclide i at the energy of the neutron. Constructing a PDF and CDF, generating a random number ξ, and selecting the nuclide and reaction type by equating ξ and the CDF, allows the nuclide and reaction type to be determined.

If the reaction type is determined to be absorption, the neutron history is terminated, the energy and location of the absorbed neutron are recorded, and another neutron history is started. If the reaction is elastic scattering, another random number needs to be generated and it is equated to the CDF for the cosine of the scattering angle in the center of mass (CM) frame to obtain μ_{CM}. It can then be transformed to obtain the scattering angle in the lab frame. For energies above thermal, the energy of the scattered neutron can be determined from μ_{CM} by scattering kinematics,

$$E' = \frac{E(A^2 + 2A\mu_{\mathrm{CM}} + 1)}{(A+1)^2}\,. \tag{2.43}$$

Knowing E', the cosine of the scattering angle in the lab frame can be determined from

$$\mu = \cos\theta = \frac{1}{2}(A+1)\sqrt{\frac{E}{E'}} + \frac{1}{2}(A-1)\sqrt{\frac{E'}{E}}\,. \tag{2.44}$$

With thermal scattering from bound lattices, the cross sections are more involved (see Section 2.6.1) and both cross section and energy CDFs must be sampled.

2.7.3 Statistical Estimation and Variance Reduction

The mean value of a function, $h(x)$, of x is defined in terms of the PDF for x by

$$\langle h \rangle = \int_a^b \mathrm{d}x\, h(x) f(x)\,, \tag{2.45}$$

and the standard deviation, σ, and the variance, V, are defined as:

$$\begin{aligned}\sigma(h) = \sqrt{V(h)} &= \left\{ \int_a^b \mathrm{d}x [h(x) - \langle h \rangle]^2 f(x) \right\}^{1/2} \\ &= [\langle h^2 \rangle - \langle h \rangle^2]^{1/2} \,.\end{aligned} \tag{2.46}$$

If N random values of the variable x are chosen from the CDF, then a statistical estimate of the mean value $\langle h \rangle$ is

$$\bar{h} = \frac{1}{N} \sum_{n=1}^{N} h(x_n) \,. \tag{2.47}$$

A bound for the error in an estimate of this type is given by the central limit theorem, which states that if many estimates $\bar{h}$ of $\langle h \rangle$ are obtained, each estimate involving N trials, the variable $\bar{h}$ is normally distributed about $\langle h \rangle$ to terms of accuracy $O(1/N^{1/2})$. In the limit $N \to \infty$, this theorem takes the form

$$\mathrm{Prob} \left\{ \langle h \rangle - \frac{M\sigma(h)}{\sqrt{N}} \leq \bar{h} \leq \langle h \rangle + \frac{M\sigma(h)}{\sqrt{N}} \right\} = \begin{cases} 0.6826, & M = 1 \\ 0.954, & M = 2 \,. \\ 0.997, & M = 3 \end{cases} \tag{2.48}$$

Equation 2.48 shows the probability that the statistical estimate of the mean value of Equation 2.47 is within $\pm M\sigma/N^{1/2}$ (or "M sigmas") of the exact value $\langle h \rangle$ is 68.3% for $M = 1$ (one σ), 95.4% for $M = 2$ (two σs), 99.7% for $M = 3$, etc.

As can be seen from Equation 2.48, the number of histories run, N, needs to be quadruped to halve the statistical uncertainty. However, there are ways to improve the efficiency of the run by using various variance reduction techniques. The discussion of this topic is outside of the scope of this dissertation, but usually involves modifying the neutron history somehow to achieve a modified distribution function that yields the same mean value with a smaller variance. Interested readers should consult [3] for information on a widespread number of variance reduction techniques.

2.7.4 Tallies

One of the main goals of a Monte Carlo calculation is the calculation of reaction rates in various regions, over various energies, and by various nuclides. This can be accomplished by tallying each collision event. Neutron fluxes and currents can also be calculated by tallying events and surface crossings. The collision rate is calculated by the product of the cross section times the flux times the volume. Therefore, by tallying the rate of collisions, we can calculate the flux from

$$\phi = \frac{\mathrm{CR}}{\Sigma_t V}\,, \tag{2.49}$$

where CR is the collision rate, and V is the volume of the region of interest. One shortcoming with this approach is that only particles which collide within the volume will contribute to the flux. Another method of calculating the scalar flux is to use the path length traversed by all particles passing through a volume per unit volume per unit time

$$\bar{\phi} = \frac{\bar{l}}{V} = \frac{1}{V}\frac{1}{N}\sum_{n=1}^{N} l_n\,, \tag{2.50}$$

where $\bar{l}$ is the track length per unit time in the volume in question of the nth history. If neutron weights are to be taken into account, Equation 2.50 must be modified to

$$\bar{\phi} = \frac{1}{V}\frac{1}{N}\sum_{m} w_n l_n\,, \tag{2.51}$$

where w_n is the weight of the neutron on the nth history.

The variance in the flux estimate is given by

$$V_{ar} = \frac{N}{N-1}\left[\frac{1}{V^2 N}\sum_{n=1}^{n}(w_n l_n)^2 - \frac{1}{V^2 N^2}\left(\sum_{n=1}^{N} w_n l_n\right)^2\right]\,. \tag{2.52}$$

Care must be taken when tallying on very small regions or with a small number of histories. In these cases the variance on the tally can be quite large, sometimes even

as large as the tally itself. Variance reduction techniques or running many histories are required for these tallies.

2.7.5 Criticality Problems

One application Monte Carlo neutron transport codes is to calculate the multiplication factor and associated eigensolution for the flux distribution. Generally, the problem is started with an arbitrary or random spatial distribution of neutrons distributed in the fission energy spectrum and isotropically in all directions. If possible, it is sometimes beneficial to start the neutrons based on some previous knowledge obtained from experience or a short run of a deterministic code. Each generation of neutrons can serve as the source of neutrons for the next generation. Generations of neutrons are run until the fission source has converged. At this point, tallies can begin and the ratio of the total number of fission neutrons on successive generations can be used as the statistical estimate of the multiplication constant.

2.8 KENO

KENO is a three-dimensional Monte Carlo criticality neutron transport program developed and maintained by ORNL as part of the SCALE code package [1]. It has a flexible geometry package that is capable of modeling any volume that can be constructed using quadratic equations. The primary purpose of KENO is to determine k-effective, but it also calculates lifetime, generation time, energy-dependent leakages, energy- and region-dependent absorption, fissions, flux densities, and fission densities.

This section presents a brief overview of the theory of KENO and builds upon Section 2.7. Particular emphasis is placed on how KENO handles neutron scattering in the thermal and epithermal range, as this is the area that is modified using the techniques discussed in this dissertation.

2.8.1 Transport Equation

KENO [9] solves a form of the Boltzmann transport equation (Equation 2.15) which has been simplified by consolidating the fission sources, assuming the media to be stationary, and ignoring time-dependence

$$\Omega \cdot \nabla\Phi + \Sigma_t(X, E, \Omega)\Phi(X, E, \Omega) = q(X, E, \Omega)\,, \tag{2.53}$$

where

- Φ is the neutron flux (neutrons/cm^2/s),
- Σ_t macroscopic total cross section of the media (cm^{-1}),
- q neutrons/cm^3/s source.

Utilizing the relationship $X' = X - R\Omega$, using an integrating factor, assuming no external source, and defining

$$T(R) = \int_0^R \Sigma_t(X - R'\Omega, E)\mathrm{d}R'\,, \tag{2.54}$$

the problem becomes an eigenvalue problem where the source is defined as

$$q(X, E, \Omega) = \iint \mathrm{d}E'\mathrm{d}\Omega'\Phi(X, E', \Omega')\Sigma_s(X, E' \to E, \Omega' \cdot \Omega) + \frac{1}{k}Q'(X, E, \Omega)\,, \tag{2.55}$$

where

- k is the largest eigenvalue of the integral equation,
- Q' is the fission source,
- Σ_s is the macroscopic scattering cross section.

By assuming the fission source to be isotropic, the final transport equation solved by KENO is

$$\Phi(X,E,\Omega) = \int_0^\infty \mathrm{d}R e^{-T(R)} \left\{ \frac{1}{k} \int_{E'} \int_{\Omega'} \nu(X - R\Omega, E') \Sigma_f(X - R\Omega, E') \right.$$
$$\chi(X - R\Omega, E' \to E) \Phi(X - R\Omega, E', \Omega') \mathrm{d}E' \frac{\mathrm{d}\Omega'}{4\pi}$$
$$\left. + \int_{E'} \int \Omega' \Sigma_t(X - R\Omega, E', \Omega') \Sigma_s(X - R\Omega, E' \to E, \Omega' \cdot \Omega) \right\}, \quad (2.56)$$

where

- χ is the fraction of neutrons born from fission,
- ν is the number of neutrons resulting from a fission,
- Σ_f is the macroscopic fission cross section of the material.

2.8.2 Collision Site Selection and Treatment

Collision site selection in KENO is the same as described in Section 2.7.2. A collision site is selected using a random number and the CDF describing where a nuclide will have an interaction between 0 and x along the path. Again, the equation becomes more complicated when there are multiple nuclides and multiple geometry regions in the problem.

The type of collision is again sampled similar to that described in Section 2.7.2. However, after selecting the collision target, the neutron's weight is reduced by the nonabsorption collision probability (see Section 2.3.1). Also, calculating the cross sections is not as straightforward a process as simply adding them up; if the collision energy is in the URR energy range, then the probability tables (see Section 2.3.2) need to be sampled. After the probability tables have been sampled, the resultant cross sections for the total and partial reactions are stored for retrieval.

For CE KENO, an explicit collision treatment is dictated by the point cross-section data. Due to this, the type of reaction must be modeled explicitly. Figure 2.5 provides

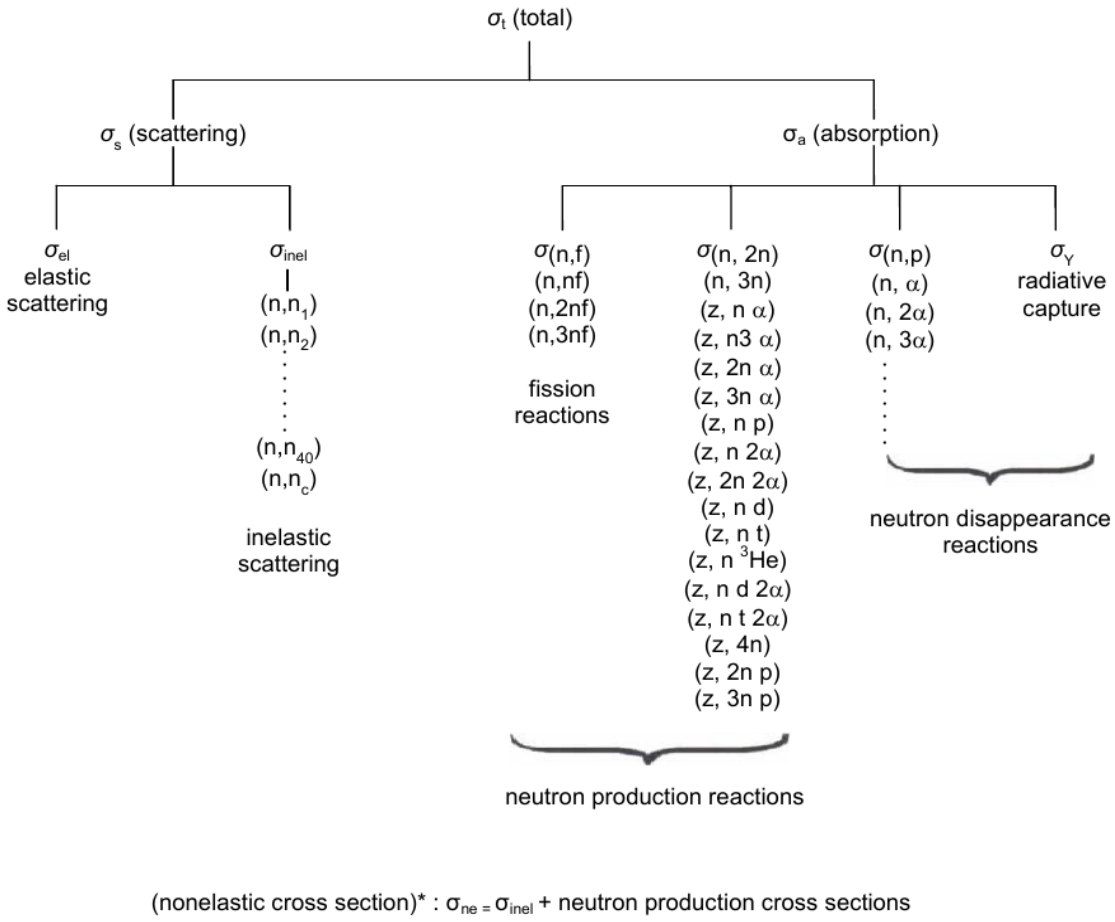

Figure 2.5: Cross-section hierarchy for particle interactions in KENO. [1]

a summary of the cross-section hierarchy in KENO. After selecting the reaction type, the angle and exit energy of the resultant neutron is determined (see Section 2.8.3). Finally, the new direction cosines in the lab system are calculated and tracking the history of the particle continues.

KENO uses an implicit approach to treat a fission event. KENO calculates a fission weight, and if the fission weight is greater than zero, the collision occured in a fissile material. The fission point is stored in the fission bank, and a pseudo-fission weight is stored with it. The energy and angular cosine must be selected from the kinematics

distribution. The fission weight is decreased by a production factor, and if the fission weight is still greater than zero the process repeats.

2.8.3 KENO Scattering Selection

The scattering (angle and energy) distributions in KENO deserve special mention because it is these cross sections that we are going to Doppler broaden in Chapter 6. Kinematics data are provided in the cross-section library in the lab (or target-at-rest) system. This allows KENO to not require transformation between different coordinate systems during the random walk. The kinematics data format is designed to accommodate coupled angle-energy distributions of secondary particles. Angle is sampled first, then energy.

Exit Angle Cosine

The kinematics format permits the anisotropic angular distributions to be expressed in either equiprobable or nonequiprobable cosine bins. Also, the formats permit the number of cosine bins to vary as a function of incident energy. In essence, each cosine distribution record can have NPU secondary angles that correspond to $NPU - 1$ cosine bins. The incident energy, E, will usually be between two bins (E_i and E_{i+1}). Therefore the angle cosine will have to be sampled in both tables and interpolated to a final result.

For equiprobable bins, the a^{th} bin is selected from the i^{th} table as

$$a = (NPU_i - 1) \times R_1 + 1 = NA_i \times R_1 + 1\,, \tag{2.57}$$

where a denotes an integer quantity, NA_i is the number of cosine bins for the i^{th} table, and R_1 is a random number. Similarly, the b^{th} bin is selected from the $i + 1^{\text{th}}$ table as

$$b = NA_{i+1} \times R_1 + 1\,. \tag{2.58}$$

Once the bins are determined, the cosine of the exiting angle from the bins can be selected by

$$\dot{\mu}_i = \mu_{i,a} + (a - NA_i \times R_1)(\mu_{i,a+1} - \mu_{i,a}) \tag{2.59}$$

$$\dot{\mu}_{i+1} = \mu_{i+1,b} + (b - NA_{i+1} \times R_1)(\mu_{i+1,b+1} - \mu_{i+1,b})\,. \tag{2.60}$$

The final exit angle cosine can then be determined through interpolation on the incident energy grid.

For nonequiprobable bins, the a^{th} bin is selected from the CDF for the i^{th} table as

$$C_{i,a-1} < R_1 < C_{i,a}\,, \tag{2.61}$$

the exit cosine can then be determined from the PDF using

$$\dot{\mu}_i = \mu_{i,a} + \frac{\sqrt{P_{i,a}^2 + 2s_i(R_1 - C_{i,a-1)}} - P_{i,a}}{s_1}\,, \tag{2.62}$$

where

$$s_i = \frac{P_{i,a+1} - P_{i,a}}{\mu_{i,a+1} - \mu_{i,a}}\,.$$

Again, the b^{th} bin is selected in a similar way, and interpolation on the incoming energies is performed to determine the final cosine.

Exit Energy

The procedure for sampling the exit energy is similar to that of sampling the exit cosine angle (with E used instead of μ); so not much detail will be described here. For equiprobable bins, the main difference is that once the exit energies from the two bins have been determined the final exit energy is determined by

$$E' = E'_i + \left(\frac{E - E_i}{E_{i+1} - E_i}(E'_{i+1} - E'_i)\right)\,, \tag{2.63}$$

where E'_i and E'_{i+1} are determined from interpolation on the exit cosine grid. The energies used are shown in Figure 2.6.

For nonequiprobable bins, a process similar to that used for the exit cosine angle is used. The main difference is calculating the exit energy using a formula similar to that given in Equation 2.62 but using exit energies instead of cosines.

2.8.4 Thermal Scattering Effects in KENO

As mentioned in Section 2.6, at thermal energies a collision between a neutron and nucleus can be affected by the thermal motion of the target nucleus. Evaluated Nuclear Data Format (ENDF) files provide thermal scattering law data to account for the thermal effects of scattering below 5 eV for a small variety of materials shown in Table 2.1. If this thermal scattering law data is not available for a material, the free gas approximation is used.

The double differential cross sections are calculated in AMPX and converted into CDFs and PDFs during library creation. As such, the fact that these $S(\alpha, \beta)$ tables exist is transparent to KENO; it just samples the kinematics data as described in Section 2.8.2.

Table 2.1: ENDF thermal scattering law data

Symbol	MAT	Principal Scatterer $S(\alpha, \beta)$	Coherent Elastic	Incoherent Elastic	Incoherent Inelastic $S(\alpha, \beta)$
be	26	Be	✓		✓
bemetal	26	Be	✓		✓
benzine (C_6H_6)	40	H			✓
beo	27	BeO	✓		✓
d_d2o	11	$^{2}_{1}$H			✓
graphite	31	C	✓		✓
h_ch2	37	H		✓	✓
h_h2o	1	H			✓
h_zrh	7	ZrH		✓	✓
lch4	33	H			✓
orthod	13	$^{2}_{1}$H			✓
orhoh	3	H			✓
parad	12	$^{2}_{1}$H			✓
parah	2	H			✓
sch4	34	H		✓	✓
zr_zrh	58	ZrH		✓	✓
o-beo	28	BeO	✓		✓
o-uo2	75	O	✓		✓
u-uo2	76	U	✓		✓

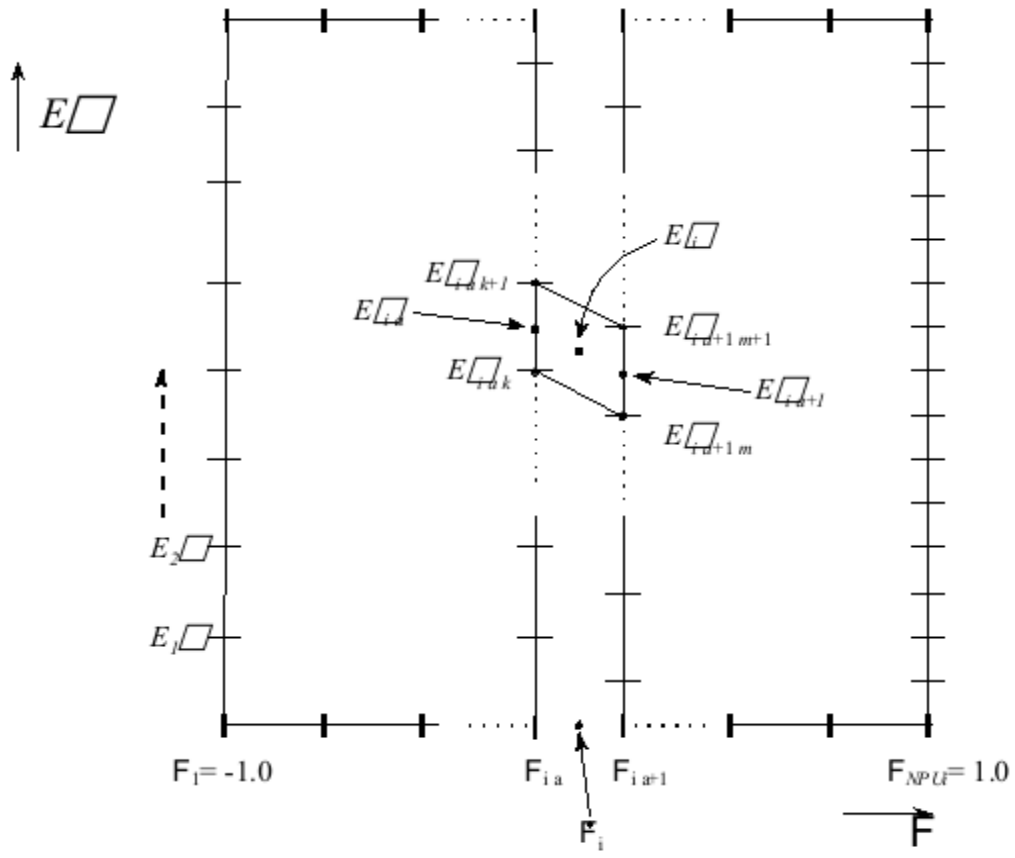

Secondary Angle-Energy Table i for E_i

Figure 2.6: Interpolation diagram for secondary angle-energy data.

Chapter 3

Literature Review and Previous Research

This section contains a review of pertinent literature. Topics include:

1. Development of a new double differential free gas scattering kernel,
2. development of the DBRC method,
3. development of methods for using the CE DBRC method to improve MG results,
4. Doppler broadening of one-dimensional cross sections, and
5. current research in methods to handle Doppler broadening of nuclear kinematics data.

3.1 Development of a New Scattering Kernel

In a series of related papers, Rothenstein and Dagan [15–18] derive and prove an ideal gas based kernel for scatterers with internal structure. As mentioned earlier in Section 2.6, the free gas scattering law is well established and used for scatterers without internal structure. However, it can be shown that for isotopes with strong

scattering resonances, there are some difficulties in using that approach. The model developed by Rothenstein and Dagan in [17] is actually the equivalent $S(\alpha, \beta)$ solution for heavy scatterers with strong energy dependent cross sections. Using their approach, a new double differential free gas kernel has been developed.

It was shown that for light water reactors, using this modified scattering kernel resulted in considerable impacts upon the criticality calculations, Doppler cofficients, and fuel inventory at the end of the fuel cycle [19]. Becker in [20] states that the underlying reason for the difference between the improved kernel and the traditional kernel is that whilst the integral scattering cross-section data is Doppler broadened, its differential part, namely the probability of a neutron to be scattered after an interaction with a target nuclei from an energy E to E' and from a specific spatial direction Ω to another direction Ω', is not. In addition, the solution of all deterministic and, in particular, stochastic codes ignore the existence of resonances and several computer codes arbitrarily set the temperature of the interacting heavy nuclide to zero outside of the thermal region.

Arbanas [21] built on the work done by Rothenstein and Ouisloumen [22] to compute temperature-dependent Legendre moments of the double differential elastic cross section. Ouisloumen had, independently of Rothenstein and Dagan, derived a general expression for Legendre moments of any order for an energy-dependent and anisotropic scattering cross section. Unfortunately, it was impractical to calculate anything other than the zeroth Legendre moment due to a threefold nested integral. Arbanas's work removed this limitation.

A double differential elastic scattering cross section in the laboratory frame at temperature T can be expanded in Legendre polynomials P_n as

$$\sigma_s^T(E \to E', \mu_{\text{lab}}) = \sum_{n \geq 0} \frac{2n+1}{2} \sigma_n^T(E \to E') P_n(\mu_{\text{lab}}) \,, \tag{3.1}$$

where $\mu_{\text{lab}} \equiv \cos(\overrightarrow{v}, \overrightarrow{v'})$, $\overrightarrow{v}$ and $\overrightarrow{v'}$ are the initial and the final velocity corresponding to the initial and the final energy E and E' in the laboratory frame, respectively, and

$P_n(\mu_{\text{lab}})$ are the Legendre polynomials. In order to solve this, the general expression for Legendre moments of a double differential elastic scattering cross section derived in [22] for a Maxwellian velocity distribution is required. This can be given as

$$\sigma_n^T(E \to E') = \frac{\beta^{5/2}}{4E} e^{E/kT} \int_0^\infty t\sigma_s^{\text{tab}}(E_{\text{CM}}) e^{-2t^2/A} \psi_n(t)\, \mathrm{d}t\,, \tag{3.2}$$

where E and E' are the incident and outgoing energies in the laboratory frame. The integration variable t is related to the energy in the center of mass frame by $E_{\text{CM}} = kTt^2/A$, where T is the temperature in units of Kelvin, k is the Boltzmann constant, A is the target mass in units of neutron mass, and $\beta = (A+1)/A$. $\sigma_s^{\text{tab}}(E_{\text{CM}})$ is a tabulated elastic scattering cross section at zero degrees Kelvin. In Equation 3.2, $\psi_n(t)$ is

$$\begin{aligned}\psi_n(t) = H(t_+ - t)H(t - t_-)G_n(t; \epsilon_{\max} - t, t + \epsilon_{\min}) + \\ H(t - t_+)G_n(t; \epsilon_{\min} - t, t + \epsilon_{\max})\,.\end{aligned} \tag{3.3}$$

Here H is the Heaviside step function and G_n is an auxiliary function, see [21].

Arbanas was able to solve for the Legendre moments of the scattering kernel for ^{238}U at a variety of energies. The results of his work for a scatter at 6.5 eV (just below the 6.67 eV absorption resonance in ^{238}U) are shown in Figure 3.1. As can be seen from the figure, the chance of upscatter from a neutron scattering off ^{238}U at 6.5 eV is actually higher than that of a downscatter. This will increase resonance absorption and lower the eigenvalue (see Section 3.2).

3.2 Development of the DBRC Method

The new scattering kernels cannot be used directly in a stochastic code like MCNP or KENO. A new sampling approach had to be developed and implemented in the sampling routines of the Monte Carlo codes. This new approach is documented in

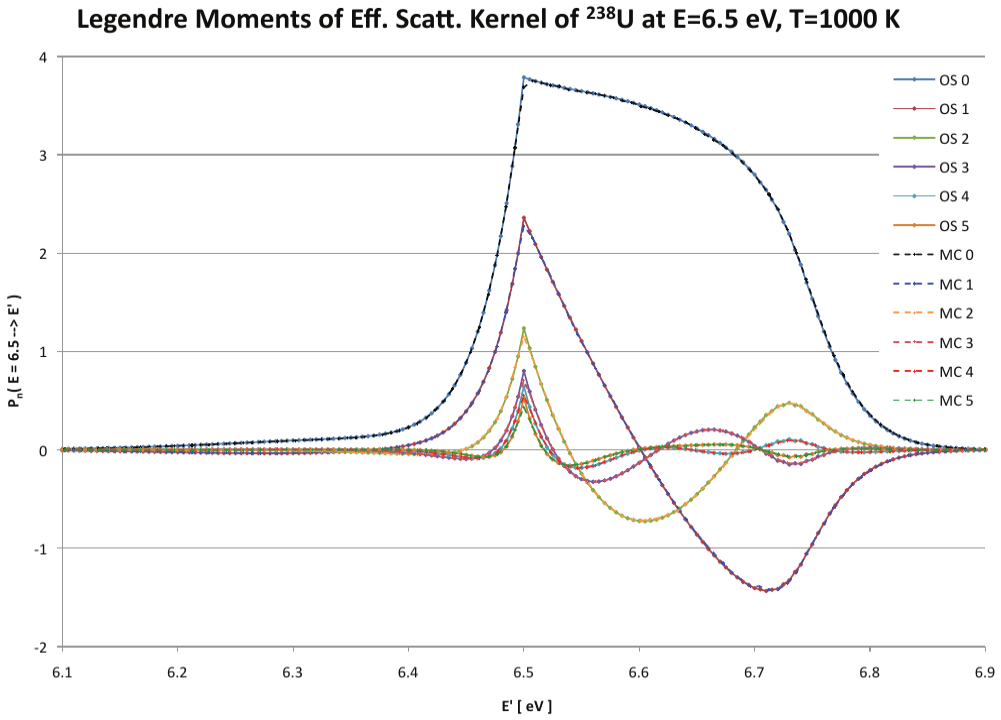

Figure 3.1: A plot of the first six Legendre moments computed by Arbanas compared to those via the Monte Carlo method.

Section 4.1.2, which provides results obtained by Becker [20] as he implemented the DBRC approach into MCNP.

Implementing the DBRC method into MCNP resulted in a -346 pcm difference in the eigenvalue when compared to the standard MCNP case in a criticality calculation for a standard light water reactor pin cell at 1200 K. The reason for this decrease in reactivity is shown by Becker to be increased capture in the lower energy resonances as shown in Table 3.1. The increased capture rate is explained by the increased upscattering into the absorption resonances. For a high temperature reactor whole core simulation using TRISO particles centered in a graphite matrix at 1200K, Becker calculated a -231 pcm impact on the reactivity.

Becker concluded that the DBRC algorithm was successfully integrated into MCNP. However, he notes that the primary drawback with this approach is increased

Table 3.1: Capture reaction rates of LWR pin cell at 1200 K

Energy bin (eV)	Capture reaction rate r [arb. Unit]		Differences
	std. MCNP	DBRC	
4.0 – 9.88	1.108E-02	1.110E-02	0.22%
9.88 – 16.0	4.129E-04	4.117E-04	-0.28%
16.0 – 27.7	6.173E-03	6.311E-03	2.24%
27.7 – 48.1	4.799E-03	5.062E-03	5.48%
48.1 – 75.5	2.328E-03	2.370E-03	1.18%
75.5 – 149	4.227E-03	4.249E-03	0.53%

computational time. As of the publication of this dissertation, DBRC has not been enabled in any publicly available MCNP release.

3.3 Improving Multigroup results using DBRC

The methods from Section 3.1 could be used to directly change the scattering kernels in the multigroup cross-section library [23], however a different, simpler, approach can be taken to readily estimate the impact of the new scattering kernel in deterministic codes. Lee [24] implemented DBRC in a Monte Carlo infinite-medium neutron slowing down code, MCSD. This code performs a Monte Carlo simulation of neutrons slowing down in the resolved resonance energy range and permits elastic scattering to be modeled with DBRC either on or off. Lee also developed a method for capturing the physics of the exact scattering kernel and generating cross sections for use in downstream deterministic codes. His method has been incorporated into the resonance treatment of CASMO-5 (for details on SCALE's resonance treatment see Section 2.4). Note that Lee did not use the DBRC method in his Monte Carlo code as discussed in Section 4.1.2, but rather a weighted method that will not be discussed here.

In order to capture the effect of DBRC, MCSD performs two major types of tallies. The first is the group-wise scalar flux, tallied as

$$\phi_g = \sum_{E_j \in g} dw_j \,, \tag{3.4}$$

where $d = -\frac{\ln(1-r)}{\Sigma_t}$, r is a random number, and w_j is a weight. The second tally is a group-wise reaction rate for interaction type α, tallied as

$$R_{\alpha g} = \sum_{E_j \in g} \sigma_\alpha dw_j \,. \tag{3.5}$$

Using these tallied quantities, the group absorption cross section is calculated by

$$\sigma_{ag} = \frac{R_{ag}}{\phi_g} \,, \tag{3.6}$$

and the absorption resonance integral is computed as

$$I_{ag} = \frac{\sigma_b}{\sigma_{ag} + \sigma_b} \sigma_{ag} \,, \tag{3.7}$$

where σ_b is the user-defined background cross section which excludes the potential cross section of the resonance isotope itself.

Using his method, Lee was able to calculate and compare the upscatter percentage to the results given by Ouisloumen [22]. His results are shown in Table 3.2. As can be seen from the table, the upscatter percentage is very high when the scattering collision occurs just below a ^{238}U resonance, and much lower when it occurs above the resonance. Since most codes don't account for any upscatter above the thermal cutoff, this will have a significant impact on the reactivity.

Lee used the new resonance integrals calculated from Equation 3.7 to generate a new cross section library for CASMO-5. Using this library he ran CASMO-5 on

Table 3.2: Upscatter percentage at 1000 K

Resonance (eV)	Neutron energy (eV)	Ouisloumen	Lee (σ)
6.67	6.52	82.03	83.40 (0.04)
	7.20	28.12	28.20 (0.01)
36.67	36.25	54.23	55.28 (0.06)
	37.20	7.95	7.26 (0.01)
661.14	659.00	1.42	1.18 (0.03)
	664.00	0.84	0.74 (0.00)

Table 3.3: Reactivity effect of exact scattering kernel

Fuel temp. (K)	Enrichment (w/o)	k (Asymptotic)	k (Exact)	Diff. (pcm)
300	4	1.25994	1.25963	-31
	8	1.40550	1.40519	-30
	12	1.46695	1.46668	-28
900	4	1.23609	1.23401	-209
	8	1.38006	1.37794	-212
	12	1.44122	1.43921	-201
1350	4	1.22298	1.21947	-352
	8	1.36643	1.36284	-358
	12	1.42775	1.42434	-340

a typical Light Water Reactor (LWR) pin cell and the results, shown in Table 3.3, agree with other uses of the exact scattering kernel (see Section 3.2).

3.4 One-Dimensional Doppler Broadening

Current work on OTF Doppler broadening has been limited to the MCNP computer code. MCNP has done a lot of work in recent years to find an efficient way to Doppler broaden one-dimensional cross sections [25–28].

MCNP takes the approach where, for each cross section at every energy, the temperature dependence is expanded as a functional expansion in temperature. This is done for every nuclide and every cross-section type that is subject to Doppler broadening. These expansion coefficients are a function of isotope, cross-section type, and energy grid point E_g. Using the capture cross section as an example, the temperature expansion would be

$$\sigma_\gamma(T, E_g) \approx \sum_{i=1}^{N} \frac{a_{g,i}}{T^{i/2}} + \sum_{i=1}^{N} b_{g,i} T^{1/2} + c_g \,, \tag{3.8}$$

where $a_{g,i}$, $b_{g,i}$, and c_g are the expansion coefficients.

These expansion coefficients are determined by a multi-step process that starts with constructing a unionized energy grid for an isotope. This unionized energy grid must contain all energy points required for an isotope and must be able to be used for all of the broadened cross sections for that isotope while still maintaining satisfactory agreement with the exact cross section values. The creation of a unionized energy grid is important because, as the temperature increases, Doppler broadening (see Section 2.2) of the isotope means that less energy points are required for the resonance peak, but more are required for the wings and tails. By only adding points, it is ensured that the unionized grid created will work for all temperatures and cross section type.

After a unionized energy grid has been created, the Doppler broadened cross sections are determined at every energy point using NJOY-derived routines that implement Cullen's exact Doppler broadening equation (Equation 2.5). This is done over a set of temperatures, separated by some small ΔT_{fit} (usually around 10 K). The grid created by these temperatures is usually more fine than that used to create the unionized energy grid. During this step, exact Doppler broadened cross sections are tabulated on the ΔT_{fit} temperature grid for each energy on the unionized energy grid.

Once the Doppler broadened cross sections have been calculated at every temperature, the expansion coefficients from Equation 3.8 can be determined. An

expansion for a given cross section type at a given energy can be evaluated for all temperatures on the temperature grid to yield a system of linear equations $\boldsymbol{Ax} = \boldsymbol{b}$. In this system, the vector $\boldsymbol{b}$ contains the cross sections at each temperature, $\boldsymbol{x}$ is the vector of the coefficients, and each row of the matrix $\boldsymbol{A}$ holds the values of the temperature corresponding to the elements in a given row raised to the powers of the expansion. Equation 3.9 illustrates this in matrix form. Such a system can generally be solved relatively easily. A discussion of the problems that arose while solving the system is given in a paper by Wilderman [28].

$$\begin{pmatrix} T_1^{-N/2} & T_1^{-(N-1)/2} & \cdots & T_1^{(N-1)/2} & T_1^{N/2} \\ T_2^{-N/2} & T_2^{-(N-1)/2} & \cdots & T_2^{(N-1)/2} & T_2^{N/2} \\ \vdots & \vdots & \ddots & \vdots & \vdots \\ T_{N_T-1}^{-N/2} & T_{N_T-1}^{-(N-1)/2} & \cdots & T_{N_T-1}^{(N-1)/2} & T_{N_T-1}^{N/2} \\ T_{N_T}^{-N/2} & T_{N_T}^{-(N-1)/2} & \cdots & T_{N_T}^{(N-1)/2} & T_{N_T}^{N/2} \end{pmatrix} \begin{pmatrix} a_{g,1} \\ \vdots \\ c_g \\ \vdots \\ b_{g,N} \end{pmatrix} = \begin{pmatrix} \sigma(T_1, E_g) \\ \sigma(T_2, E_g) \\ \vdots \\ \sigma(T_{N_T-1}, E_g) \\ \sigma(T_{N_T}, E_g) \end{pmatrix} \tag{3.9}$$

By using this method Wilderman was able to achieve cross sections that were within 0.1% of those calculated by NJOY with little impact on the code run time. The main drawback of the MCNP approach is that these OTF coefficients have to be calculated and stored. Currently MCNP does not make OTF libraries available with their production code; however, they do provide a tool for the user to generate them.

3.5 Kinematics Doppler Broadening

Not much work has been done on OTF or pre-Doppler broadening of the kinematics (two-dimensional data). Some work has been done by Trumbull [29] in pre-broadening the incoherent inelastic thermal scattering (see Section 2.6) for use in the MC21 Monte Carlo code developed at Bechtel Marine Propulsion Corporation.

In MC21, direct sampling of the $S(\alpha, \beta)$ data is used in a format nearly identical to that described in previously published work [30]. Two conditional PDFs are

derived in order to sample the energy transfer, β, and momentum transfer, α, given an incident neutron energy (see Section 7.1). MC21 performs interpolation on the integrated scattering cross section, energy transfer, and momentum transfer distributions functions such that

$$\sigma_s(E,T) = \sigma_s(E,T_i) + \frac{T-T_i}{T_{i+1}-T_i}[\sigma_s(E,T_{i+1}) - \sigma_s(E,T_i)]\,, \tag{3.10}$$

$$p(\hat{\beta}|E,T) = p(\hat{\beta}|E,T_i) + \frac{T-T_i}{T_{i+1}-T_i}[p(\hat{\beta}|E,T_{i+1}) - p(\hat{\beta}|E,T_i)]\,, \tag{3.11}$$

and

$$p(\hat{\alpha}|\beta,E,T) = p(\hat{\alpha}|\beta,E,T) + \frac{T-T_i}{T_{i+1}-T_i}[p(\hat{\alpha}|\beta,E,T_{i+1}) - p(\hat{\alpha}|\beta,E,T_i)]\,, \tag{3.12}$$

for $T_i < T \leq T_{i+1}$. It is important to note that the interpolation is performed on $\hat{\alpha}$ and $\hat{\beta}$, indicating that the α and β PDFs have undergone a transformation.

In the case of the α PDFs, the minimum and maximum values for a given energy transfer, as a function of T, are determined and a traditional unit-base normalization [31] is applied to obtain the $\hat{\alpha}$ PDFs. A slightly different approach is used for the β PDFs primarily to isoplate the quasi-elastic peak around $\beta = 0$. First, $\hat{\beta}$ is calculated by dividing by $|\beta_{\text{min}}|$,

$$\hat{\beta} = \frac{\beta}{|\beta_{\text{min}}|}\,. \tag{3.13}$$

The resulting down scattering $\hat{\beta}$ PDFs values range from -1 to 0 (a unit base), and the up scattering values range from $0 < \hat{\beta} \leq \frac{\beta_{\text{max}}}{|\beta_{\text{min}}|}$. Interpolation on the up scattering and down scattering portions are performed separately and then recombined back into a single $\hat{\beta}$ PDF.

Using this method, Trumbull was able to achieve good eigenvalue results for a variety of benchmarks. If the $S(\alpha,\beta)$ values were given at temperatures 50 K apart, then very good agreement was reached. When the temperatures were more than 100 K apart, the results started to diverge from expected values.

Chapter 4

Doppler Broadened Rejection Correction Method

The first feature to be added to KENO is the DBRC method. As mentioned in Section 2.6, neutron scattering has to be treated specially when the neutron is at thermal energies. For thermal moderators, there usually exists $S(\alpha, \beta)$ tables which help in calculating the thermal scattering cross section (see Table 2.1). However, there are many more materials that do not have $S(\alpha, \beta)$ tables, and these materials still need to have correct scattering behavior in the thermal energy range. This is currently done by using the Free Gas Thermal Treatment.

This chapter will discuss the current implementation of the free gas method, and highlight its current limitations and assumptions. After the assumptions have been discussed, the DBRC method will be introduced and it will be shown how it handles some of the assumptions made in the current method. Finally, the new method will be used to run some common cases and to compare results with results in current literature.

4.1 Free Gas Thermal Treatment

Above a certain thermal cutoff (typically around 5 eV), the target atom in a collision between an atom and a neutron can be considered at rest when compared with the velocity of the neutron. This aids in calculating results from elastic scatter as, once the angle has been sampled from an angular distribution, the exit energy of the neutron can be calculated from simple kinematics. However, below this thermal cutoff the collision between the neutron and the atom is affected by the thermal motion of the atom. In some cases, the collision is also affected by the presence of other atoms nearby. This thermal motion cannot be ignored without producing erroneous results, therefore KENO uses a free gas approximation to account for the thermal motion. This thermal approximation is the same as that used by the MCNP code [32].

The free gas thermal treatment in KENO assumes:

- That the medium is a free gas,
- Throughout the thermal range of interest, the elastic scattering cross section at zero Kelvin is nearly independent of the energy of the neutron, and
- That the reaction cross sections are nearly independent of temperature.

These assumptions allow the code to run quickly, but introduce some error when the scattering cross section varies (as it does in low energy resonances). With these assumptions, the free gas thermal treatment merely consists of taking into account the velocity of the target nucleus when the kinematics of a collision are being calculated. As such, this treatment will only apply to elastic scattering.

4.1.1 Sampling the Velocity of the Target Nucleus

The Sampling the Velocity of the Target Nucleus (SVT) method is the current method of choice for Monte Carlo codes that need to use the free gas approximation. In the SVT method, the target velocity is sampled and subtracted from the velocity of the

neutron to calculate the relative velocity. The collision is sampled in the target-at-rest frame and the outgoing velocities are transformed to the laboratory frame by adding the target velocity. KENO uses the SVT method if the energy of the neutron is greater than 5 eV and there is no other scattering data, such as $S(\alpha, \beta)$, available.

In the SVT method the effective scattering cross section is first represented in the laboratory system for a neutron of kinetic energy E as

$$\sigma_s^{\text{eff}}(E) = \frac{1}{v_n}\sigma_s(v_{\text{rel}})\, v_{\text{rel}}\, p(V)\mathrm{d}v\frac{\mathrm{d}\mu_t}{2}\,. \tag{4.1}$$

Here, v_{rel} is the relative velocity between a neutron moving with a scalar velocity v_n and a target nucleus moving with a scalar velocity V, and μ_t is the cosine of the angle between the neutron and the target direction-of-flight vectors. The equation for v_{rel} is

$$v_{\text{rel}} = (V_n^2 + V^2 - 2v_nV\mu_t)^{\frac{1}{2}}\,. \tag{4.2}$$

The scattering cross section at the relative velocity is denoted by $\sigma_s(v_{\text{rel}})$, and $p(V)$ is the probability density function for the Maxwellian distribution of target velocities,

$$p(V) = \frac{4}{\pi^{1/2}}\beta^3V^2e^{-\beta^2V^2}\,, \tag{4.3}$$

where β is defined as

$$\beta = \left(\frac{AM_n}{2kT}\right)^{\frac{1}{2}}\,, \tag{4.4}$$

and A is the mass of a target nucleus in units of the neutron mass, M_n is the neutron mass in MeV-sh^2/cm^2, and kT is the equilibrium temperature of the target nuclei in MeV.

By slightly rearranging Equation 4.1, we can obtain the probability distribution for a target velocity V and cosine μ_t using

$$p(V, \mu_t) = \frac{\sigma_s(v_{\text{rel}})v_{\text{rel}}\, p(V)}{2\sigma_s^{\text{eff}}(E)v_n}\,. \tag{4.5}$$

Here KENO makes the simplifying assumption that the variation of $\sigma_s(v_{\text{rel}})$ with target velocity can be ignored. MCNP (and by extension KENO) justifies this approximation in two ways:

1. For light nuclei, $\sigma_s(v_{\text{rel}})$ is slowly varying with velocity, and

2. for heavy nuclei, where $\sigma_s(v_{\text{rel}})$ can vary rapidly, the moderating effect of scattering is small so that the consequences of the approximation will be negligible.

Due to this approximation, we can rewrite the probability distribution as proportional to

$$p(V, \mu_t) \propto \sqrt{v_n^2 + V^2 - 2V v_n \mu_t} V^2 e^{-\beta^2 V^2} . \tag{4.6}$$

With some more manipulation, the above expression can be written as

$$p(V, \mu_t) \propto \frac{\sqrt{v_n^2 + V^2 - 2V V_n \mu_t}}{v_n + V} \left(V^3 e^{-\beta^2 V^2} + v_n V^2 e^{-\beta^2 V^2} \right) . \tag{4.7}$$

This is the final probability distribution to be sampled.

KENO divides the final probability distribution into two segments, to allow for faster sampling. This is outlined in the following algorithm that is used to sample the target velocity:

1. With probability $\alpha = 1/(1 + (\sqrt{\pi}\beta v_n/2))$ the target velocity V is sampled from the distribution $p_1(V) = 2\beta^4 V^3 e^{-\beta^2 V^2}$. By using the transformation $V = \sqrt{y}/\beta$ this becomes sampling the distribution $p(y) = y e^{-y}$.

2. With probability $1 - \alpha$, the target velocity is sampled from the distribution $p_2(V) = (4\beta^3/\sqrt{\pi}) V^2 e^{-\beta^2 V^2}$. By using $V = \sqrt{y}/\beta$ the distribution can be reduced to sampling the distribution $p(y) = (4/\sqrt{\pi}) y^2 e^{-y^2}$.

3. The cosine of the angle between the neutron velocity and the target velocity is sampled uniformly on the interval: $-1 \leq \mu_t \leq 1$.

4. The rejection function is computed using

$$R(V, \mu_t) = \frac{\sqrt{v_n^2 + V^2 - 2V v_n \mu_t}}{v_n + V} \leq 1 \,. \tag{4.8}$$

If the sampling is rejected, the procedure is repeated. The minimum efficiency of this rejection algorithm is around 68%, but it approaches 100% as either the incident neutron energy approaches zero or becomes much larger than kT.

Once the velocity of the target nucleus and the angle of the scatter have been determined, the kinematics of the scattering reaction can be determined as before from the kinematics equations.

4.1.2 Doppler Broadened Rejection Correction

The DBRC method serves to eliminate the approximation used to develop Equation 4.6. Recall that KENO used the approximation that the variation of the cross section $\sigma_s(v_{\text{rel}})$ with respect to the relative speed v_{rel} can be ignored. The idea behind the DBRC method is that one can sample the pair (V, μ_t) from the exact distribution by resorting to an additional rejection algorithm that takes into account the correlation between angle and velocity precisely due to the constraint imposed by the term $\sigma_s(v_{\text{rel}})$ [15, 17]. To see this, note that Equation 4.5 can be identically rewritten as

$$p(V, \mu_t) = C \frac{\sigma_s(v_{\text{rel}})}{\sigma_0^{\max}(v_\xi)} \frac{v_{\text{rel}}}{v_n + V} (v_n + V) p(V) \,, \tag{4.9}$$

where

$$C = \frac{\sigma_0^{\max}(v_\xi)}{2 v_n \sigma_s^{\text{eff}}(E)}$$

is a normalization constant [20]. $\sigma_0^{\max}(v_\xi)$ is the largest elastic scattering cross section (at temperature 0 K) on an energy interval in proximity of the actual value $\sigma_s^{\text{eff}}(E)$. Usually this energy interval is in the range $\xi \pm 4$, where ξ is a dimensionless neutron speed $\xi = \sqrt{AE/kT}$. As in Equation 4.7, we can rewrite the probability distribution

as

$$p(V,\mu_t) \propto \frac{\sigma_s(v_{\text{rel}})}{\sigma_0^{\max}(v_\xi)} \frac{\sqrt{v_n^2+V^2-2Vv_n\mu_t}}{v_n+V} \left(V^3 e^{-\beta^2V^2} + v_n V^2 e^{-\beta^2V^2}\right) . \tag{4.10}$$

Note that the only difference between this equation and Equation 4.7 is the addition of a new rejection term.

With the addition of the rejection term

$$R_{\text{DBRC}} = \frac{\sigma_s(v_{\text{rel}})}{\sigma_0^{\max}(v_\xi)} \leq 1 , \tag{4.11}$$

the sampling algorithm described in Section 4.1.1 becomes:

1. Apply the first four steps described in Section 4.1.1 to generate a test pair (V,μ_t).

2. Compute the ratio R_{DBRC}, which depends on the test pair (V,μ_t). If the rejection test is satisfied, accept the pair; otherwise, reject the pair and restart from above by sampling a new pair from the SVT algorithm.

One important impact of the DBRC method is that, in the proximity of resonances, it might lead to an extensive number of rejections. This will, in turn, slow down the Monte Carlo simulation, leading to a noticeable rise in the amount of time it takes for the Monte Carlo simulation of approximately 10% for most reactor physics calculations.

4.2 Implementation into KENO

Implementing DBRC into KENO is a relatively straightforward task, as KENO already uses the SVT algorithm for its free gas thermal treatment. Figure 4.1 shows the path of the cross-section reading and collision routines within KENO. The routines/modules that need to be modified to implement the DBRC method are only read_pointwise, nuclide_type, sample_reaction, and sample_freegas.

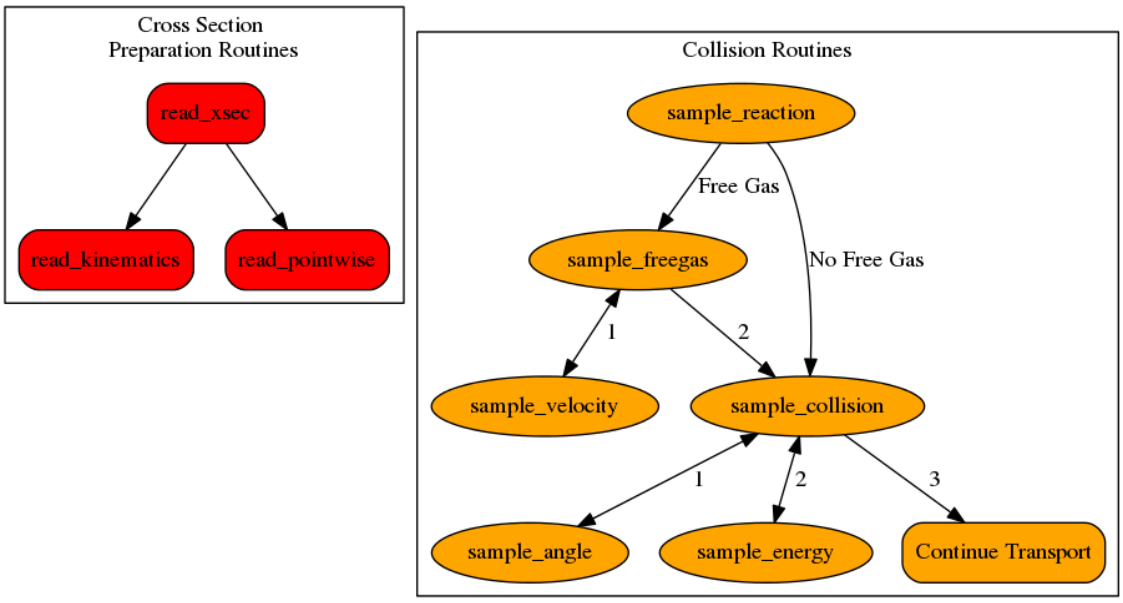

Figure 4.1: Routines for cross section preparation and collisions in KENO.

4.2.1 read_pointwise

For DBRC, the sampling and rejection equations of Section 4.1.2 require the scattering cross sections of the material at the temperature 0 K (also known as the temperature-independent cross sections). However, KENO only reads in the temperature-dependent cross sections because it was assumed that would be all required. In fact, AMPX did not even originally produce the temperature-independent scattering cross sections for any isotope in the CE libraries.

The temperature-independent scattering cross section files were created for a few isotopes of interest (typically heavy isotopes) in a simple (E, σ_s) tabular format. read_pointwise was modified to read in these new files, if they exist, if the user wishes to utilize the DBRC method. The files can be in either little- or big-endian format.

4.2.2 nuclide_type

The nuclide_type module implements a container that holds all the material cross sections and other data. This container needed to be updated to hold the new temperature-independent data that is read in by read_pointwise for the DBRC method. A flag which indicated whether or not the DBRC data is present and should be used was also added.

4.2.3 sample_reaction

Subroutine sample_reaction is the routine that determines whether free gas sampling is used. Originally for free gas sampling to be used the energy of the neutron had to be below a thermal cutoff (typically 5-10 eV), $S(\alpha, \beta)$ data had to not exist for the material of interest, and free gas sampling had to be enabled by the user. The coding changes extend the energy range where the free gas sampling is applied – if the user has set DBRC to be enabled. The new energy range can be changed by the user, but the default is to extend up into the epithermal range (210 eV). Above 210 eV there is little effect [33].

4.2.4 sample_freegas

The subroutine sample_freegas needed to be modified to use the new algorithm discussed in Section 4.1.2. The modifications made to the algorithm in sample_freegas are shown in Figure 4.2.

It is important that all calculations (that of $\sigma_{\max}$ and the rejection test) are done using the temperature independent data read in by the modified read_pointwise.

4.3 Results

In order to test the DBRC implementation a variety of cases will be run. The main area of interest with regards to the DBRC method is that of temperature dependence.

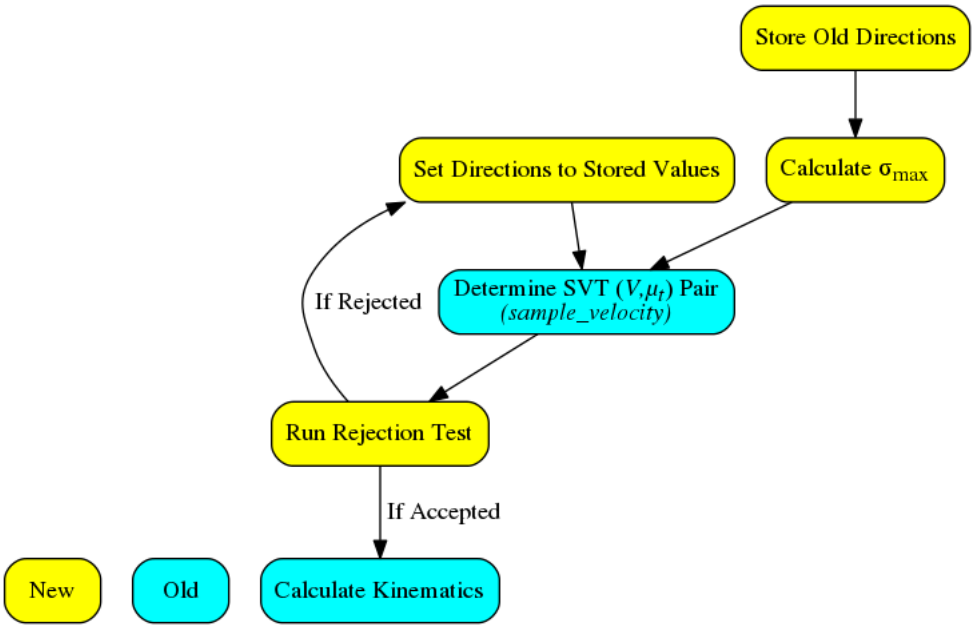

Figure 4.2: DBRC algorithm in KENO.

It is expected that as the temperature increases, the impact of the DBRC method will also increase. That is, as the temperature increases the difference between the reference eigenvalue and the new, DBRC enabled, eigenvalue will also increase. This is due to the motion of the target nucleus causing additional upscatter (and therefore absorption in the resonances) as the temperature goes up. Initially, we will look at the impact caused by ^{238}U and then expand to other heavy isotopes.

4.3.1 Becker LWR Pin Cell

The first case used to highlight the potential impact of the DBRC method is that of a simple LWR pin cell. For this model, the pin cell is reflected on all sides and is not part of a larger bundle. This model was chosen specifically to compare with results established by Becker [20] when he originally implemented the DBRC method into MCNPX. A representation of the model created by NEWT [34] is shown in Figure 4.3.

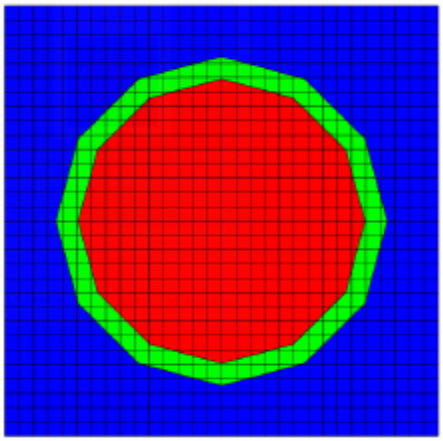

Figure 4.3: LWR Pin Cell (NEWT).

This pin cell consists of 4% enriched UO_2 surrounded by a Zircalloy cladding, cooled by light water. The fuel temperature will be varied to give a good representation of the DBRC effects. The original source of this model is the thesis of Dr. Bjorn Becker, who created a MCNPX model to demonstrate the effectiveness of the DBRC method. It was adapted to MCNP5 and KENO for use in this dissertation.

Table 4.1 shows the results of the DBRC runs at different temperatures for both MCNP5 and KENO, and Figure 4.4 plots the results for the KENO runs. As can be seen from the table and chart, the effect of DBRC increases greatly as the temperature increases. This is expected because as the temperature increases, the thermal motion of the target nuclide (^{238}U in this case) also increases. This causes additional upscatter and absorption in the absorption resonances. At lower temperatures, such as 293 K, the impact is within the standard deviation of the eigenvalue, and we can safely assume that DBRC has little to no effect.

KENO and MCNP have similar differences in pcm as the temperature increases, even though the eigenvalues are different. This is due to differences in the CE libraries and CE treatments presented by both MCNP and KENO. Therefore the difference in the eigenvalues is not unexpected. The extra run-time imposed by activating the DBRC method is about 5-10% in KENO. However, the runtime in KENO can be

Table 4.1: DBRC - Temperature Results

Temperature (K)	MCNP5 No DBRC	MCNP5 DBRC	Difference (pcm)	KENO No DBRC	KENO DBRC	Difference (pcm)
293	1.34918 (0.00014)	1.34914 (0.00014)	-3	1.34454 (0.00015)	1.34434 (0.00015)	-15
600	1.33474 (0.00013)	1.33397 (0.00014)	-58	1.33033 (0.00015)	1.32949 (0.00015)	-63
900	1.32423 (0.00013)	1.32243 (0.00014)	-136	1.31974 (0.00015)	1.31770 (0.00014)	-155
1200	1.31539 (0.00014)	1.31228 (0.00014)	-237	1.31060 (0.00015)	1.30737 (0.00015)	-247
2400	1.28529 (0.00014)	1.27710 (0.00014)	-639	1.28102 (0.00016)	1.27461 (0.00016)	-502

longer if the temperature independent library created for the DBRC method is large. In order to ensure a quicker runtime, care must be taken to ensure that the data prepared for the DBRC method does not extend too far past the energy range of interest (210 eV).

The initial run was done using ^{238}U for DBRC since results could then be compared with those obtained by Becker using MCNPX. After this initial comparison, additional temperature independent libraries were created for various heavy nuclides. The additional nuclides were: ^{232}Th, ^{234}U, ^{235}U, ^{236}U, ^{237}Np, ^{239}Pu, and ^{240}Pu. The pin cell model discussed above contains a few other uranium isotopes, and the results of activating DBRC for these additional isotopes (when compared with just activating DBRC for ^{238}U) are given in Table 4.2. As can be seen from the table, activating DBRC for the additional uranium isotopes has little to no effect.

4.3.2 CASL LWR Pin Cell

In order to more fully test the impact of additional isotopes being included for use with DBRC, another pin cell was obtained. This pin cell, christened the CASL LWR

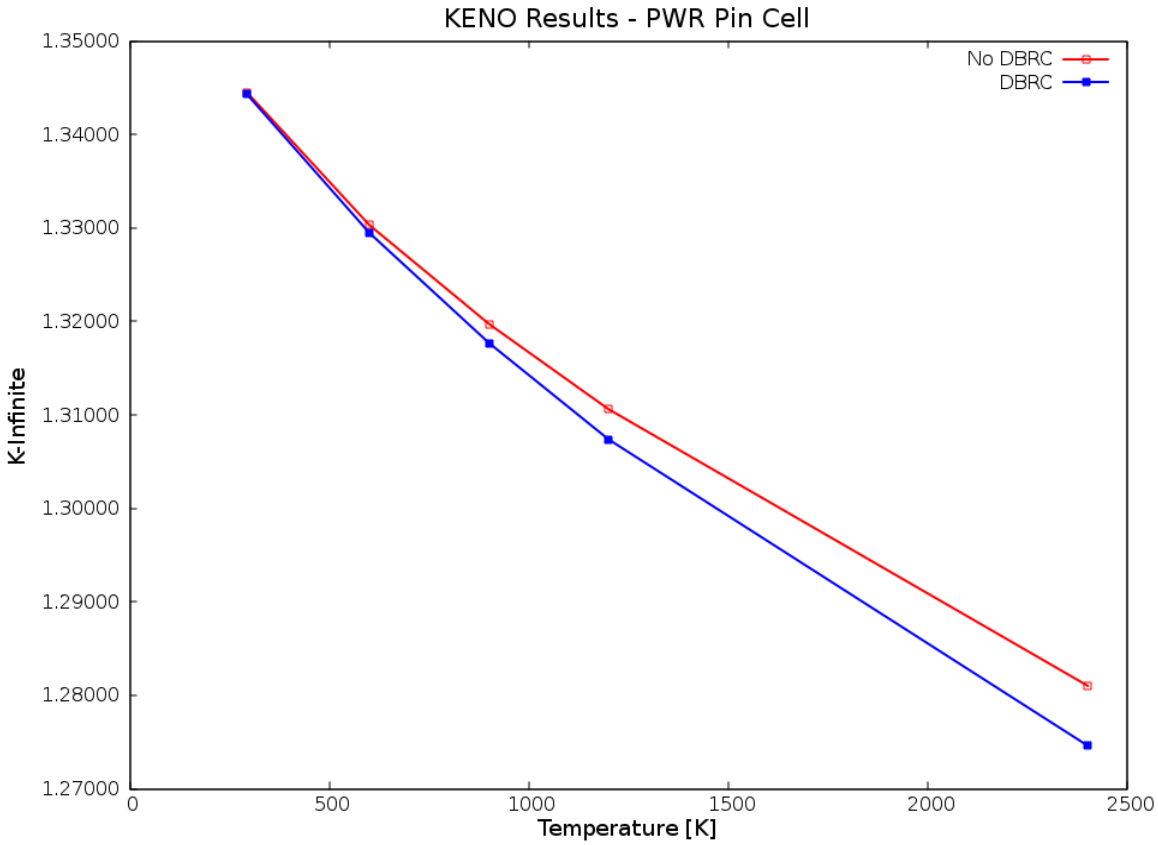

Figure 4.4: DBRC KENO results.

pin cell, has a large variety of fission and activation products and therefore has many heavy nuclides contained within it. The CASL pin cell is also available at a wide range of burn-ups, so the impact of DBRC as fuel depletes can begin to be examined.

The CASL pin cell is very similar to the pin cell described in Section 4.3.1, but it contains additional trace isotopes as a result of depletion. The enrichment of uranium also changes as the fuel is depleted. The results of running this case at the beginning of the cycle and comparing no DBRC, DBRC for ^{238}U only, and DBRC for all available isotopes is shown in Table 4.3.

It is clear that the effect of using the DBRC method on ^{238}U is the most pronounced, while using DBRC for the other isotopes present has little to no effect.

Table 4.2: DBRC Extra Istopes Results

Temperature (K)	^{238}U Only	Other Uranium	Difference (pcm)
293	1.34434	1.34444	7
	(0.00015)	(0.00017)	
600	1.32949	1.32931	-14
	(0.00015)	(0.00016)	
900	1.31770	1.31755	-11
	(0.00014)	(0.00015)	
1200	1.30737	1.30714	-18
	(0.00015)	(0.00015)	
2400	1.27461	1.27489	22
	(0.00016)	(0.00015)	

Table 4.3: DBRC Results for CASL Pin Cell

Temperature (K)	KENO No DBRC	KENO U-238 Only	Difference (pcm)	KENO All DBRC	Difference (pcm)
293	1.22557	1.22543	-11	1.22535	-6
	(0.00007)	(0.00007)		(0.00007)	
600	1.21141	1.21031	-91	1.21024	-6
	(0.00007)	(0.00007)		(0.00007)	
900	1.20081	1.19882	-166	1.19873	-8
	(0.00007)	(0.00007)		(0.00007)	
1200	1.19173	1.18864	-260	1.18866	1
	(0.00007)	(0.00007)		(0.00007)	
2400	1.16320	1.15650	-577	1.15643	-6
	(0.00007)	(0.00007)		(0.00007)	

This could be due to several reasons, but the main cause is the fact that ^{238}U is the most abundant isotope in most reactor simulations. While enabling DBRC for the other isotopes does not have much impact on reactivity, it also does not have much impact on the run time. This is also due to the lack of abundance of these isotopes.

The CASL pin cell was provided at a wide variety of burnup steps at a fuel temperature of 900 K. As the fuel burns, it is expected that the amount of fission

Table 4.4: DBRC Results for Depleted CASL Pin Cell

Time Step (d)	No DBRC	DBRC (U-238)	Diff (pcm)	DBRC (All)	Diff (pcm)
2.862	1.197471	1.195348	-177	1.195476	-167
5.729	1.194393	1.192413	-166	1.192589	-151
8.596	1.192100	1.190117	-166	1.190026	-174
11.464	1.190018	1.188183	-154	1.188220	-151
14.331	1.188463	1.186389	-175	1.186418	-172
28.626	1.182667	1.180729	-164	1.180673	-169
57.208	1.172105	1.170232	-160	1.170039	-176
114.361	1.148144	1.146248	-165	1.146238	-166
171.514	1.124543	1.122632	-170	1.122520	-180
228.667	1.102619	1.100779	-167	1.100717	-173
285.819	1.082642	1.080758	-174	1.080670	-182
357.258	1.059709	1.058074	-154	1.057729	-187
428.697	1.038822	1.037326	-144	1.036965	-179
500.135	1.019624	1.017987	-161	1.017700	-189
571.574	1.001736	0.999991	-174	0.999772	-196
714.441	0.969048	0.967438	-166	0.967130	-198
857.308	0.939481	0.938019	-156	0.937747	-185
1000.175	0.913160	0.911677	-163	0.911393	-194
1143.042	0.889782	0.888535	-140	0.888204	-178
1285.909	0.869539	0.868078	-168	0.867792	-201
1428.776	0.851499	0.850413	-128	0.850066	-168
1571.643	0.836409	0.834805	-192	0.834618	-214
1714.510	0.823151	0.821845	-159	0.821504	-200
1857.377	0.811744	0.810380	-168	0.810165	-195
2000.244	0.801964	0.800846	-140	0.800418	-193

products and activation products will increase. This should increase the impact of enabling DBRC for all isotopes, as there will be more of them to affect the reactivity. Unfortunately, the cases run will be merely snapshots of the DBRC effect. The fuel pin was not actively depleted with DBRC enabled. An attempt to examine the impact of actively depleting with DBRC enabled will be discussed in Section 4.3.3. The results obtained from running the CASL pin cell are shown in Table 4.4 and plotted in Figure 4.5. There is a slight impact in turning DBRC on for all isotopes

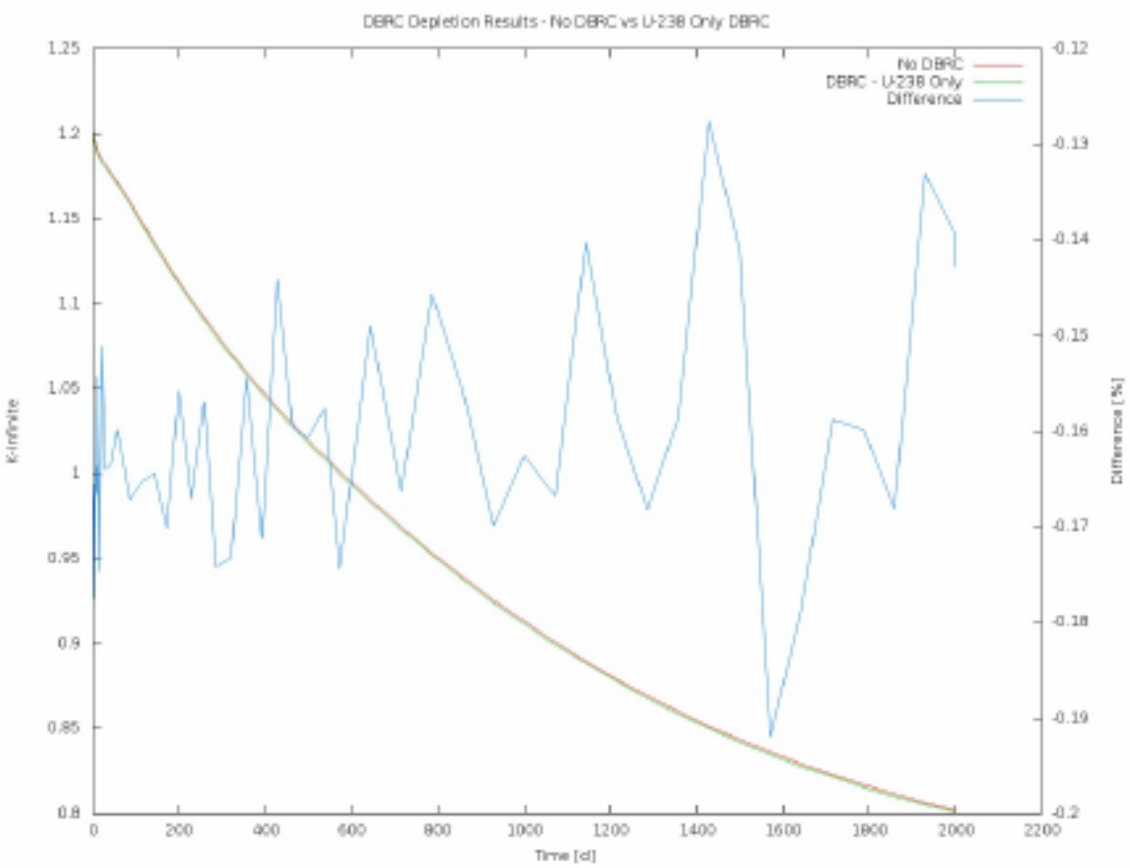

Figure 4.5: DBRC KENO results for CASL Pin Cell.

as the fuel depletes, but it is not very significant.

4.3.3 CANDU Bundle

Another model of interest is that of the CANDU reactor. Most CANDUs use 37-element fuel bundles that contain natural uranium and are cooled and moderated by high purity heavy water. While CANDUs do not generally operate at high enough temperatures that show the most effect from using the DBRC method, it will still be interesting to see what effects occur as the CANDU model can be depleted. The NEWT representation of a CANDU 1/4 bundle is shown in Figure 4.6.

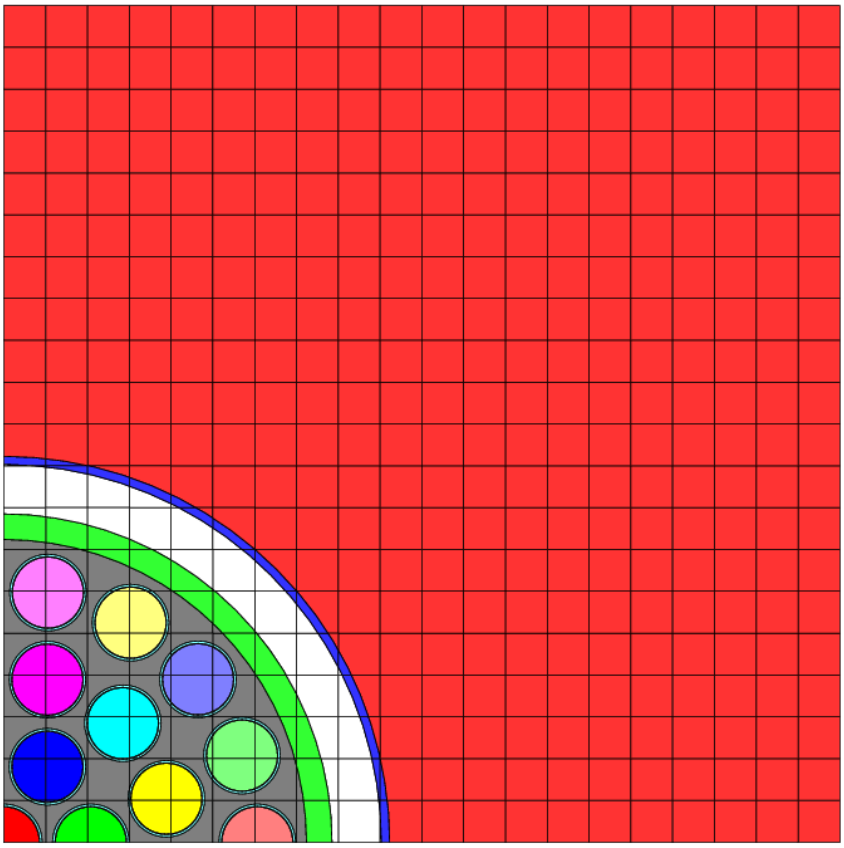

Figure 4.6: CANDU 1/4 Bundle.

The source of the CANDU model is a HELIOS [35] model provided by the Canadian Nuclear Safety Commission (CNSC). It was converted to a SCALE model and used originally to compare SCALE and NESTLE against HELIOS and NESTLE. Since CANDUs have a slightly larger amount of ^{238}U, it is thought that the effect of the new scattering method will have a discernible impact. However, since the temperature of the CANDU bundle is generally not very high, this impact might be limited.

Since the CANDU model is a NEWT model, a MG library will have to be constructed that contains the effects of using DBRC. The method used to construct

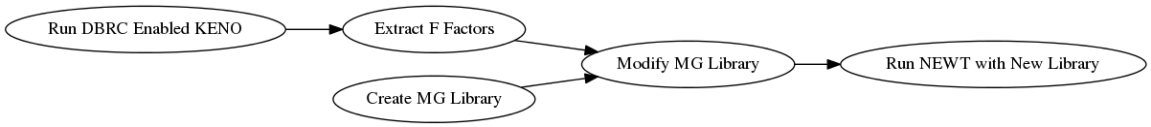

Figure 4.7: Multi Group DBRC Steps.

this library is similar to that used by Lee [24] and discussed in Section 3.3. A quick chart of the steps used in the method is shown in Figure 4.7.

Initially, a 169-group MG library was created. This library has a group structure that is similar to the 252-group structure created in SCALE (discussed in [7]) but, rather than having a fine group structure everywhere, there exists only one energy group per ^{238}U resonance. This results in a lower number of groups; the new library only contains 169 groups compared to the original 252. In parallel to the library creation, a variety of KENO cases were run to obtain ^{238}U absorption reaction rates for a variety of background cross sections. These reaction rates can be divided by the flux to obtain the absorption cross section, and then be divided by the infinitely dilute cross section to obtain the F Factors (see Section 2.4.1). It is important to only have one energy group (or F Factor) per resonance, as this will allow the absorption reaction rates to capture the effect of the DBRC method.

The results from the NEWT/TRITON [36] run with the created library are shown in Figure 4.8. As can be seen from the results, the impact of DBRC on the CANDU bundle is fairly insignificant. This could be due to a number of factors, including the low temperature of the case and the composition of the fuel. Regardless, it is interesting to note that there is the expected decrease in k-infinity at the start of the cycle due to the increase in upscatter and absorption in the resonances. As the fuel depletes, the case with the DBRC created MG library actually decreases in eigenvalue slower than that with the original library. This causes the case run with the new library to have a higher k-infinity at the end of the cycle than that of the

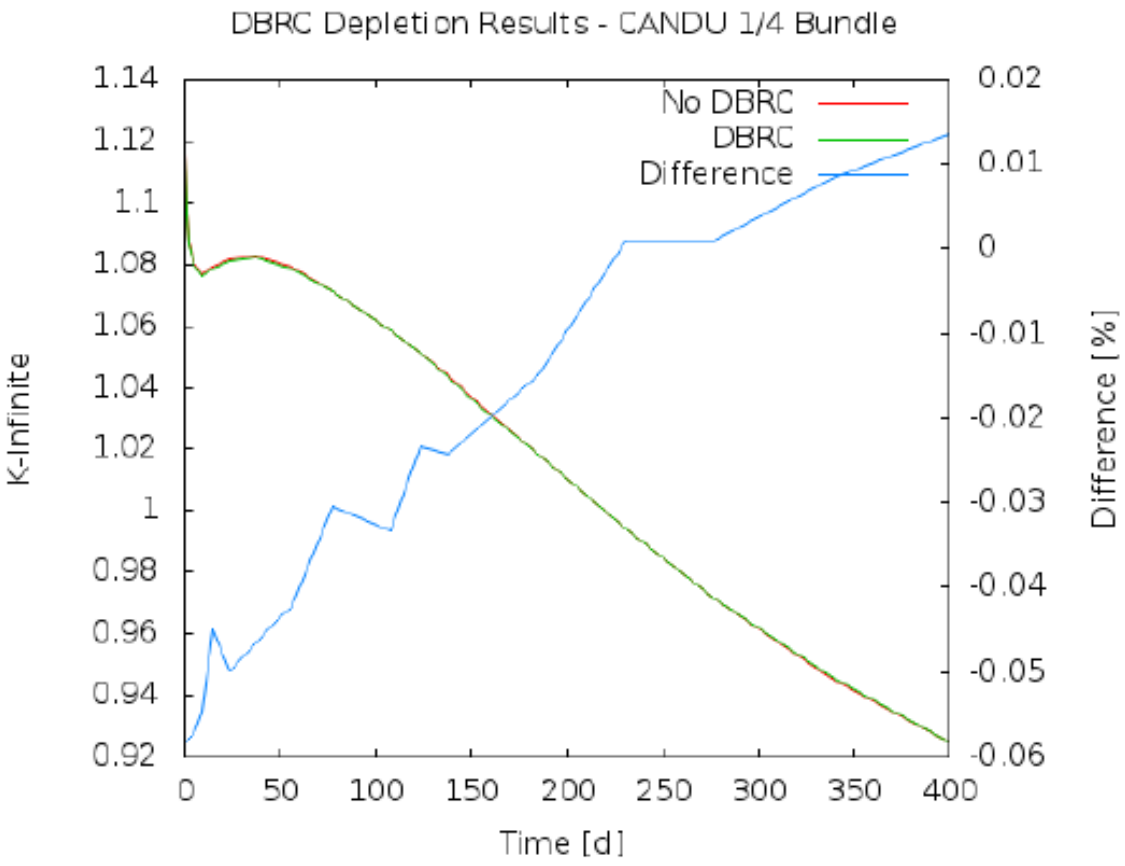

Figure 4.8: CANDU - DBRC depletion results.

original library. However, the difference is extremely small (around 0.15%) and more cases should be run to test this at a higher temperature.

4.3.4 Mosteller Benchmark

The final case examined for the DBRC method is that of a Doppler-defect benchmark created by Mosteller [37]. This benchmark consists of a set of computational benchmarks for the Doppler reactivity defect. The benchmark also serves as a test for the Doppler coefficient of reactivity, since it is simply the reactivity defect divided by the change in fuel temperature.

The benchmark specifications contain corresponding pairs of pin cells for hot zero power (HZP) and hot full power (HFP) conditions. At HZP, the temperature for everything – fuel, cladding, and borated moderator – is a uniform 600 K. At HFP, the fuel temperature is 900 K, while the temperature of everything else is still 600 K. The Doppler defect is calculated as the reactivity difference between HFP and HZP conditions. The Doppler coefficient of reactivity is then determined as

$$DC = \frac{\Delta\rho_{Dop}}{\Delta T_{Fuel}}\,, \tag{4.12}$$

where DC is the Doppler coefficient of reactivity, ΔT_{Fuel} is 300 K, and the Doppler defect is

$$\Delta\rho_{Dop} = \frac{k_{HFP} - k_{HZP}}{k_{HFP} \times k_{HZP}}\,. \tag{4.13}$$

There are three subsets of benchmarks, each using a different type of fuel. For this dissertation, only the first subset (containing UO_2 fuel) will be examined. The geometry for the benchmark is an infinite array of identical, infinitely long Pressurized Water Reactor (PWR) fuel pin cells with no axial variation. The fuel is assumed to be pure UO_2 with no impurities or fission products present. The enriched uranium fuel is assumed to contain only ^{234}U, ^{235}U, and ^{238}U, with the ^{234}U content proportional to the ^{235}U concentration. The cladding is assumed to be pure zirconium, with no minor constituents of Zircaloy present. A final assumption is that the presence of any structural materials can be ignored. A schematic of the benchmark is given in Figure 4.9 and a full description of the materials is given in the reference.

The results of running the UO_2 benchmark in KENO are shown in Table 4.5 and the Doppler defects are plotted in Figure 4.10. The results from these runs are consistent with those given in the benchmark paper, and show that the Doppler coefficient is generally less negative when DBRC is ignored.

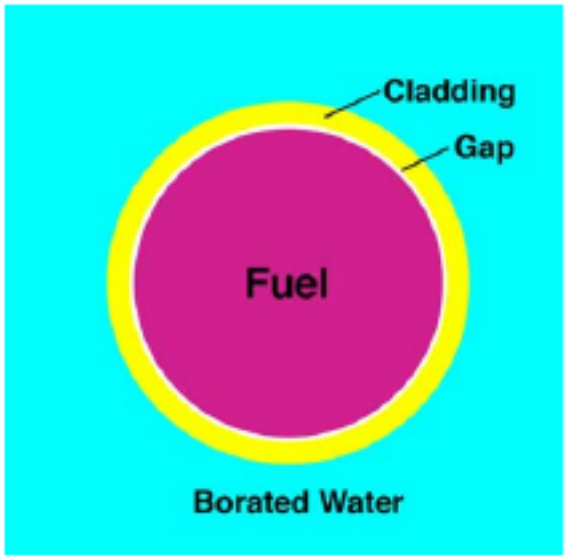

Figure 4.9: Mosteller fuel pin.

Table 4.5: Mosteller Benchmark UO_2 Results

Enrichment (%)	HZP: No DBRC	DBRC	HFP: No DBRC	DBRC
0.711	0.66602 ± 10	0.66547 ± 10	0.65981 ± 10	0.65908 ± 10
1.6	0.96129 ± 11	0.96041 ± 12	0.95270 ± 12	0.95131 ± 11
2.4	1.09940 ± 11	1.09867 ± 11	1.08989 ± 12	1.08818 ± 11
3.1	1.17744 ± 11	1.17652 ± 11	1.16736 ± 11	1.16565 ± 11
3.9	1.24010 ± 11	1.23906 ± 11	1.22997 ± 11	1.22792 ± 12
4.5	1.27562 ± 12	1.27452 ± 11	1.26513 ± 11	1.26311 ± 11
5.0	1.29967 ± 11	1.29883 ± 11	1.28943 ± 10	1.28738 ± 12

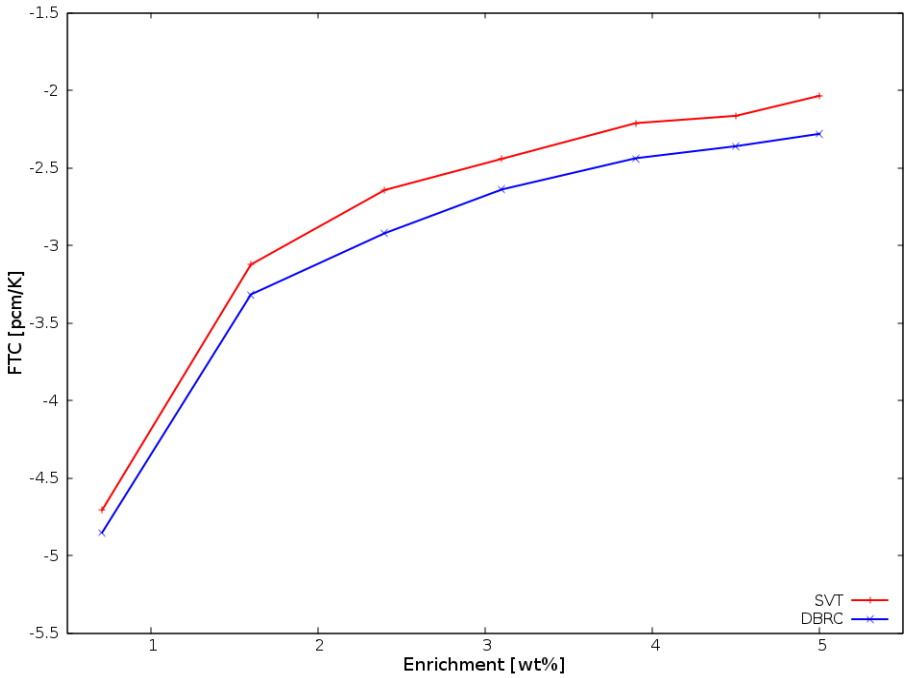

Figure 4.10: Doppler defect for Mosteller UO_2 Benchmark.

Chapter 5

One-Dimensional Problem Dependent Doppler Broadening

The next feature to be added to KENO is the ability for KENO to generate one-dimensional temperature- and problem-dependent cross sections using a computationally efficient method for Doppler broadening. Recall from Section 2.2 that calculating the Doppler broadened cross sections takes an unacceptable amount of time for a quick Monte Carlo calculation. In order to combat this, a finite difference method has been developed [38] that greatly increases the speed at which cross sections can be Doppler broadened at the expense of some accuracy.

This chapter will briefly discuss this finite difference method and showcase its current limitations. The implementation of this method into KENO will be shown and how it relates to the rest of the AMPX-created cross sections will be discussed. Finally, various synthetic cases will be run, including a full reactor assembly, to highlight the impact that this problem-dependent Doppler broadening can have on real reactor problems.

5.1 Finite Difference Method for Doppler Broadening

The approach to be implemented into KENO is a finite-difference method, which is well suited for resonance analysis and LWR reactor applications. This approach, based on an approximation of the exact Doppler broadening equation developed by Cullen known as the Solbrig kernel (see Section 2.2), can be represented by

$$E\bar{\sigma}(E) = \frac{1}{2\sqrt{\pi\xi}} \int_0^\infty \mathrm{d}u' u' \left[\exp\left(\frac{-(u-u')^2}{4\xi} \right) - \exp\left(\frac{-(u+u')^2}{4\xi} \right) \right] \sigma(u'), \quad (5.1)$$

where $u = \sqrt{E}$ and $\xi = \frac{mkT}{2M}$.

Defining $F(u,\xi) = E\bar{\sigma}(E)$ and $\zeta = 2\xi$ allows Equation 5.1 to be represented in terms of the second-order differential equation

$$\frac{\partial^2 F}{\partial u^2} = \frac{\partial F}{\partial \zeta}. \quad (5.2)$$

Then, because of the initial condition $F(u,0)$ for $-\infty < u < \infty$ and the boundary conditions $F(\infty,\zeta) = F(\infty,0)$ and $F(-\infty,\zeta) = F(-\infty,0)$, the function F can be calculated using the finite-difference method.

The application of the finite-difference method solves Equation 5.2 by applying an explicit finite-difference formalism assuming constant meshes with $\sigma u = h$ and $\sigma\zeta = \gamma$. The first and second derivatives can then be expanded in a Taylor's series. Thus, the explicit finite-difference equation for the function F at any u_i and ζ_{j+1} is

$$F_i^{j+1} = s(F_{i+1}^j + aF_i^j + F_{i-1}^j), \quad (5.3)$$

where $s = \frac{\gamma}{h^2}$ and $a = \frac{1-2s}{s}$. The finite-difference equation in Equation 5.3 can be modified for non-uniform meshes as

$$F_i^{j+1} = s\left(aF_i^j + \frac{2(F_{i-1}^j \delta v_r + F_{i+1}^j \delta v_l)}{\delta v_r + \delta v_l}\right), \tag{5.4}$$

where $s = \frac{\gamma}{\delta v_l \delta v_r}$, $a = \frac{1-2s}{s}$, $\delta v_l = v_i - v_{i-1}$, $\delta v_r = v_{i+1} - v_i$, and v_i is the momentum at the i^{th} grid point.

Selecting a ΔT that is small (such as 1K) allows for agreement within 0.1% to reference cross sections across all energies, except for very low and very high energies. The increase in error at the edges of the energy range is due to limitations in the finite-difference method. Since each element in the energy grid uses the surrounding elements to calculate the next value, the finite-difference method produces poor cross-section estimates when surrounding elements are inaccurate or nonexistent. In an attempt to alleviate these errors, extra points can be added past the known energy range. This reduces the error for cross sections at very high and very low energies by interpolating the known cross-section data, but does not eliminate it completely.

Figures 5.1 and 5.2 show the results of using the finite-difference method to obtain cross sections for the ^{238}U scattering reaction at two energies; near the 6.67 eV resonance at 750K, and at 900K near the tail region. As previously discussed, the error in the tail region quickly disappears as one moves away from the energy boundary.

5.1.1 Correcting Limitations

As seen in Figure 5.2b, the error at the low energy tail can approach 10%. While this probably has a negligible effect on the results, it would be beneficial to try and minimize this error. One solution is to use linear interpolation for the first five momentum points on the energy grid. Since there are no resonances in this extremely

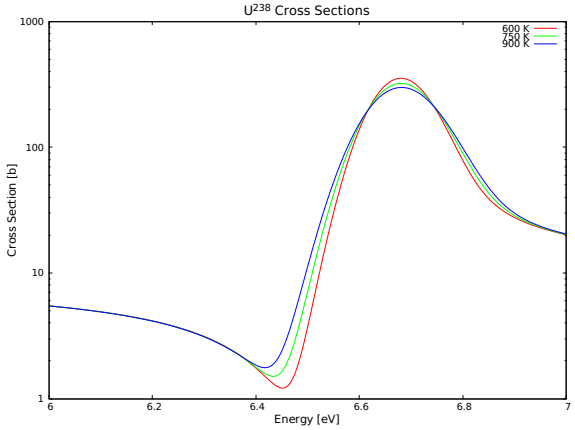

Figure 5.1: ^{238}U scattering cross sections showing a resonance.

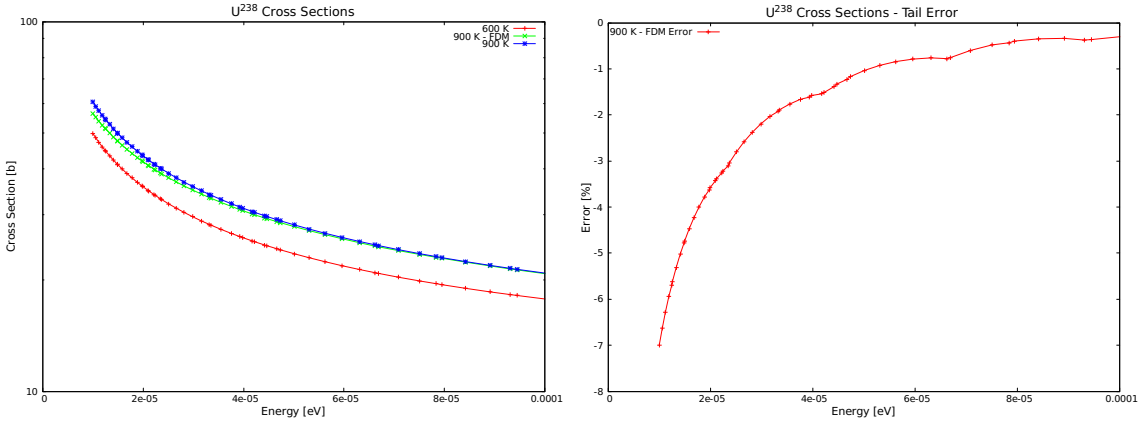

(a) Cross Sections (b) Error

Figure 5.2: ^{238}U scattering cross sections and error near low energy tail.

small energy range, this should not introduce any errors into the broadened cross sections.

An example of this approach is shown in Figure 5.3. In Figure 5.3a there is a large (approaching 10%) error in the lower tail region. This contrasts sharply with the lack of error in the rest of the energy space, although there is a small error when using the finite difference method around the resonances. In Figure 5.3b the error

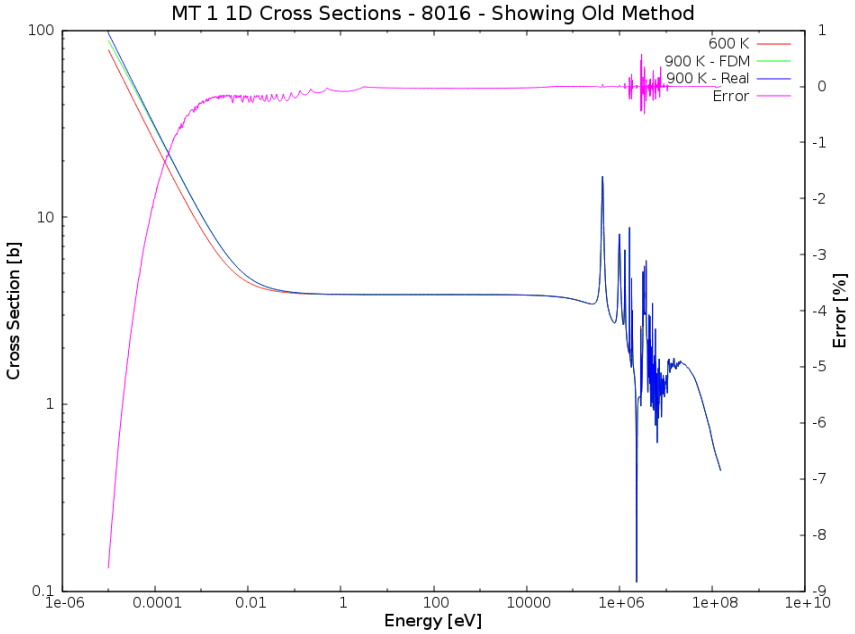

(a) Old Method

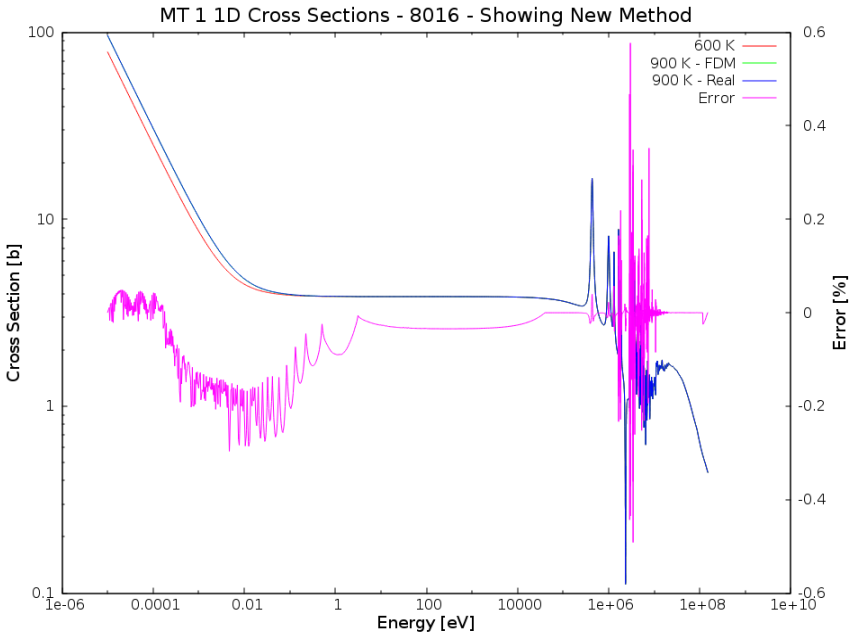

(b) New Method

Figure 5.3: Differences in ^{16}O σ_t cross sections with new and old methods.

has mostly disappeared and is now less than 0.2% in the tail region. The rest of the energy range is mostly unaffected by the change.

Another potential problem arises when dealing with isotopes that don't have a large resonance structure. One example is the one-dimensional cross sections of ^{1}H. As can be seen in Figure 5.4, there are no resonances for ^{1}H. This is a common feature in thermal moderator one-dimensional cross sections. Unfortunately, the energy structure of these cross sections tend to lead to numerical instability in the finite difference method used to Doppler broaden the cross sections. This can be easily seen in Figure 5.4a, where the Doppler broadened cross sections actually exceed the higher temperature cross sections in the low energy range.

In order to remedy this problem, interpolation over the entire energy range can be used. This should not introduce significant error due to the lack of resonances in the cross sections. Results from this interpolation are shown in Figure 5.4b. Since this approach corrects the problem, interpolation should be used for Doppler broadening the one-dimensional cross sections instead of the finite difference method for isotopes with no resonance structure.

5.2 Probability Tables

The next step in the pre-broadening process is to examine the pre-broadening of the probability tables. Like the 1D cross sections, these tables are prepared at a number of predetermined temperatures. Unlike the 1D cross sections, there are typically only a few dozen tables (of a few dozen points each) for each isotope. This means that any operation chosen to pre-broaden the data should be quick and should not significantly impact the runtime of the transport calculation.

The approach chosen to pre-broaden the probability tables is that of simple linear-logarithmic interpolation. This approach is practical due to the low number of points, and because the data does not change nearly as much as data in the resolved resonance region. Since the impact of increasing temperature on the probability tables lessens

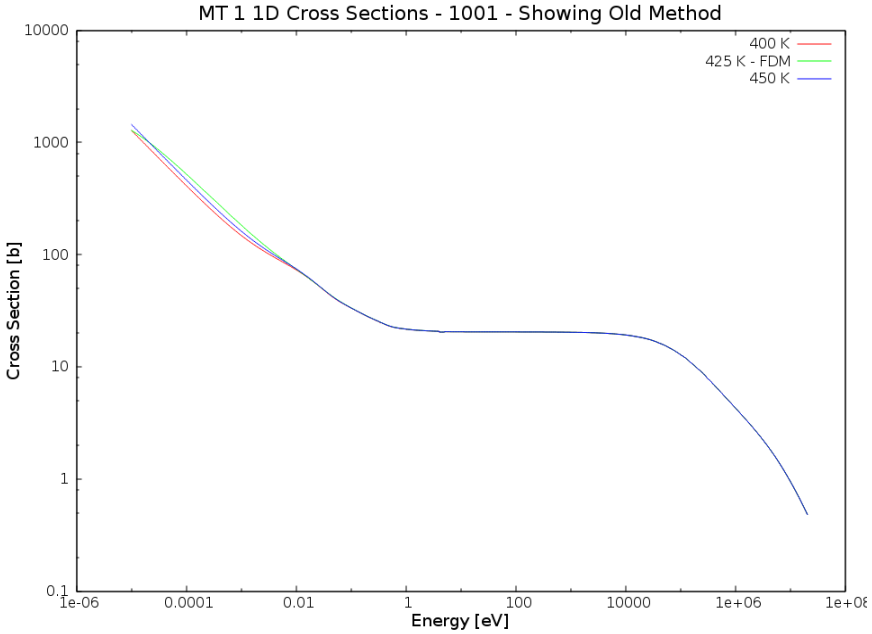

(a) Old Method

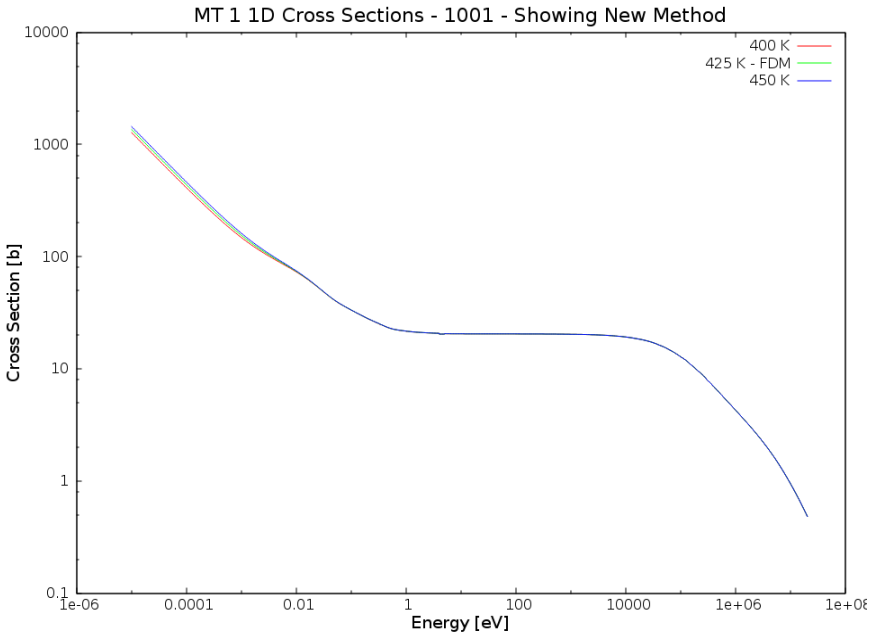

(b) New Method

Figure 5.4: Differences in ^{1}H σ_t cross sections with new and old methods.

as the temperature increases, logarithmic interpolation is performed on the square root of temperature. Thus, we can determine a probability at temperature T_i as

$$y_i = y_1 + \frac{\log\left(\frac{T_i}{T_1}\right)(y_2 - y_1)}{\log\left(\frac{T_2}{T_1}\right)}. \tag{5.5}$$

Using Equation 5.5 results in a typical error in the probability tables of around 0.1% for most energies. However, as the energy increases, the accuracy of the probability table decreases. This is due to insufficient sampling of the data that constructs the probability table. In the upper energy regions, the error for the interpolation can be slightly over 1%. This error is still acceptable for the same reason that the original data is insufficiently sampled and rarely used in LWR reactor calculations.

5.3 Implementation into KENO

Implementing the one-dimensional and probability table problem-dependent Doppler broadening routines into KENO involves slightly modifying the current cross-section reading routines and then adding the Doppler broadening routines on to the end of the cross section processing. This is highlighted in Figure 5.5, which shows the program flow KENO uses to read in cross sections for one nuclide. As can be seen in the figure, the cross-section routines are completely linear in nature. Therefore, it was relatively straightforward to add the new routines to the end and Doppler broaden after the original data was read in to memory.

5.3.1 Modifications to Existing Routines

The original routines had to be modified to store data that is required to Doppler broaden the cross sections to the desired user temperature.

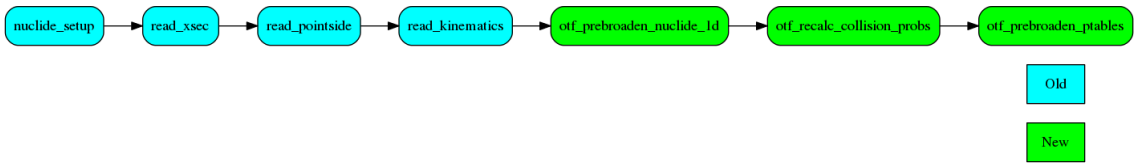

Figure 5.5: Cross-section processing routines.

nuclide_setup

This routine is modified to store the desired temperatures before they are overwritten by temperatures that are available on the cross-section libraries. This is required so that KENO knows what temperature to Doppler broaden to. This routine is only called once per KENO run; it serves as the master subroutine that calls read_xsec for each required nuclide.

read_xsec

The subroutine read_xsec contains the code that controls the cross-section reading in process. Modifications made here include determining the available temperatures, the reference library, and whether or not Doppler broadening is required. For example, if a user requests ^{238}U at 900 K, Doppler broadening is not required since AMPX libraries are already available for this isotope and temperature.

The end of this subroutine contains calls to the actual reading routines. After the reading routines, subroutine calls to the Doppler broadening routines occur sequentially as shown in Figure 5.5.

read_pointwise

The one-dimensional cross-section reading routine was modified to store the reaction numbers of the temperature-dependent cross sections. This allows the Doppler broadening routines to know which reactions need to be Doppler broadened.

5.3.2 New Routines

otf_prebroaden_nuclide_1d

This subroutine controls the Doppler broadening of the one-dimensional cross sections. It will open a second cross-section library file that bounds the desired user temperature. For example, if the user wants ^{16}O cross sections at 675 K, KENO will have already opened the 600 K library; this routine will then open the 900 K library so that the the user desired 675 K temperature is bounded by both available temperature libraries.

Once both libraries are open, the code will loop through all of the temperature-dependent cross section reaction types. For each reaction, it will pass the cross-section data through to a C++ routine that performs the finite-difference method to Doppler broaden as described in Section 5.1. During this process, the original cross sections that were read in by KENO are overwritten by the Doppler broadened cross sections. One effect of overwriting the cross sections from the original library is that the energy grid stays the same as that of the original data. Generally, as temperature increases, points are added or removed from the energy grid in order to ensure that the cross-section error is low when doing interpolation between energy points. By using the same energy grid as the original data some fidelity might be lost. However, this is not expected to be an issue as the energy grid will still be the same as the closest temperature; if the cross sections are broadened from the original temperature independent data then this issue will have to be revisited.

otf_recalc_collision_probs

After the one-dimensional cross sections are Doppler broadened, the collision probabilities (see Section 2.3.1) will need to be recalculated. This subroutine accomplishes this task for all collision probability reactions that are present in the library. This subroutine will also recalculate redundant reactions if they exist. In this case, redundant reactions means reactions for which cross sections can be calculated

by summing up the cross sections from other reactions that are already known. For thermal moderators, the redundant reactions are not recalculated; only the collision probabilities are recalculated.

otf_prebroaden_ptables

If the nuclide being Doppler broadened has probability tables, they are Doppler broadened to the correct temperature in this routine. This routine loops through all of the probability tables and uses the methods described in Section 5.2 to interpolate them to the desired temperature. One limitation arises when an energy exists on the reference library, but not the bounding library. If this occurs, then the closest energy on the reference library is reused, instead of interpolating to the desired temperature.

Support Utilities

Various other quick utility functions and variables were created and placed into the modules otf_vars and otf_utils. otf_vars contains global variables that are important to the overall Doppler broadening process (location of libraries, desired user temperature, etc.). otf_utils contains quick functions such as linear interpolation, library opening, and summation routines. These routines are generally used in several different places in the Doppler broadening process and are too small to need their own module.

5.4 Results

In order to test the impact of the one-dimensional problem dependent Doppler broadening, a variety of test cases were run. Some cases from Chapter 4 will be reused, and some new cases that are described here will be utilized.

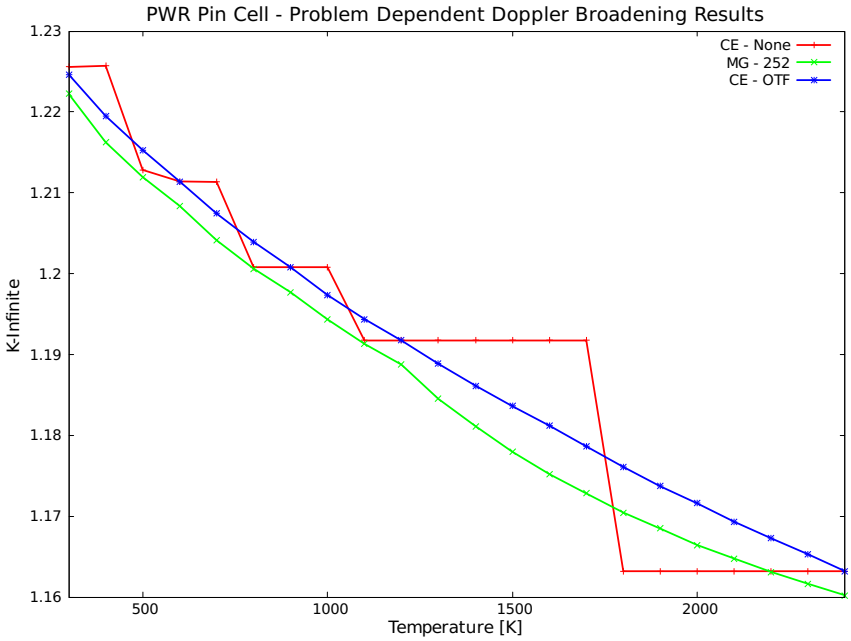

Figure 5.6: Results for CASL pin cell showing impact of problem-dependent Doppler broadening.

5.4.1 CASL Pin Cell

The first case reuses the pin cell model from Section 4.3.2. Before problem-dependent Doppler broadening was implemented, KENO would simply use cross sections at the closest temperature that was present on the libraries with no interpolation. For example, if the user specified 760 K, KENO would use 900 K. As can be seen in Figure 5.6, this leads to nonphysical "steps" in the eigenvalue behavior versus temperature as the library changes.

The multigroup 252 group library results are also shown in Figure 5.6. Currently, KENO uses linear interpolation to temperature-adjust the multigroup libraries, and including these results allows for a comparison with the Doppler broadening approach. The Doppler broadening implementation in KENO uses currently available libraries as reference points for the finite-difference equation/interpolation. This approach

Table 5.1: Eigenvalue results for pin cell depletion at different temperatures.

Depletion		Eigenvalue			
Burnup [GWd/MTHM]	Time [d]	900 K	1000 K	1100 K	1200 K
0.000	0.0	1.31920	1.31590	1.31280	1.30980
0.032	1.0	1.28540	1.28220	1.27930	1.27660
2.300	72.0	1.24840	1.24570	1.24290	1.24030
6.780	212.0	1.19730	1.19450	1.19220	1.18920
11.300	352.0	1.15130	1.14920	1.14650	1.14360
15.700	492.0	1.11140	1.10910	1.10650	1.10400
20.200	632.0	1.07400	1.07270	1.07020	1.06790
24.700	772.0	1.03980	1.03890	1.03710	1.03430
29.200	912.0	1.00770	1.00730	1.00610	1.00390
33.700	1052.0	0.97700	0.97790	0.97670	0.97470
38.100	1192.0	0.94890	0.94980	0.94930	0.94690
42.600	1332.0	0.92200	0.92360	0.92380	0.92170

explains why the eigenvalues agree at the reference library temperatures in Figure 5.6 (293 K, 600 K, 900 K, 1200 K, and 2400 K).

Depletion Effects

To demonstrate the impact of Doppler broadening on depletion calculations, the pin cell was depleted to a burnup of 42.6 GWd/MTH. A variety of temperatures were used, and the results are shown in Table 5.1. As shown in the table, the impact of the temperature decreases as the fuel is burned. This effect can be attributed to the homogeneous nature of the temperature; a reactor would provide different results.

5.4.2 Radial and Axial Temperature Effects

In order to better understand the effect of radial and axial temperature profiles in a fuel pin, two additional pin cell models were created. These pin cells are very similar to the one described previously, but one has nine radial temperature regions and the

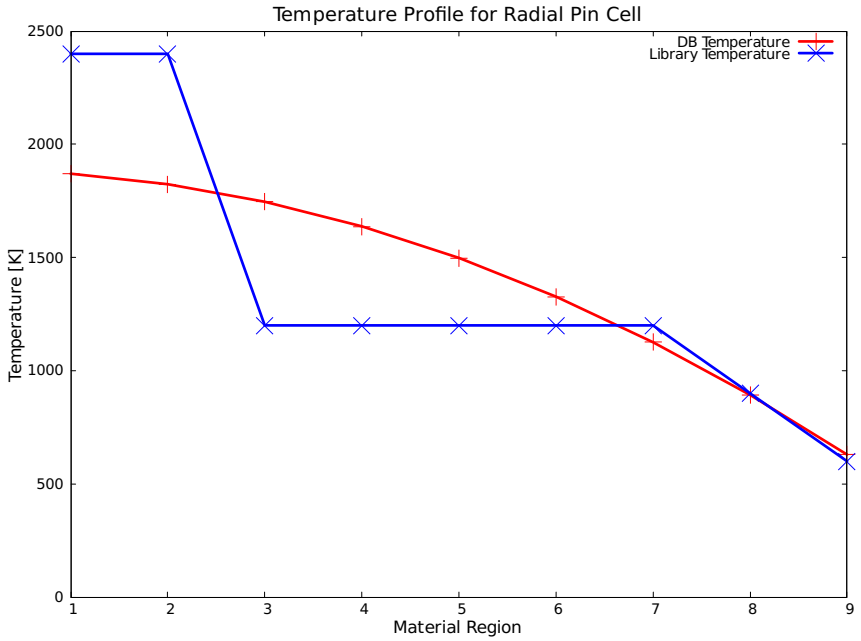

Figure 5.7: Radial temperatures for the fuel pin model.

Table 5.2: Eigenvalue results for pin cell with different radial temperatures.

	No DB	DB	Difference [pcm]
Eigenvalue (σ)	1.31489 (0.00015)	1.31260 (0.00014)	-174

other has nine radial temperature regions and nine axial temperature regions (total of 81 different temperature regions). These pin cells were designed to closely mimic the temperature profile found in an operating reactor.

Figure 5.7 shows the radial temperature profile used in the first case along with the temperatures used in KENO without problem-dependent Doppler broadening. The impact of Doppler broadening on the eigenvalue is shown in Table 5.2, where σ is the statistical uncertainty of k-effective from the Monte Carlo run.

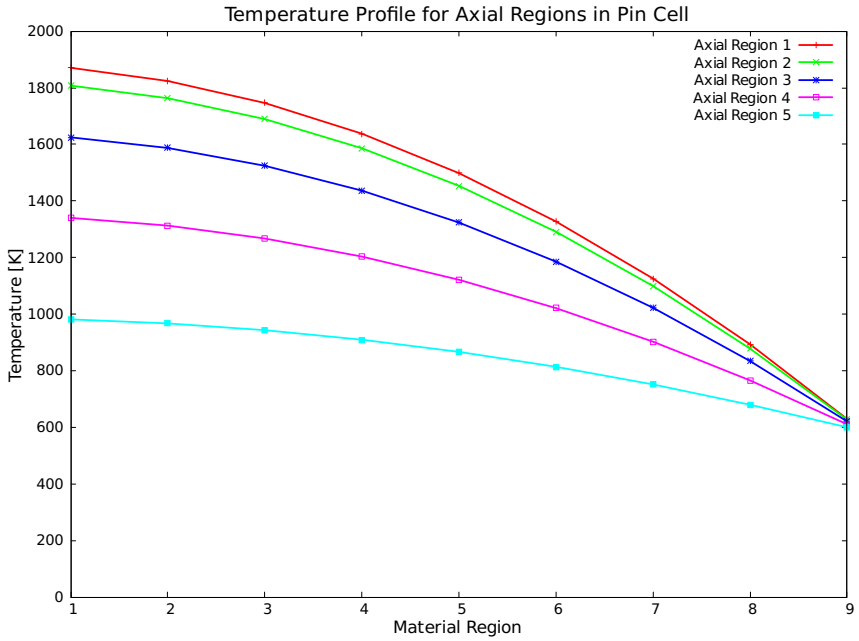

Figure 5.8: Radial temperatures for each axial region of pin cell.

For the case where the both the axial and radial temperatures vary, the temperature profiles in both the axial and radial directions are shown in Figure 5.8. Axial region 1 is the center axial region of the fuel pin, with axial region 2 being the region directly above and below it, etc. Only the first five regions are shown because the temperature profile is symmetric. Eigenvalue results are shown in Table 5.3.

For both cases the overall impact is to lower the eigenvalue. Referring back to Figure 5.6 shows that this is the expected behavior as temperature increases. Since the net effect of the radial and axial profiles is to increase the average pin cell temperature, the eigenvalue should be lower than that of the non-Doppler broadened case.

5.4.3 3D Assembly

The next test case used is that of a full 3D assembly shown in Figure 5.9. The fuel assembly uses low-enriched uranium and has 18 different temperatures along the

Table 5.3: Eigenvalue results for pin cell with different axial and radial temperatures.

	No DB	DB	Difference [pcm]
Eigenvalue (σ)	1.31623 (0.00014)	1.31387 (0.00015)	-179

Table 5.4: 3D assembly problem-dependent Doppler broadening results.

	MG 252	CE No DB	Difference MG vs. CE No DB [pcm]	CE DB	Difference MG vs. CE DB [pcm]
Eigenvalue (σ)	1.04323 (0.00003)	1.04617 (0.00005)	282	1.04424 (0.00005)	97

length of the fuel rods. The large number of fuel regions with different temperatures will highlight the effects of Doppler broadening on the cross sections. Traditional KENO calculations use the same cross sections for all 18 temperatures because all temperatures are near the same reference library. In this case, using the Doppler broadened cross sections results in a 193 pcm reduction in reactivity (difference in columns 4 and 6 in Table 5.4.

As seen in Table 5.4, using Doppler broadened cross sections creates a difference of several hundred pcm. The impact on the run time is minimal because all cross sections are Doppler broadened before any transport calculations are done. Most isotopes can be Doppler broadened in a few seconds, and the worst case scenario of ^{238}U takes less than one minute.

5.4.4 Aluminum Infinite Homogeneous Model

To test the impact of Doppler broadening of the probability tables, a hypothetical case was created where changes in the probability tables would have a significant

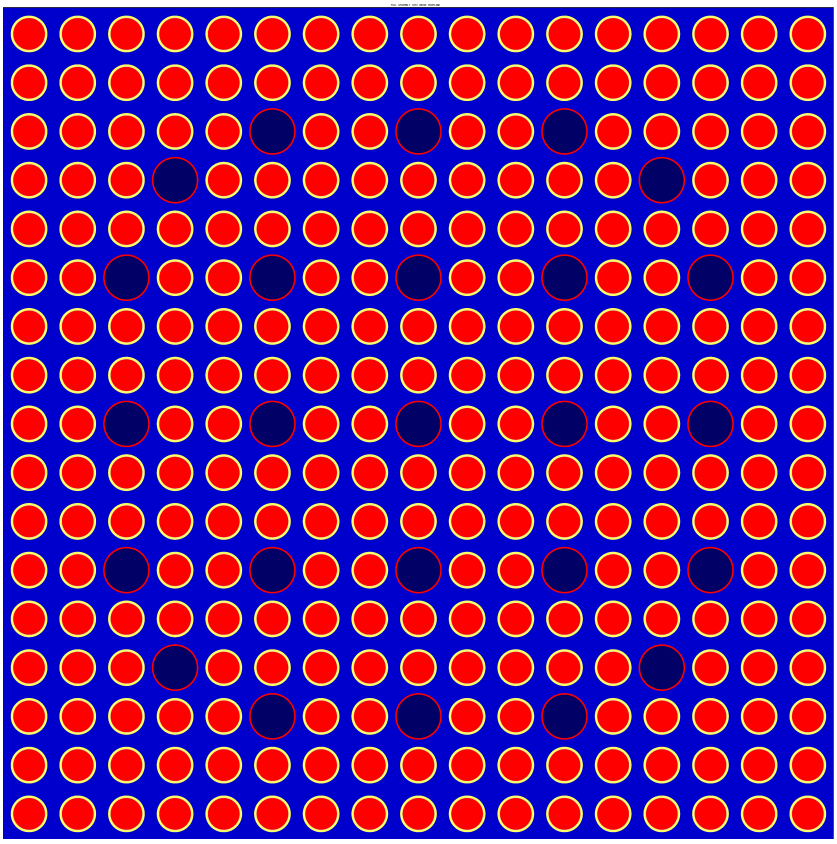

Figure 5.9: Radial view of 3D assembly model generated by KENO.

impact on the eigenvalue. In the pin cell and assembly cases discussed thus far, the Doppler broadening of the probability tables changed the eigenvalue by less than 5 pcm, which represents less than a one σ change for each system, so a different case was required. The case created is that of a 3% enriched uranium cube moderated by ^{27}Al at 1050 K. The results of enabling probability table broadening are shown in Table 5.5.

As can be seen in Table 5.5, the impact of Doppler broadening only the 1D cross sections is not very noticeable (only a 2σ difference). However, when the probability tables are also Doppler broadened, the eigenvalue significantly changes. Thus, the

Table 5.5: Infinite homogeneous aluminum model results.

	No DB	DB - 1D Only	Difference No DB vs. 1D DB [pcm]	DB - 1D and PTAB	Difference No DB vs. 1D and PTAB DB [pcm]
Eigenvalue (σ)	0.65350 (0.00009)	0.65347 (0.00010)	-21	0.65299 (0.00009)	-73

importance of correcting the probability tables for temperature is shown even when the impact may not be as large as that of the 1D cross sections.

Chapter 6

Two-Dimensional Problem Dependent Doppler Broadening

After the one-dimensional cross sections have been Doppler broadened, the next step is to Doppler broaden the two-dimensional cross sections (or kinematics data). The two-dimensional data is so named due to the fact that it is concerned with the cross sections that represent scattering from one energy to another energy. This gives rise to a two-dimensional array of data; cross sections of a specific incoming energy scattering to a variety of outgoing energies. This data is used for the thermal moderators, and is described more fully in Section 2.6.1. The way that KENO utilizes this data is described in Section 2.8.3.

This chapter will describe the broadening approach implemented into KENO and discuss the current limitations. Results will be shown for a variety of cases using different thermal moderators to highlight the impact that this kinematic Doppler broadening will have on reactor and pin cell problems.

6.1 Interpolation Method on Double Differential Probability Data

As mentioned in Section 2.8.3, KENO uses CDFs and PDFs of the double differential scattering cross sections. These PDFs and CDFs are stored on an AMPX CE library for use by KENO. During problem setup, KENO will open the CE library with the closest temperature to the model temperature, and use that data for all neutron interactions with the thermal moderator.

The Doppler broadening method implemented into KENO uses linear interpolation on the cosine of the scattering angle (μ) and energy (E) probabilities. For interpolation on μ, no extra manipulation needs to be done and the interpolated probability can be determined by

$$p(\mu|E_{in},T) = p(\mu|E_{in},T_i) + \frac{T-T_i}{T_{i+1}-T_i}\left[p(\mu|E_{in},T_{i+1}) - p(\mu|E_{in},T_i)\right] . \tag{6.1}$$

For the outgoing energy (E) probabilities, a traditional unit-base normalization [31] is applied before linear interpolation is done. The equation is then similar to Equation 6.1:

$$p(\hat{E}|\mu,E_{in},T) = p(\hat{E}|\mu,E_{in},T_i) + \frac{T-T_i}{T_{i+1}-T_i}\left[p(\hat{E}|\mu,E_{in},T_{i+1}) - p(\hat{E}|\mu,E_{in},T_i)\right] . \tag{6.2}$$

Typically the interpolation is done on either the CDF or PDF, and then the non-interpolated value is recalculated.

The unit-base normalization is required when the energy range of the exit energy probability distribution varies at different temperatures or incoming energies. Examining Figure 6.1, we can observe the major problem with Cartesian interpolation; the panel at E will have features from the lower panel at the low end, and from the upper panel at the high end. This will cause the resulting function to have artificial peaks when the distributions shift as a function of energy, as is usually the case.

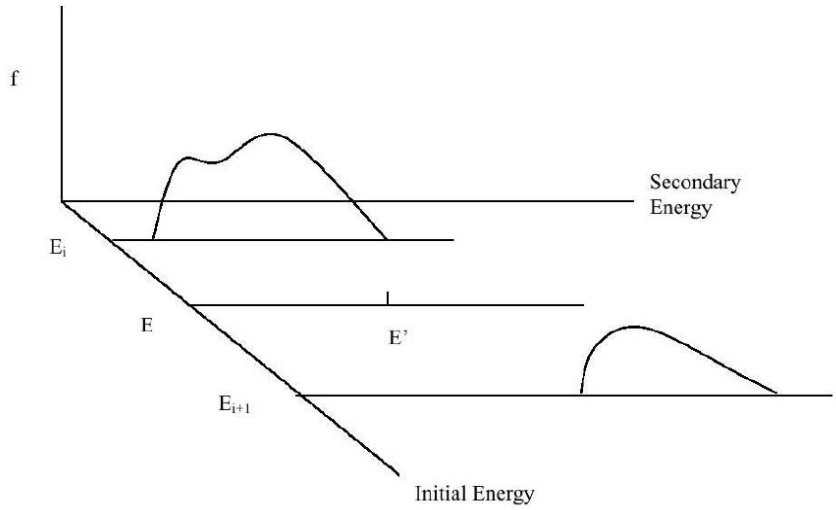

Figure 6.1: Interpolation between two-dimensional panels.

While the above equations are relatively simple, a lot of effort has to go into ensuring that the interpolation is done on the same E_{in} and μ grid. Much of the coding is involved in dealing with this "bookkeeping." Generally this is more difficult for the E probabilities, as for these the μ and E_{in} grids have to be the same. For these cases, the μ and E_{in} grids from the closest temperature is used as a reference, and a "dummy" panel is created at the desired angles and energies for the far temperature using (unit-base) linear interpolation. Equation 6.2 can then be used to calculate the probabilities at the intermediate temperature.

For the case where the cosine probabilities are equiprobable (generally the case for incoherent inelastic scattering), it is beneficial to do linear interpolation on the cosines themselves rather than on the cosine CDFs and PDFs. This is done by using linear interpolation in temperature,

$$\mu = \mu_i + \frac{T - T_i}{T_{i+1} - T_i} \left[\mu_{i+1} - \mu_i\right] . \tag{6.3}$$

6.1.1 Implementation into KENO

Implementing the two-dimensional Doppler broadening method into KENO is similar to the implementation of the one-dimensional problem-dependent Doppler broadening. A routine is added on to the cross-section processing chain shown in Figure 5.5 to handle the broadening of two-dimensional data. After the original data is read in, the interpolation discussed in Section 6.1 is performed. The new interpolated data then overwrites the old data, and KENO cross-section processing continues.

The original routines described in Sections 5.3.1 and 5.3.2 are slightly modified to contain a few additional variables that are needed to read in the two-dimensional data and to call the new broadening routines.

otf_broaden

This module is modified with the addition of a new subroutine (prebroaden_doublediff) that controls the overall flow of the two-dimensional Doppler broadening interpolation. It reads in the second bounding temperature containing the two-dimensional data, and creates the second cosine and energy panel used for interpolation. In SCALE kinematics data can be identified by either MT 1007 or MT 1008. MT 1007 holds data for incoherent inelastic scattering, and MT 1008 holds data for coherent or incoherent elastic scattering. This subroutine determines which scattering data is being processed, and which of the equations from Section 6.1 to apply for the cosine CDFs and PDFs.

For all scattering types, the CDFs and PDFs for the final energy are calculated the same way. First, dummy panels are created to ensure that each PDF or CDF is on the same cosine and incoming energy grid, then Equation 6.2 is applied to calculate the interpolated probability value. Once all probabilities have been interpolated, the original data is overwritten by the new interpolated data and processing continues.

otf_DD_utils

This module contains a variety of useful utility subroutines that are used in the interpolation of the double differential CDFs and PDFs. These include routines that:

- ensure the cosines and incident energies are on the same grid,
- create panels to hold interpolated data,
- calculate the unit-base normalization factors,
- recalculate CDFs and/or PDFs as needed, and
- overwrite the existing kinematics data with the interpolated data.

6.1.2 Results

In order to vary the Doppler broadening of the kinematic two-dimensional data a variety of moderators should be tested. Some moderators will only have incoherent inelastic scattering, but some moderators will also have either incoherent or coherent elastic scattering. The Doppler broadening routines need to be able to handle all such cases transparently and successfully.

Incoherent Inelastic Scattering

Incoherent inelastic scattering (stored exclusively in MT 1007) is present in all thermal moderators, and is arguably the most important scattering type present in the cross-section libraries. While any isotope would test this successfully, hydrogen in water was chosen as the main testing material. Hydrogen in water is the thermal moderator for the vast majority of operating nuclear reactors. As such, it is important to verify if the interpolation scheme is producing reasonable results.

To test this, the CASL pin cell described in Section 4.3.2 was slightly modified. Two main changes were made:

1. the thermal moderator was switched from H_2O to just hydrogen, and

2. the temperature of all non-moderator materials was fixed.

For SCALE, the default when using hydrogen is to use the thermal scattering data for hydrogen in water. If the user wants hydrogen free gas, they must explicitly state so. This occurs due to the prevalence of water as a moderator in the nuclear industry.

For hydrogen in water, data exists on the cross-section libraries at the temperatures 293 K, 350 K, 400 K, 450 K, 500 K, 550 K, 600 K, 650 K, and 800 K. Results from cases run at these moderator temperatures are shown in Figure 6.2a. Interpolation is controlled by the dbx parameter in KENO. By setting this to 2, two-dimensional interpolation is enabled. Cases run at temperatures in between the reference library temperatures are shown in Figure 6.2b.

As can be seen from Figure 6.2, results from the interpolated runs fall in the expected range of k-effective values. There is some error in between 650 K and 800 K, but this is expected due to the large difference in temperature between the two reference libraries.

To further examine the impact of the interpolation on incoherent inelastic scattering data, the hydrogen in the CASL pin cell model was changed back to H_2O. The results from this case are shown in Figure 6.3. It is important to recall that ^{16}O doesn't exist on the same temperature grid as hydrogen in water does, so the Doppler broadening approach discussed in Chapter 5 is used in addition to the two-dimensional interpolation.

Coherent Elastic Scattering

Coherent elastic scattering is present in many crystalline materials and is characterized by the presence of Bragg edges. Bragg edges result in a histogram style of PDFs (see Figure 6.4) where neutrons will scatter to discrete angles. Elastic scattering is stored in MT 1008, and this histogram nature is one easy way to test whether or not the scattering stored in MT 1008 is coherent or incoherent.

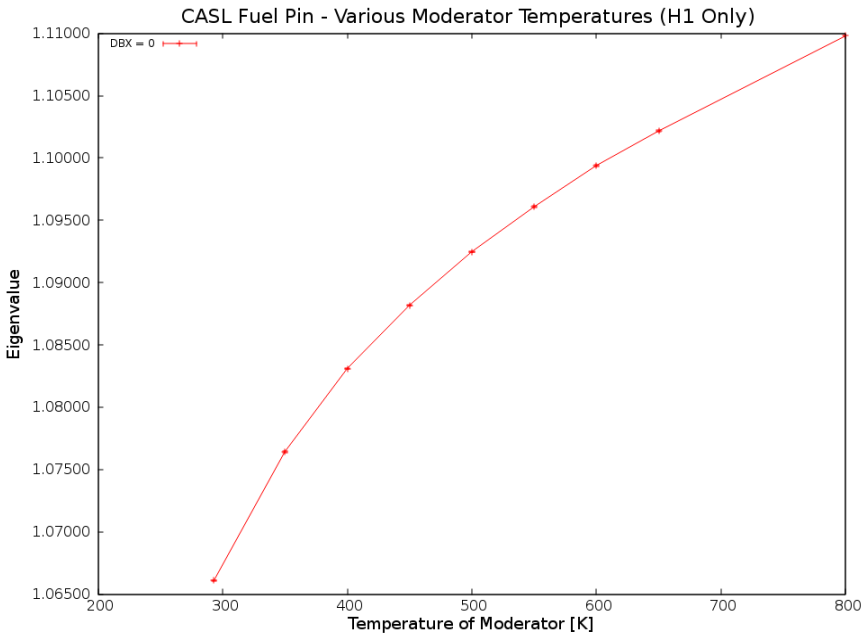

(a) DBX = 0

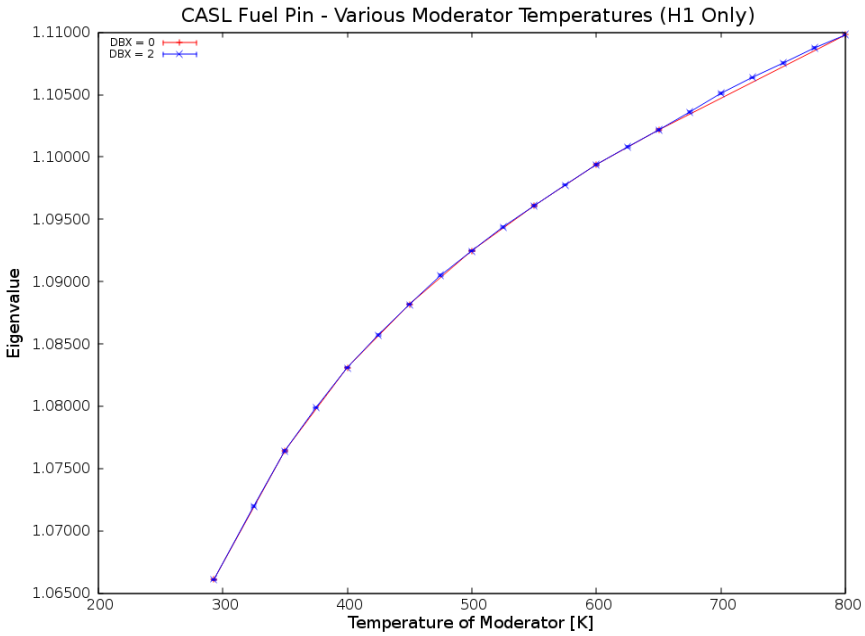

(b) DBX = 2

Figure 6.2: 2D interpolation results from CASL pin cell (hydrogen in water).

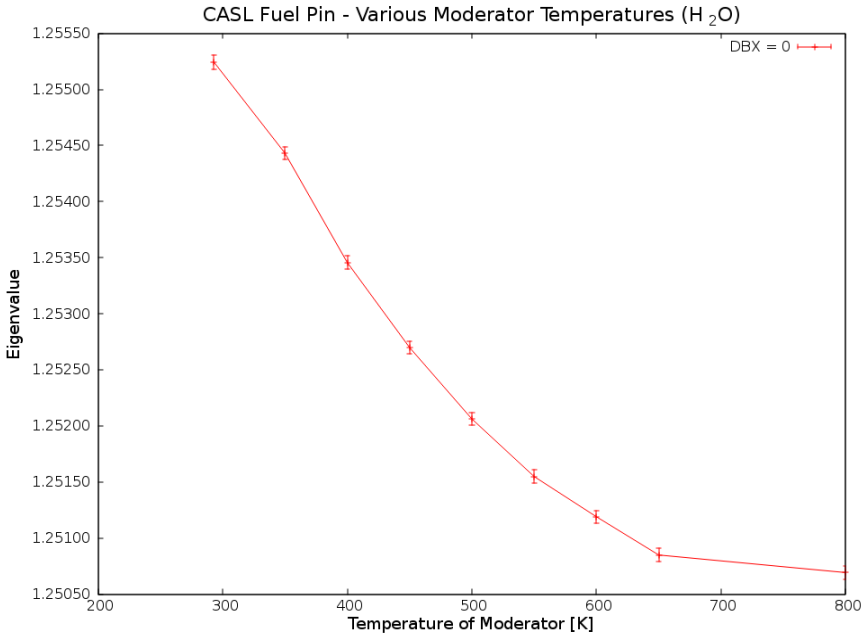

(a) DBX = 0

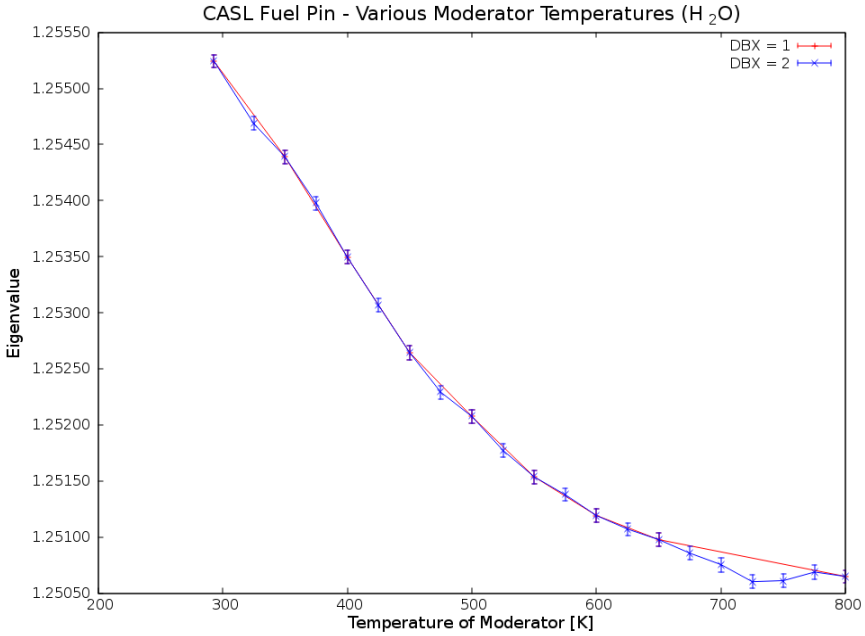

(b) DBX = 2

Figure 6.3: 2D interpolation results from CASL pin cell (water).

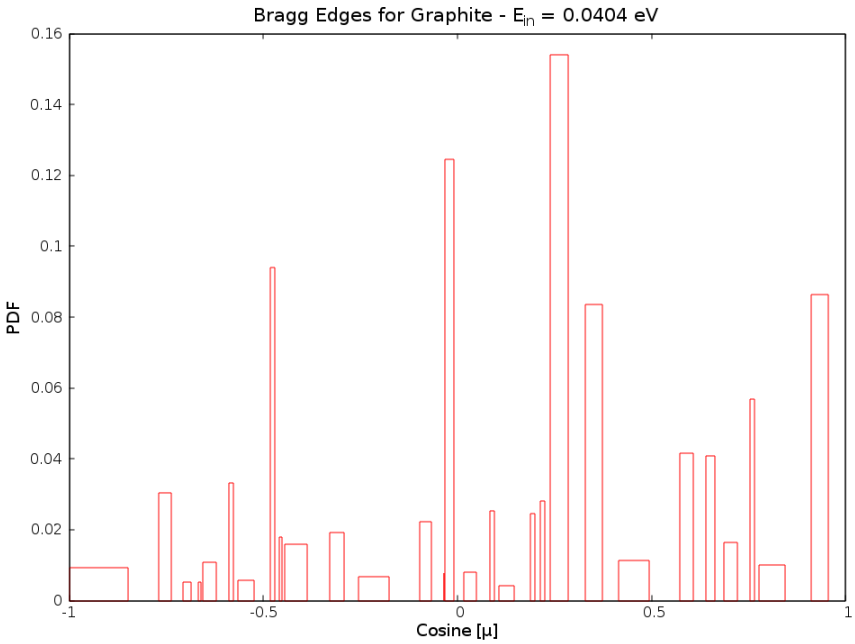

Figure 6.4: Bragg edges in graphite.

Interpolating the Bragg edge scattering data is relatively easy. If a specific scattering cosine exists at both temperatures, the new PDF can be interpolated between the two temperatures. If the specific scattering cosine only exists on one of the two temperatures, then the PDF is obtained by interpolating between the temperature where it exists and zero. In this way, the final results will contain the aggregate of the PDFs from both temperatures. The CDFs are then recalculated from the PDF data.

To test interpolation on this type of scattering, graphite is used as a moderator. Graphite is a thermal moderator sought for high temperature reactors. This case involves a sphere of uranium surrounded by a larger sphere of the graphite moderator. The fuel is slightly enriched uranium oxide (UO_2) at 900 K. The graphite temperature is varied to obtain the results. Results from the current reference temperatures are shown in Figure 6.5a and results using interpolation are shown in Figure 6.5b. The eigenvalues resulting from the interpolation runs are consistent with what is expected by interpolating the eigenvalues from the reference library runs.

Incoherent Elastic Scattering

Incoherent elastic scattering is stored much like incoherent inelastic scattering, except it is stored in MT 1008 and does not generally use equiprobable cosine bins. Therefore it can be treated much the same as inelastic scattering, except allowances have to be made to allow for cosines to exist on some temperatures and not others. An isotope will not have both incoherent and coherent elastic scattering, therefore MT 1008 can be used for both of them.

The test case used for incoherent elastic scattering is hydrogen in polyethylene. Like all thermal moderators it contains incoherent inelastic scattering in MT 1007; however it also contains incoherent elastic scattering in MT 1008. Unlike the other cases presented thus far, there are only two reference temperatures available for polyethylene: 293 K and 300 K. Results from the current reference temperatures are shown in Figure 6.6a and the results using interpolation are shown in Figure 6.6b.

Again, the eigenvalues resulting from these interpolation runs are consistent with what is expected by interpolating the eigenvalues from the reference library runs.

6.2 Interpolation Method on $S(\alpha, \beta)$ Data

As shown in Equation 2.25, only the $S(\alpha, \beta)$ value in the double differential equation depends on temperature. We can use this fact to interpolate only on the $S(\alpha, \beta)$ values, and then recalculate the double differential cross sections for a given material temperature. Unfortunately, calculating the double differential cross sections can take some time (on the order of 10 minutes per isotope per temperature), so this is an inefficient way to get problem-dependent, temperature-corrected, cross sections. However, it will serve as a good stepping block to the use of $S(\alpha, \beta)$ values directly as discussed in Chapter 7.

6.2.1 Implementation into KENO

The double differential cross sections are calculated by the AMPX module Y12. Y12 takes the thermal scattering data as formatted by ENDF and outputs it in such a way that it can be used by KENO as described in Section 2.8.3. To interpolate the $S(\alpha, \beta)$ data and create double differential cross sections "on-the-fly," KENO will have to provide the needed data to Y12 and read in the Y12 results back into the KENO data structures. This is done by providing the required ENDF-formatted data file, calling Y12 from within KENO, and reading the created data file.

This implementation is easily done in KENO by adding one routine that reads in the required data from the ENDF-formatted file, calls Y12, and then reads the Y12 output into the required KENO cross-section arrays. Due to the fact that Y12 is implemented as a library, execution control does not need to leave KENO. Unfortunately, as mentioned earlier, compared to quickly interpolating the double differential cross sections, this method can take several minutes per moderator used.

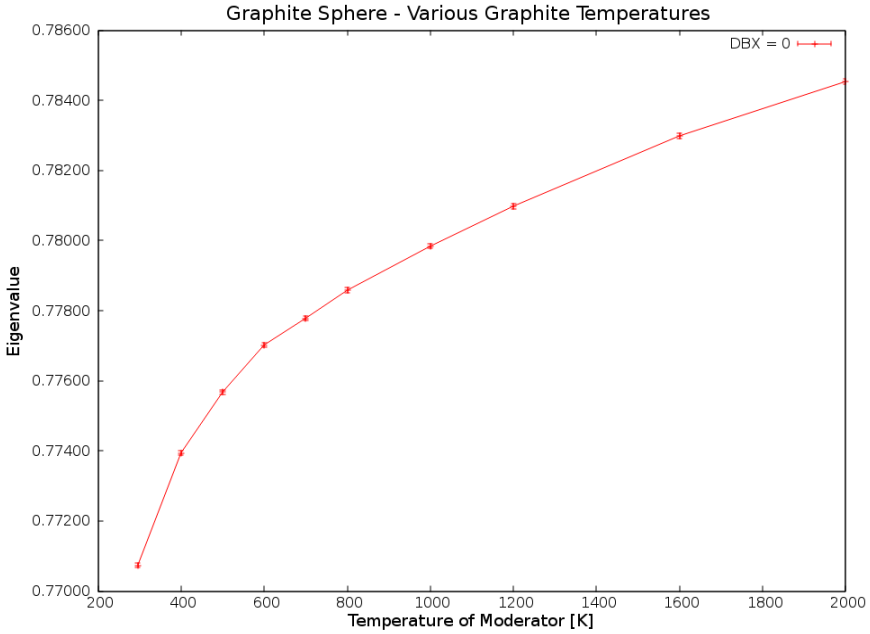

(a) DBX = 0

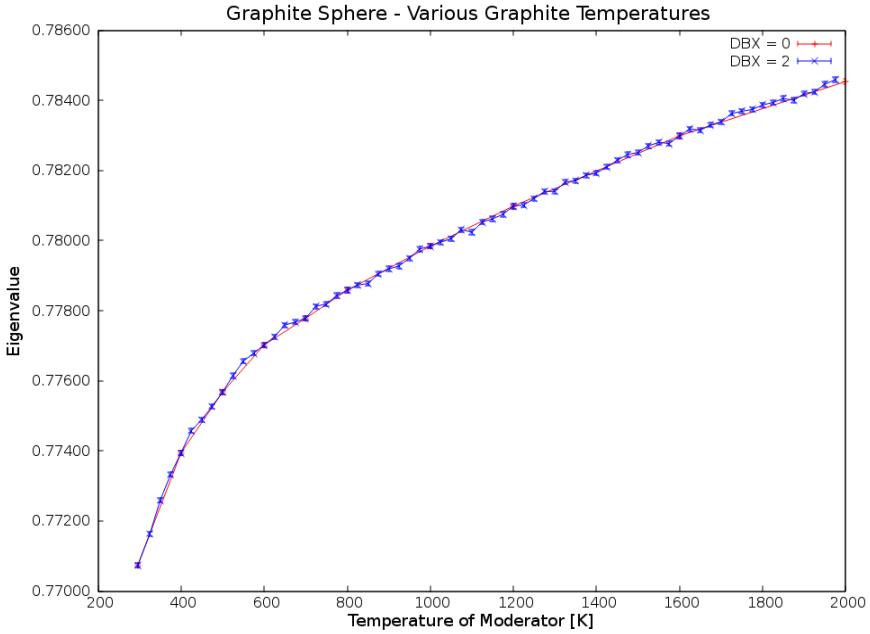

(b) DBX = 2

Figure 6.5: 2D interpolation results from graphite sphere.

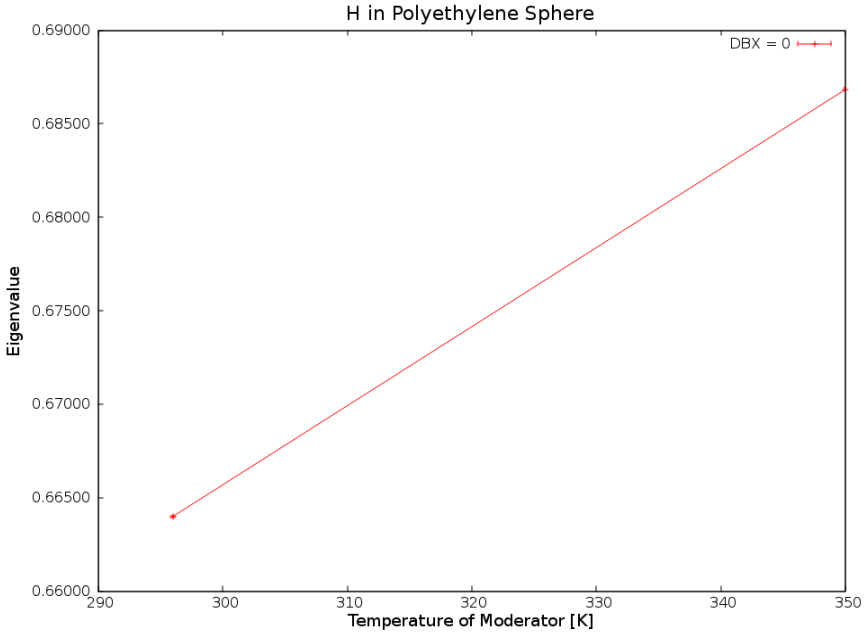

(a) DBX = 0

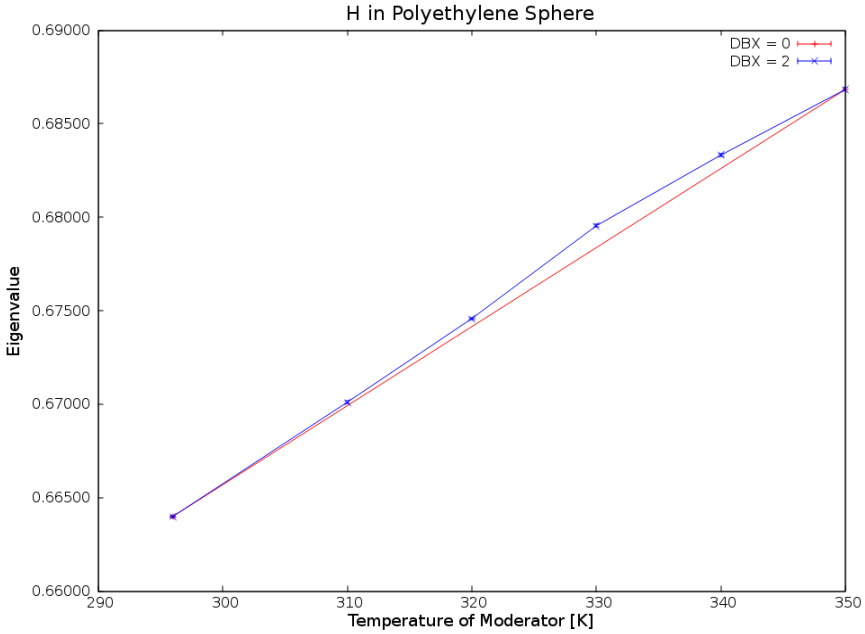

(b) DBX = 2

Figure 6.6: 2D interpolation results from polyethylene sphere.

In order to make this method work, KENO would also have to depend on the AMPX code. These reasons make it unfeasible to ship a production KENO code with this method enabled, but it can still be tested here for thoroughness.

6.2.2 Results

The CASL fuel pin surrounded by hydrogen in water and the graphite sphere will be used to demonstrate the effectiveness of interpolation on the $S(\alpha, \beta)$ tables. Note that interpolating on the $S(\alpha, \beta)$ data will only affect the incoherent inelastic scattering cross sections. The other types of scattering (stored in MT 1008 for KENO) will not be affected by this interpolation and must be handled by interpolating on the double differential cross sections as described previously.

To enable this testing feature, the dbx parameter is set to 3. Results comparing the double differential interpolation with the $S(\alpha, \beta)$ interpolation for the CASL pin cell surrounded by hydrogen in water are shown in Figure 6.7. As can be seen in the figure, the results are very similar to that of interpolation on the double differential cross sections. This is largely unexpected. By using Y12 to calculate the double differential cross sections, we can remove the slight bump that occurs at the temperature where the original method changed energy grids. This is particularly evident in Figure 6.7 at the 325 K temperature; the data is much smoother when using the values calculated by interpolating the $S(\alpha, \beta)$ data.

Results obtained by modeling the spherical fuel region surrounded by a graphite sphere are shown in Figure 6.8. Interpolation on the double differential cross sections yields similar results to interpolation on the $S(\alpha, \beta)$ tables.

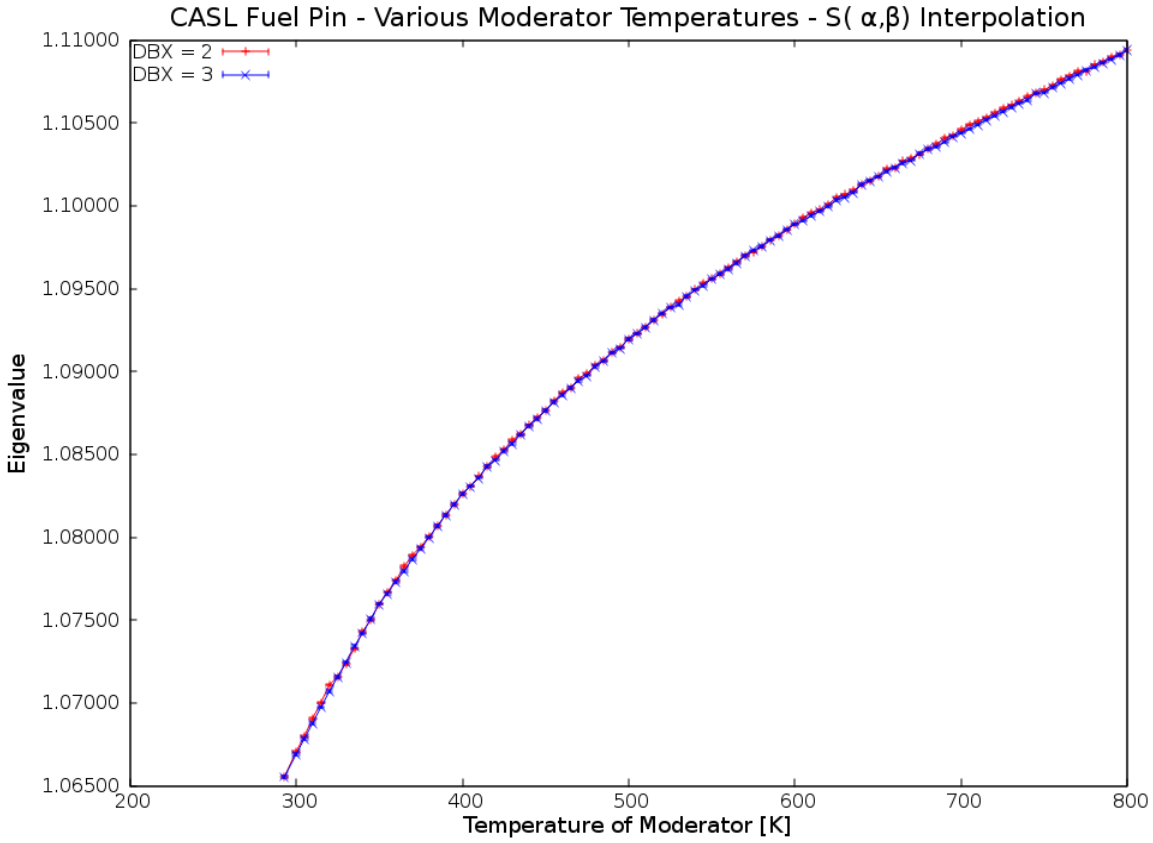

Figure 6.7: 2D interpolation results on $S(\alpha, \beta)$ for CASL pin cell.

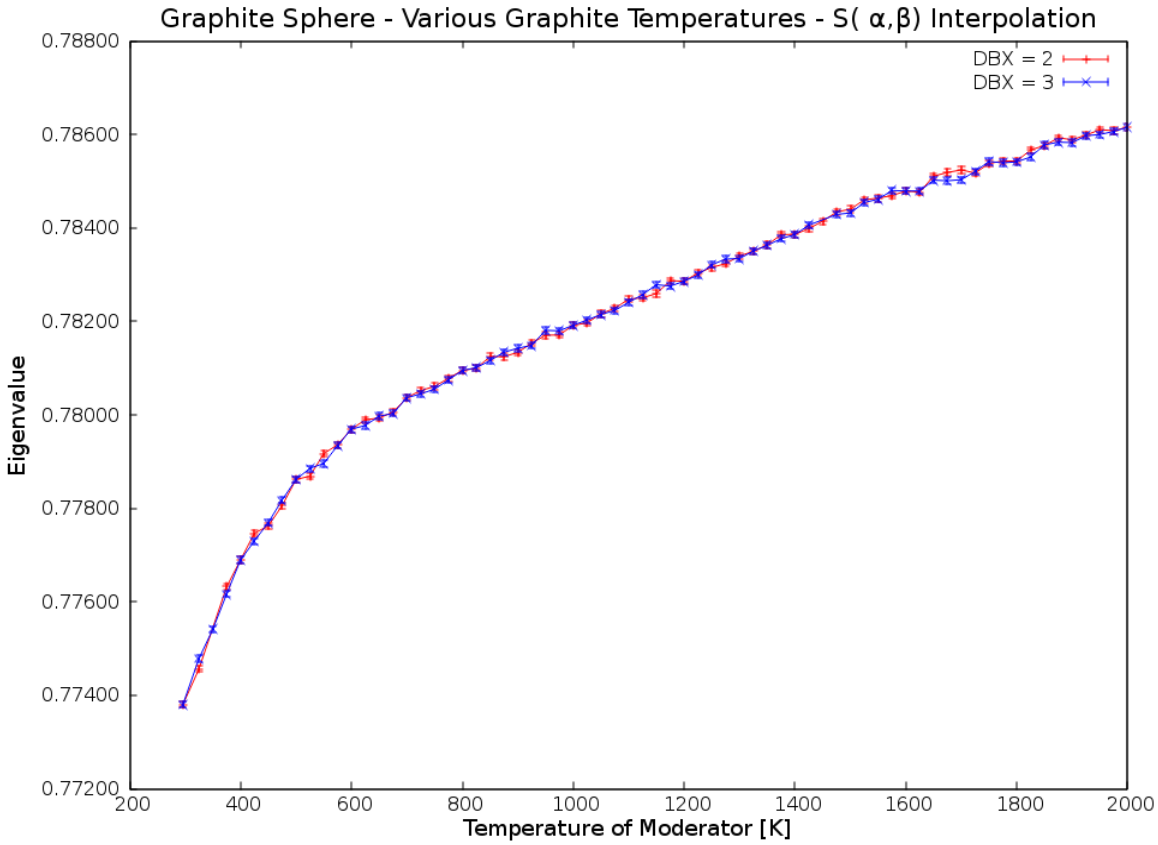

Figure 6.8: 2D interpolation results on $S(\alpha, \beta)$ for graphite sphere.

Chapter 7

Direct $S(\alpha, \beta)$ Scattering Implementation

As discussed in previous chapters, KENO currently uses probabilities from the double differential form of the scattering cross sections. This is a well tested and proven method for modeling scattering off of thermal moderators [32]. For incoherent inelastic scattering the double differential cross section only depends on $S(\alpha, \beta)$ values that are calculated and tabulated in ENDF files. Therefore it is possible to use the $S(\alpha, \beta)$ values directly in the Monte Carlo transport calculation by calculating the $S(\alpha, \beta)$ CDFs and utilizing them when a scattering event occurs.

This chapter discusses the methodology of using and creating $S(\alpha, \beta)$ CDFs for use in a direct $S(\alpha, \beta)$ method. It involves creating a new AMPX module for creating the $S(\alpha, \beta)$ CDFs from the ENDF files, and modifying KENO to use these CDFs instead of the original double differential CDFs and PDFs.

7.1 Direct $S(\alpha, \beta)$ Method

Scattering law data is stored in ENDF files as a set of function values, S, over a grid of discrete α and β values. By storing the scattering data in this way, the storage

requirement is minimized. Unfortunately, the data generally has to be processed and put into another form that is useful for computational methods before it can be used. As an example, the AMPX module Y12 takes the $S(\alpha,\beta)$ values and calculates the double differential cross section, $\sigma(\mu, E \rightarrow E')$, from them. Bischoff first suggested the direct $S(\alpha,\beta)$ method by exploiting the compact format of the $S(\alpha,\beta)$ data through generating PDFs in both α and β to drastically lower the storage cost. [39]

In order to use the $S(\alpha,\beta)$ data, two dimensionless quantities need to be defined. The dimensionless momentum transfer, α, is defined by

$$\alpha = \frac{E + E' - 2\mu\sqrt{E'E}}{AkT}, \tag{7.1}$$

where,

E	=	incident neutron energy (eV),
E'	=	scattered neutron energy (eV),
μ	=	cosine of the scattering angle,
A	=	atomic mass,
kT	=	temperature (eV),

and the dimensionless energy transfer, β, is defined by

$$\beta = \frac{E - E'}{kT}, \tag{7.2}$$

where positive values represent downscattering events. Using these definitions for α and β the double differential cross section is defined as

$$\sigma(E \rightarrow E', \mu) = \frac{\sigma_b}{2kT}\sqrt{\frac{E'}{E}}e^{\beta/2}S(\alpha,\beta) \tag{7.3}$$

where σ_b is the bound cross section unique to each element. The difference between this equation and Equation 2.23 lies in the definition of β given in Equation 7.2.

Ballinger [30] noticed that a transformation matrix could be obtained given the definitions of α and β in terms of energy and angle where

$$\begin{bmatrix} \frac{d\alpha}{dE} & \frac{d\alpha}{d\mu} \\ \frac{d\beta}{dE} & \frac{d\beta}{d\mu} \end{bmatrix} = \begin{bmatrix} \frac{1-\mu\sqrt{\frac{E'}{E}}}{AkT} & \frac{-2\sqrt{E'E}}{AkT} \\ \frac{1}{kT} & 0 \end{bmatrix} . \tag{7.4}$$

Rewriting the double differential cross section in terms of α and β using the determinant of the transformation matrix yields

$$\sigma(\alpha,\beta) = \frac{\sigma_b AkT}{4E} S(\alpha,\beta) e^{\beta/2} . \tag{7.5}$$

By noticing that the leading term is a constant, this double differential cross section can be integrated over all α and β values to obtain a scattering cross section as a function of energy.

There is no efficient way to directly sample α and β from Equation 7.5. Therefore, as described in Section 2.7.1, CDFs and PDFs are generally constructed. These are then sampled to determine the scattered neutron energy by first sampling a β followed by sampling an α. Integration over both α and β is required to convert the scattering law data into a set of CDFs. By doing this, the CDF for α can be decoupled from the incident energy which will reduce the storage requirement for the data.

The two associated CDFs are

$$P(\beta_i|E,T) = \int_0^{\beta_i} Ce^{\beta/2} \int_{\alpha_{min}}^{\alpha^{max}} S(\alpha,\beta,T)\mathrm{d}\alpha\mathrm{d}\beta , \tag{7.6}$$

where C is a constant and thus doesn't matter to the calculation of the CDF, and

$$P(\alpha_i|\beta,E,T) = \int_0^{\alpha_i} \frac{S(\alpha',\beta,T)}{\int_{\alpha_{min}}^{\alpha^{max}} S(\alpha,\beta,T)\mathrm{d}\alpha}\mathrm{d}\alpha' . \tag{7.7}$$

As mentioned previously, the α CDF can be decoupled from the incident energy by storing "F Factors" defined as

$$F(\alpha_i, \beta_j) = \int_0^{\alpha_i} S(\alpha', \beta_j) e^{\beta_j/2} d\alpha' \tag{7.8}$$

and calculating the α CDFs on-the-fly from

$$P(\alpha|\beta_j) = \frac{F(\alpha, \beta_j) - F(\alpha_{\min}, \beta_j)}{F(\alpha_{\max}, \beta_j) - F(\alpha_{\min}, \beta_j)} \,. \tag{7.9}$$

Constructing the α CDFs on-the-fly is the key for making the direct $S(\alpha, \beta)$ method memory conservative.

In order to calculate α_{min} and α_{max} one uses the knowledge that the minimum momentum transfer occurs during a glancing collision (or $\mu = 1$). Therefore using Equation 7.1 α_{min} is

$$\alpha_{min} = \frac{2E - \beta kT - 2\sqrt{E^2 - E\beta kT}}{AkT} \tag{7.10}$$

and α_{max} ($\mu = -1$) is

$$\alpha_{max} = \frac{2E - \beta kT + 2\sqrt{E^2 - E\beta kT}}{AkT} \,. \tag{7.11}$$

Once the α and β CDFs are constructed, it is straightforward to sample a β from the distribution and use it to calculate an α value. First a β is sampled from the β distribution and used, along with the incident energy, to sample an α from the constructed α distribution described in Equation 7.9. The sampled α and β values are then converted into scattering cosine and exit energy using the definitions given in Equations 7.1 and 7.2.

β CDFs are stored on an incident energy mesh that is calculated by Y12 and the α "F Factors" are stored on the resulting β mesh. Since the α "F Factors" don't also

need to be stored on an incident energy mesh, the memory taken up by the CDFs can be greatly reduced. However, since α CDFs then need to be calculated during neutron transport, the time taken to sample a neutron scattering event increases when using the direct $S(\alpha, \beta)$ method.

7.1.1 Interpolation on $S(\alpha, \beta)$ CDFs

Interpolation is done on the $S(\alpha, \beta)$ data in the same way that interpolation was done on the double differential CDFs (see Section 6.1). The same unit-base interpolation functions are used to interpolate the β values and the α values are done using normal interpolation. Interpolation is linear-logarithmic done in the square root of temperature. Like the interpolation done for the double differential CDFs, the β grid of the closest temperature is used. This could lead to a slight shift in the results as the grid changes at the mid-point between temperatures.

7.2 Implementation

There are two distinct areas that need to be addressed to implement the direct $S(\alpha, \beta)$ method in SCALE:

1. need to create an AMPX module that will generate the α and β CDFs, and
2. need to implement in KENO the ability to read the α and β CDFs and use them for calculating the exit energy and angle of a scattering event.

7.2.1 Creation of α and β CDFs

In order to create the α and β CDFs a new AMPX module needed to be created. This module will implement the methods described in Section 7.1 to create a binary file that is read in by KENO. This module will be heavily based on the existing AMPX module called Y12, which reads in the ENDF data file and prepares double differential

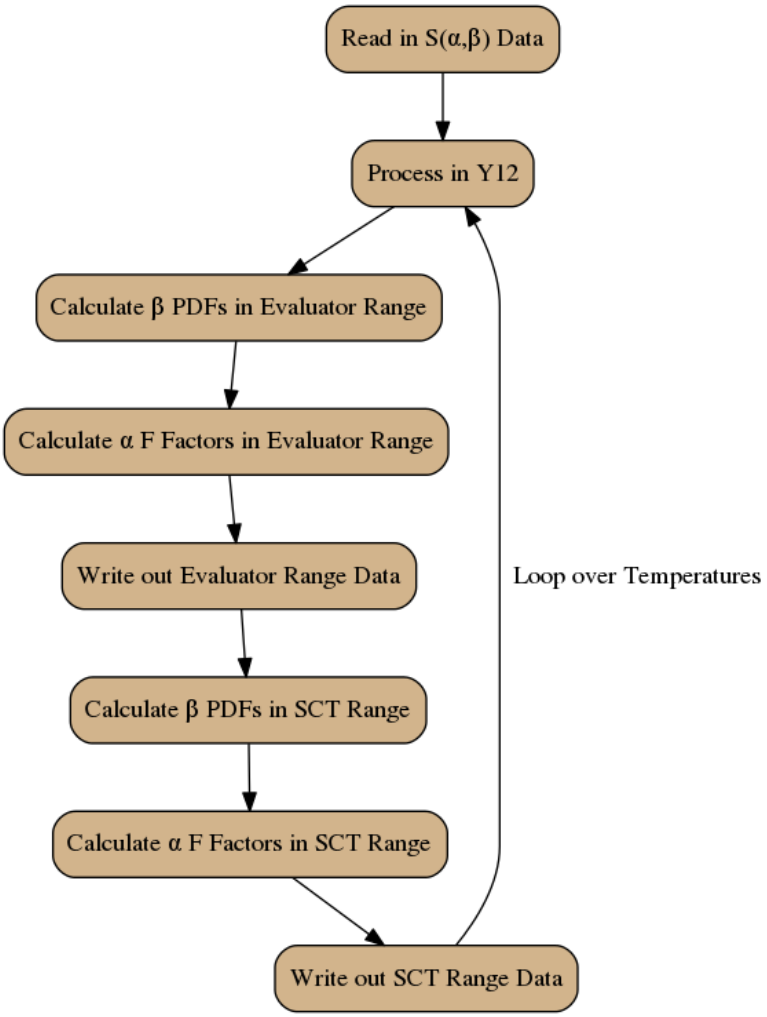

Figure 7.1: Program flow of S$\alpha\beta$RE.

cross sections. In the future it is possible that this new module, named S$\alpha\beta$RE (for $S(\alpha, \beta)$ Reformat Engine) can be pulled into Y12 and no longer exist as a separate program.

The program flow of S$\alpha\beta$RE is shown in Figure 7.1. As shown in the figure, there are two distinct areas of S$\alpha\beta$RE. First, the data for the evaluator range is processed, and then the data in the Short Collision Time (SCT) approximation region is calculated and processed. Calling Y12 is done by S$\alpha\beta$RE to generate the incident

and final energy grids to be used by the β CDFs. The α grid used is that created by the evaluator on the ENDF file.

Generally when evaluations are done and placed into ENDF files, the evaluator assigns some maximum energy that the $S(\alpha, \beta)$ values should be used for. This maximum energy typically is anywhere from 2 to 4 eV. Above that range the SCT approximation is used. The SCT approximation [40] is an equation that is used to directly obtain a $S(\alpha, \beta)$ value using

$$S^{\mathrm{SCT}}(\alpha, \beta, T) = \frac{\exp\left[-\frac{(\alpha-|\beta|)^2 T}{4\alpha T_{\mathrm{eff}}(T)} - \frac{|\beta|}{2}\right]}{\sqrt{4\pi\alpha \frac{T_{\mathrm{eff}}(T)}{T}}}, \tag{7.12}$$

where T_{eff} is the effective temperature and is obtained from the ENDF file. Once the $S(\alpha, \beta)$ values are obtained, the calculation of the CDFs proceeds as before. The structure of the binary file produced by S$\alpha\beta$RE is documented in Appendix A.

Currently the β grid created depends on the final energy grid obtained from Y12. That is, for a specific incident energy, a β point is created for every calculated exit energy. This leads to a final exit energy grid that has the same density as that produced by Y12 and currently used in KENO for the double differential cross-section scattering. This grid is fairly inefficient, and there is potential for thinning the grid by removing points that can be recalculated through linear interpolation (within some error tolerance). The α grid is the same as that created by the evaluator in the ENDF file. No work has been done to expand or thin this grid. The total size of the $S(\alpha, \beta)$ binary data file is generally about one-quarter the size of a similar double differential CDF data file.

7.2.2 Implementation into KENO

Implementing the direct $S(\alpha, \beta)$ method into KENO is relatively straightforward. When a collision occurs, KENO determines the type of reaction that is going to occur by using the one-dimensional cross sections. Currently, if the reaction is going to

be an incoherent inelastic scatter, KENO will sample the double differential CDFs by sampling a cosine followed by an exit energy. The properties of the neutron are adjusted, and the history continues. With the direct $S(\alpha, \beta)$ method, two new subroutines were created to sample α and β, named sample_alpha and sample_beta, respectively. For temperature interpolation, the module otf_broaden was expanded to include a subroutine to interpolate on the $S(\alpha, \beta)$ CDFs, and a new module was created to aid in the interpolation named otf_sab_utils.

sample_beta

Sampling of β was done first so that the calculated β could be used to determine $\alpha_{\min}$ and $\alpha_{\max}$ for the α "on-the-fly" sampling. Sampling the β is done in a similar fashion as sampling the exit energy for the double differential cross section method. If the incoming energy matches an energy on the energy grid exactly, then a random number is sampled and the β is calculated from the CDFs for that energy. If the incoming energy is between two energy points on the incident energy grid, then one random number is sampled and used to generate two β values using the bounding incident energies. The final beta is then determined by linear interpolation on the incoming energy.

After β is determined, the exit energy can be determined by using Equation 7.2 in the form

$$E' = E - \beta kT \,. \tag{7.13}$$

sample_alpha

Determining α (and therefore μ, the scattering cosine) is slightly more involved than calculating β. The steps to sample α are:

1. sample a random number,

2. interpolate between the β values to obtain a F Factor grid for all α values,

3. calculate $\alpha_{\min}$ and $\alpha_{\max}$ using Equations 7.10 and 7.11,

4. calculate the CDFs using Equation 7.9 (can stop calculating this when the CDF exceeds the random number), and

5. determine α from the random number and CDFs.

Once α is determined, μ can be determined by using Equation 7.1 in the form

$$\mu = \frac{E + E' - \alpha AkT}{2\sqrt{EE'}} \,. \tag{7.14}$$

otf_broaden and otf_sab_utils

A new subroutine named otf_prebroaden_SAB was created that controls the logic for prebroadening the $S(\alpha, \beta)$ CDFs. First, the α F Factors are interpolated in temperature across their β grid. There is no need for unit base interpolation here due to the fact that the CDFs are calculated as needed when given β. Next, the β values are interpolated by looping over all incoming energies, creating β CDFs at that energy if they don't exist, and interpolating to the desired temperature.

Like the double differential interpolation discussed in Section 6.1.1, it is necessary to use a unit-base interpolation scheme when interpolating β values on temperature. The logic to do this unit-base interpolation is contained in the otf_sab_utils module. This module contains everything required to do the unit-base conversion and do the final interpolation on temperature. After a new β CDF panel is created, it can be used it overwrite the existing data so that the data is now temperature corrected.

7.3 Results

Two types of results will be shown in this section. First, the direct $S(\alpha, \beta)$ method will be shown to produce similar scatters when compared to the current KENO method of scattering. Next, some of the simple models used to test the interpolation on the double differential cross sections (see Section 6.2.2) will be run and the results shown.

7.3.1 Scattering Results

As a test to verify the accuracy of the direct $S(\alpha, \beta)$ method, a variety of scatters off various moderators were done, and the results tallied into exit energy and cosine bins. For each test, several million scattering events were tallied. After each scatter the neutron was reset to some initial energy so that a distribution of exit energies and cosines could be obtained.

Figure 7.2 shows the results of scattering 10 million neutrons off of hydrogen in water, using both the double differential scattering cross sections and the direct $S(\alpha, \beta)$ method. As can be seen in Figure 7.2a, the exit energy distribution from the direct $S(\alpha, \beta)$ method almost overlays the distribution obtained using the current double differential cross section approach. There is a bit more structure to the direct $S(\alpha, \beta)$ results, as evidenced by the dips and rises around 0.8 eV and 0.9 eV. For the scattering angle results in Figure 7.2b, the double differential results are hampered by the hard-coded 32 equiprobable bin limit. You can clearly see 32 distinct steps where the probability is the same. Due to the OTF method used for sampling the α value, the scattering angle distribution is a smooth curve.

The main drawback of using the direct $S(\alpha, \beta)$ method is that, due to constructing the α CDFs during the collision, each collision takes two to three times longer to sample. While not noticeable for a single collision, running these scattering tests with millions of neutrons leads to the run time increasing from tens of seconds to a minute or more.

More examples of scattering off of hydrogen in water are shown in Figures 7.3 and 7.4. Figure 7.4 is particularly interesting due to the fact that $S(\alpha, \beta)$ values here are calculated using the SCT approximation. With the SCT approximation, most structure in the PDFs disappear. This leads to a relatively flat probability distribution instead of the structure seen in the evaluation range. This is particularly noticeable when the incoming energy is near the exit energy. In the evaluation range there is a clear peak where $E = E'$ whereas in the SCT range this peak is gone.

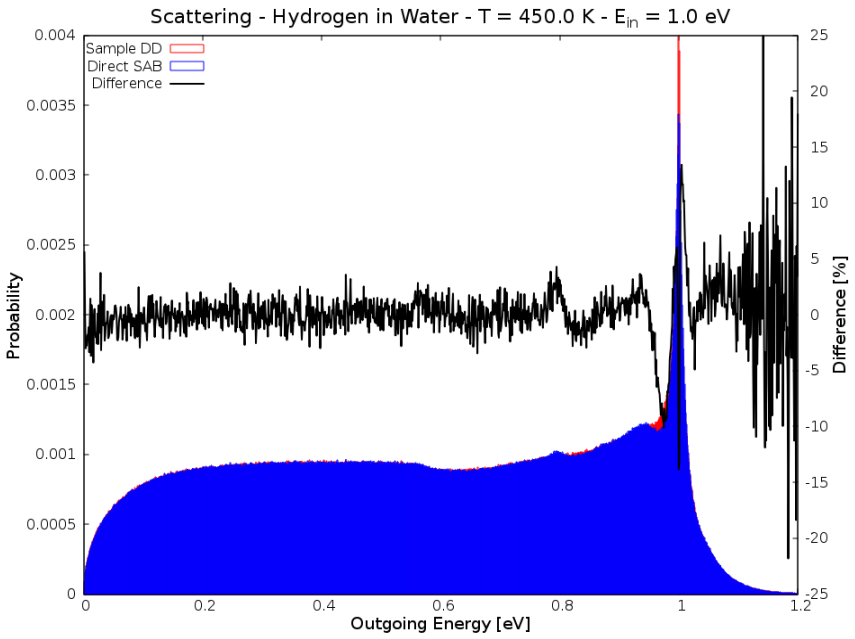

(a) Exit energy

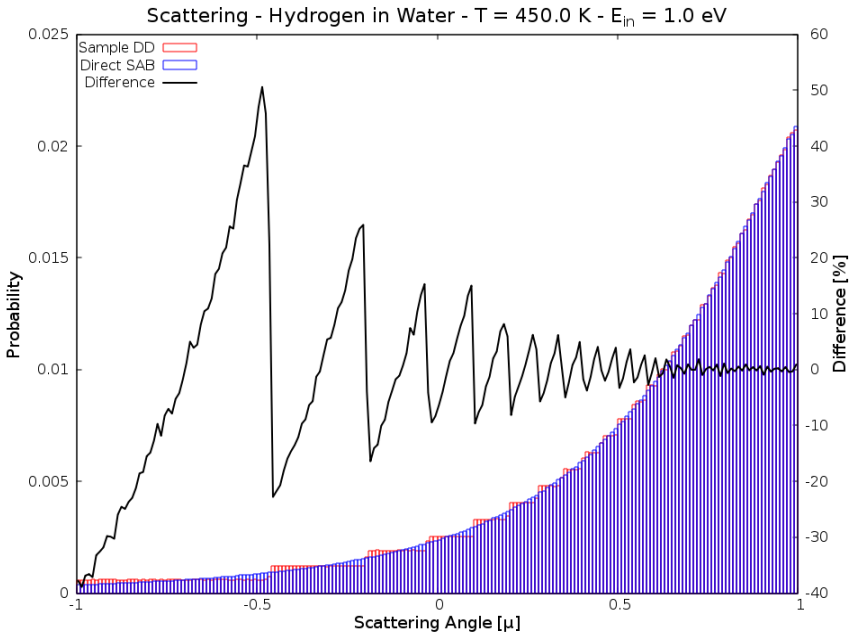

(b) μ

Figure 7.2: Neutron scattering off of hydrogen in water at $E_{\text{in}} = 1$ eV, $T = 450$ K.

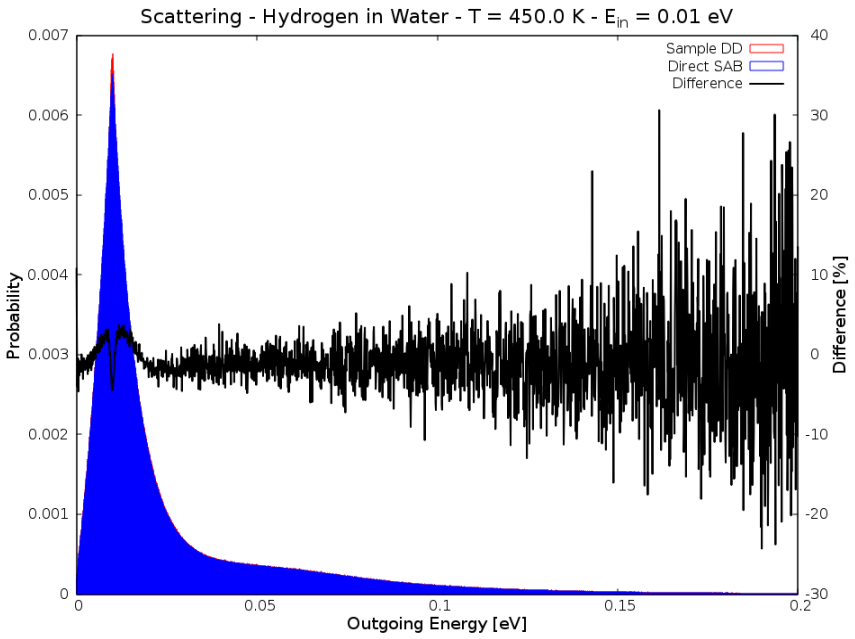

(a) Exit energy

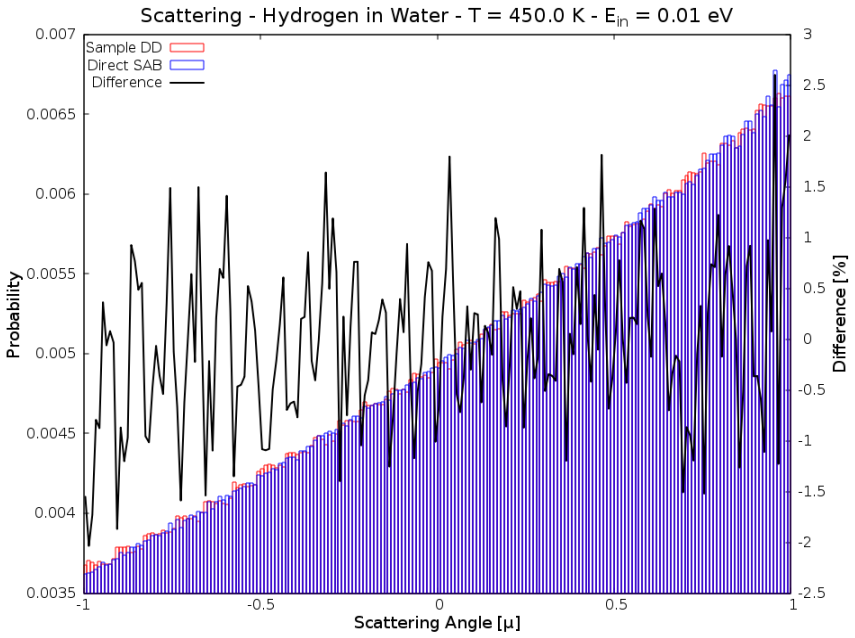

(b) μ

Figure 7.3: Neutron scattering off of hydrogen in water at $E_{\text{in}} = 0.01$ eV, $T = 450$ K.

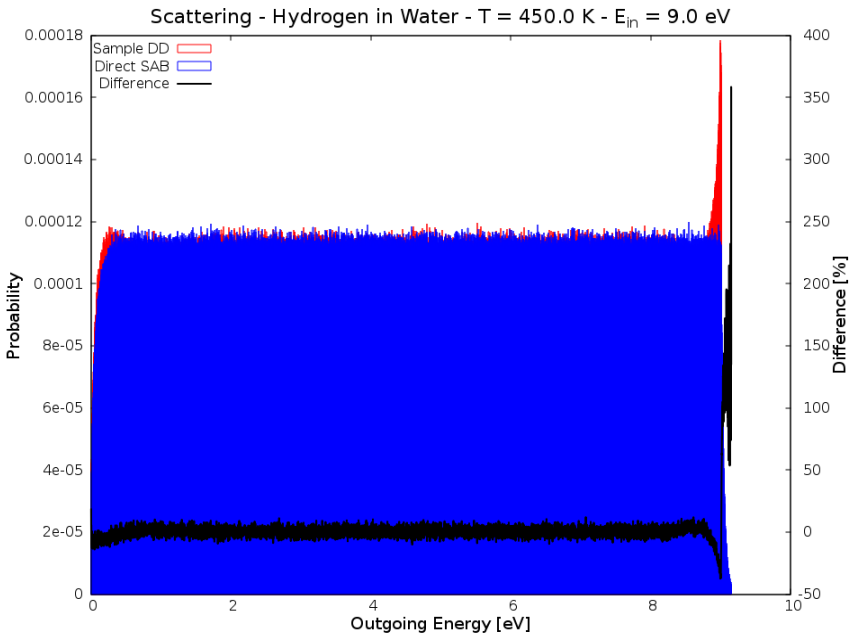

(a) Exit energy

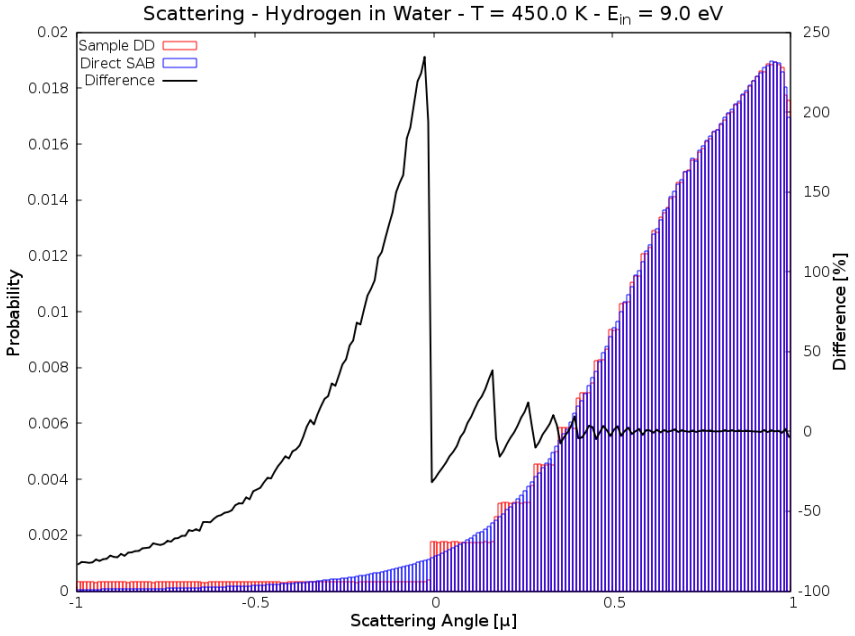

(b) μ

Figure 7.4: Neutron scattering off of hydrogen in water at $E_{\text{in}} = 9$ eV, $T = 450$ K.

There is, however, still a small peak when using the double differential cross sections. This peak is not physical and is believed to come from corrections done by AMPX to account for long tails in the CDF distribution. Regardless, as shown in the eigenvalue results, this peak has little effect on the eigenvalue.

Another example of a prominent thermal scattering material is graphite. Results showing graphite scatters are in Figures 7.5 to 7.7. Again the structure of the $S(\alpha, \beta)$ values can be see inside the evaluation range (which is up to 2 eV for graphite). Above 2 eV, in the SCT range, there is again no structure and a small peak in the double differential CDFs calculated by AMPX.

7.3.2 KENO Results

To demonstrate the accuracy of the direct $S(\alpha, \beta)$ method on eigenvalue calculations, the same suite of models that were run in Section 6.1.2 will be run with direct $S(\alpha, \beta)$ enabled. Like before, the cases will be run with temperature interpolation turned on when the temperature needs to be interpolated. The method for temperature interpolation on the $S(\alpha, \beta)$ CDFs is discussed in Section 7.1.1.

Remember that the direct $S(\alpha, \beta)$ method is only used for incoherent inelastic scattering. For the other types of thermal scattering, the interpolation methods on the double differential cross section CDFs will be used. Since the method is so similar, only two cases will be showcased: The CASL pin cell surrounded by water, and the uranium/graphite sphere.

CASL Pin Cell

Figure 7.8a shows the results of using the direct $S(\alpha, \beta)$ method at the library temperatures (no interpolation). One-dimensional Doppler broadening (dbx = 1) still needs to be used because the moderator contains ^{16}O that needs to be Doppler broadened to the correct temperature. Figure 7.8b shows the results when intermediate temperatures are added and interpolation is performed on the $S(\alpha, \beta)$

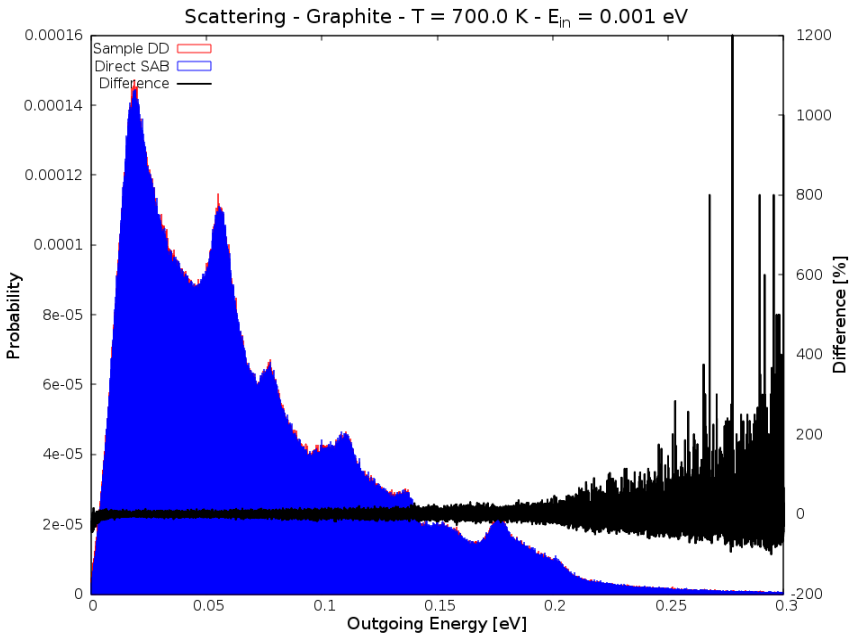

(a) Exit energy

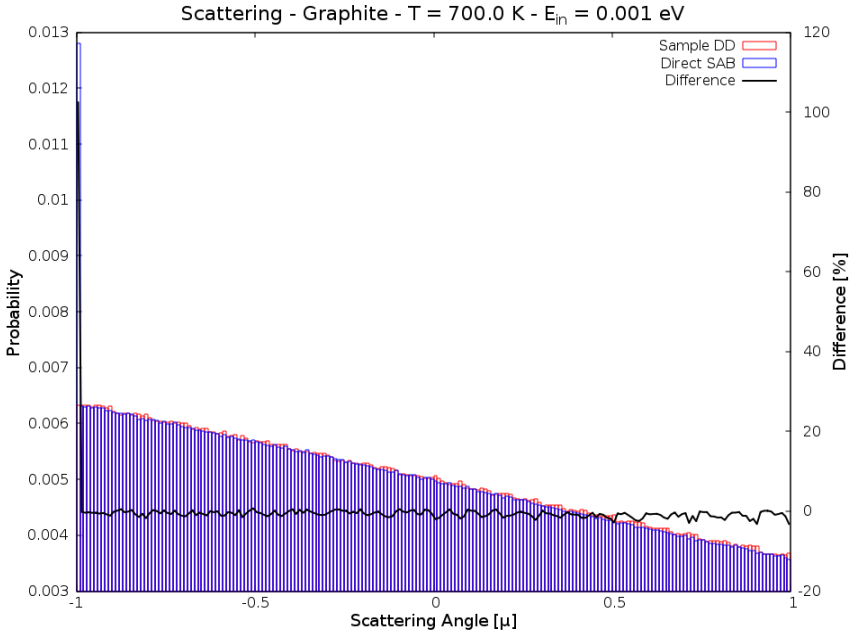

(b) μ

Figure 7.5: Neutron scattering off of graphite at $E_{\text{in}} = 0.001$ eV, $T = 700$ K.

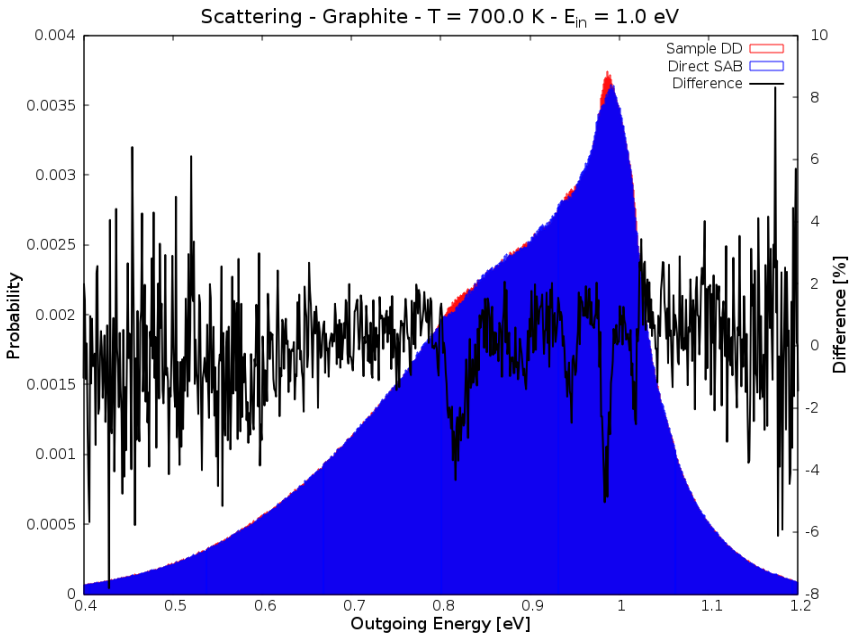

(a) Exit energy

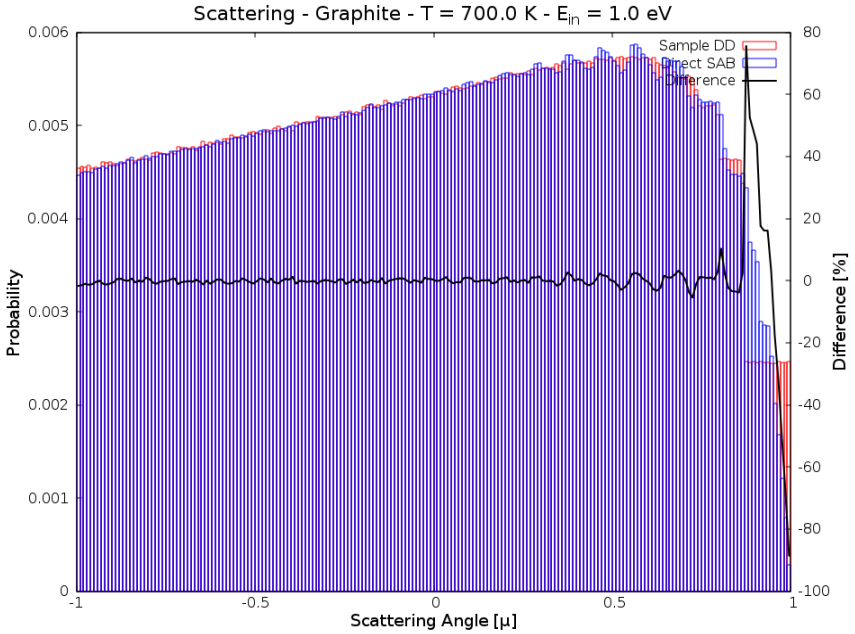

(b) μ

Figure 7.6: Neutron scattering off of graphite at $E_{\text{in}} = 1$ eV, $T = 700$ K.

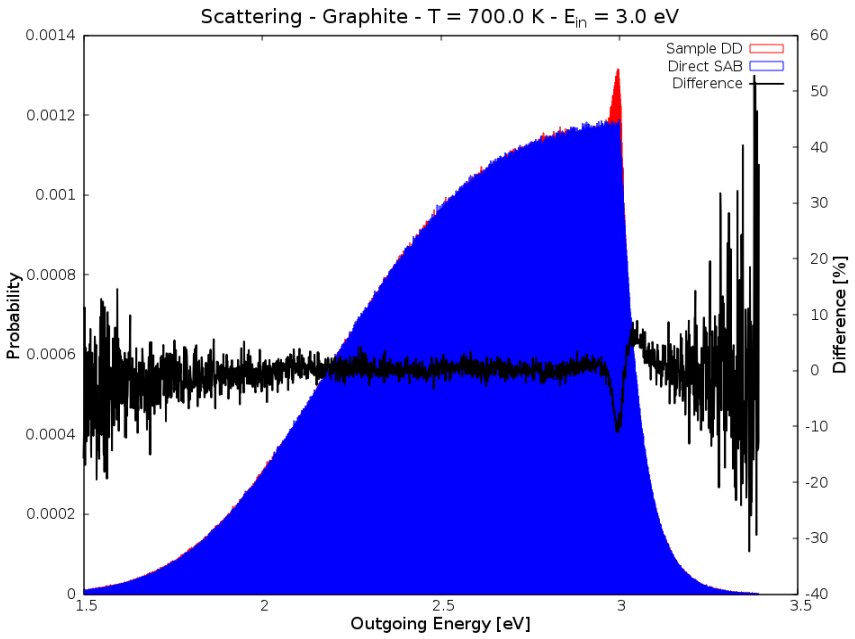

(a) Exit energy

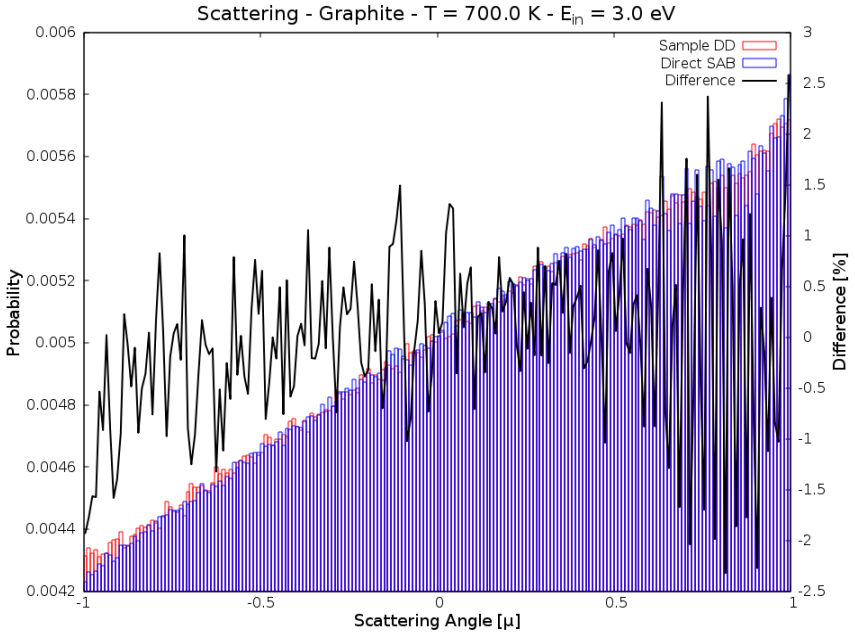

(b) μ

Figure 7.7: Neutron scattering off of graphite at $E_{\text{in}} = 3$ eV, $T = 700$ K.

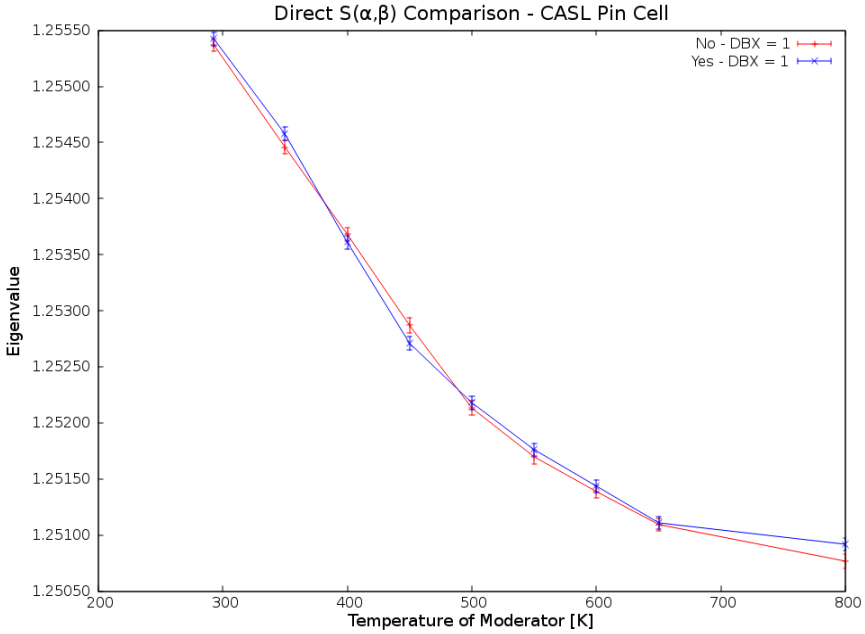

(a) DBX = 1

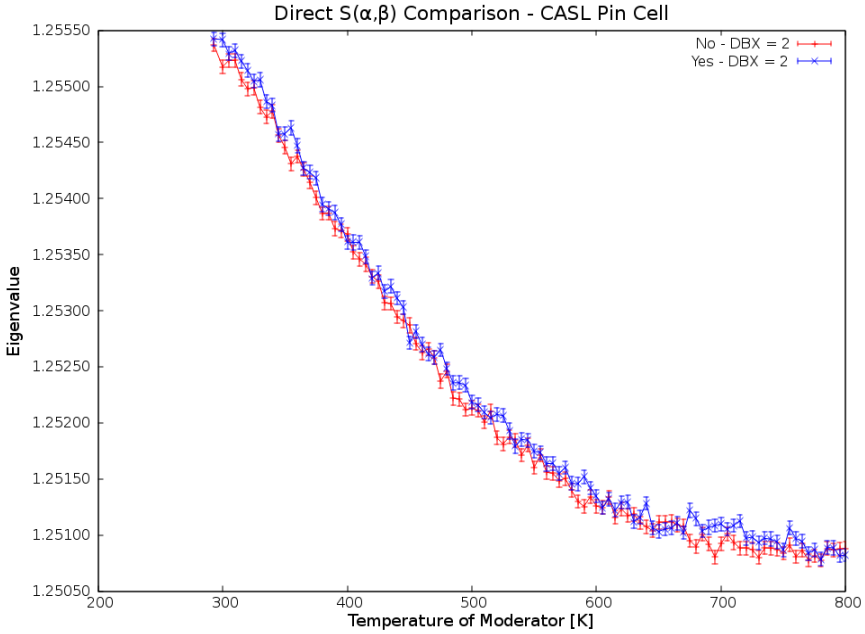

(b) DBX = 2

Figure 7.8: Direct $S(\alpha, \beta)$ results for CASL pin cell (water).

data. While the data is somewhat noisy due to the uncertainty caused by the Monte Carlo simulation, the results when using the direct $S(\alpha, \beta)$ method are generally within one or two standard deviation from using the double differential cross sections.

Graphite Sphere

For the graphite sphere, Figure 7.9a shows the results of using the direct $S(\alpha, \beta)$ method at the library temperatures. Figure 7.9b shows the results when intermediate temperatures are added and interpolation is performed. Again, the data is somewhat noisy, but it is easy to see the overall trend. The direct $S(\alpha, \beta)$ method is generally within one standard deviation, except for the lowest and the highest temperature. Interpolation on both methods yields acceptable results given the reference library temperatures.

Timing and Data Library Sizes

Due to the heterogeneous nature of the computing cluster at the University of Tennessee Department of Nuclear Engineering (http://necluster.engr.utk.edu/), it can be difficult to get timing results for many cases because cases may be run on computers of vastly differing speeds. Table 7.1 shows timing results for a few cases that were run on the same or similar nodes. As can be seen from the table, there is a definite slow-down when direct $S(\alpha, \beta)$ is enabled. This can be attributed to the need to calculate the α CDFs during the scatter sampling. The slow-down depends entirely on how many scattering events occur in the moderator. For these problems the ratio of fuel-to-moderator is not that low, so the slow-down experienced is not that high.

The main benefit of the direct $S(\alpha, \beta)$ method is that the data libraries can be smaller than those associated with the double differential method. Table 7.2 shows the average library size per temperature of some of the common moderators discussed

Table 7.1: Timing results for direct $S(\alpha, \beta)$ cases.

Moderator	Temperature [K]	Double Differential [min]	Direct $S(\alpha, \beta)$ [min]	Slow-Down [%]
H_2O	293.6	578	627	8.5
H_20	800.0	953	1006	5.6
Graphite	296.0	741	807	8.9

Table 7.2: Size of library for direct $S(\alpha, \beta)$.

Moderator	Double Differential [MB]	Direct $S(\alpha, \beta)$ [MB]	% of Double Differential
Hydrogen in Water	21	5	24
Graphite	30	4	13
Beryllium	30	3	10
Polyethylene	17	3	18

in this section. It is important to keep in mind that the direct $S(\alpha, \beta)$ libraries only contain the α F Factors and β CDFs. They still depend on the some features of the original libraries, such as the one-dimensional and elastic scattering cross sections. The current direct $S(\alpha, \beta)$ libraries have also not been optimized. Work can be done to further thin the resultant data and remove duplicate values for the SCT range. Some testing has been done where libraries have been constructed that are under one MB in size.

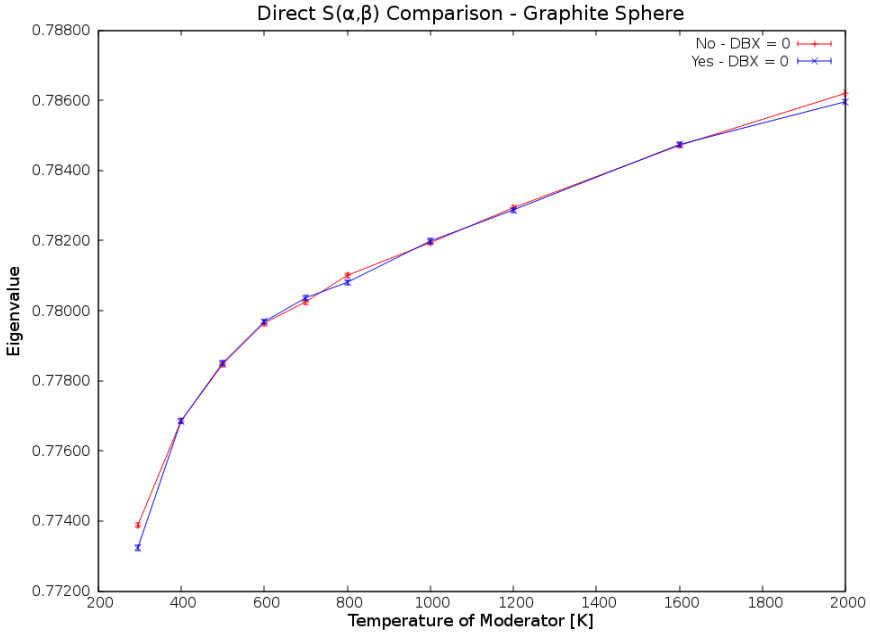

(a) DBX = 0

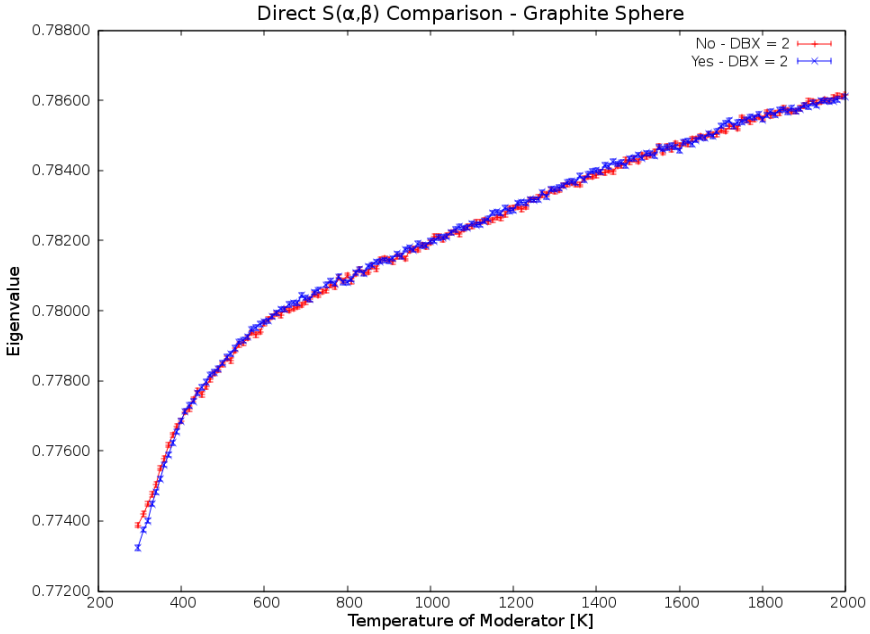

(b) DBX = 2

Figure 7.9: Direct $S(\alpha, \beta)$ results for graphite sphere.

Chapter 8

Benchmark Calculations

While previous chapters demonstrated the effects of Doppler broadening on synthetic problems, this chapter will discuss the impact of Doppler broadening on several benchmarks. Two main benchmark handbooks have been created by various working groups, and several experiments have been pulled from these handbooks and can be used as benchmarking cases.

The International Handbook of Evaluated Criticality Safety Benchmark Experiments (IHECSBE) [41] was prepared by a working group comprised of experienced criticality safety personnel from various countries. The handbook contains criticality safety benchmark specifications that have been derived from experiments performed at various nuclear critical facilities around the world. The benchmark specifications are intended for use by criticality safety engineers to validate calculational techniques used to establish minimum subcritical margins for operations with fissile material. For the purposes of this dissertation, the benchmarks will be used to demonstrate the accuracy of the new Doppler broadening methods. The handbook contains 549 evaluations with almost 5000 benchmark specifications.

The International Handbook of Evaluated Reactor Physics Benchmark Experiments (IHERPhBE) [42] was prepared by a working group of experienced reactor physics personnel. It contains reactor physics benchmark specifications that have

been derived from experiments performed at various nuclear experimental facilities around the world. Like the IHECSBE, the benchmark specifications are intended for use to validate calculation techniques. The most recent edition of the handbook contains data from 53 different experimental series that were performed at 31 different reactor facilities.

Many of the benchmarks in the handbooks were done at room temperature. Therefore one goal was to find several elevated temperature benchmarks that could be used to test the effectiveness of the problem-dependent Doppler broadening methods. Several benchmarks were identified, all at elevated temperatures of around 500 K. Since the closest cross-section libraries provided with SCALE are at 565 K, this should provide a good check for the accuracy of the Doppler broadening methods. Since the temperatures were so low, and the previous cases in Section 4.3 should accurately capture the effect, DBRC was not enabled for these benchmarks.

8.1 Criticality Safety Benchmarks

8.1.1 LEU-COMP-THERM-078 Evaluation

The first evaluation that was modeled is described in full detail in evaluation number LEU-COMP-THERM-078 [43]. The experiment was designed to investigate critical systems with fuel for light water reactors in the enrichment range around 5% ^{235}U. There are fifteen different critical experiments in the evaluation designed to test the effects of different water-hole configurations in the fuel array. All experiments were run at cold (approximately 300 K) conditions; however, Doppler broadening should still be useful as libraries are only provided at 293.6 K. A cut-away view of the critical assembly core tank taken from the evaluation [43] is shown in Figure 8.1.

The first of the experiments had no water holes in the array so it could be used as a baseline for the other experiments. The remaining fourteen experiments contained

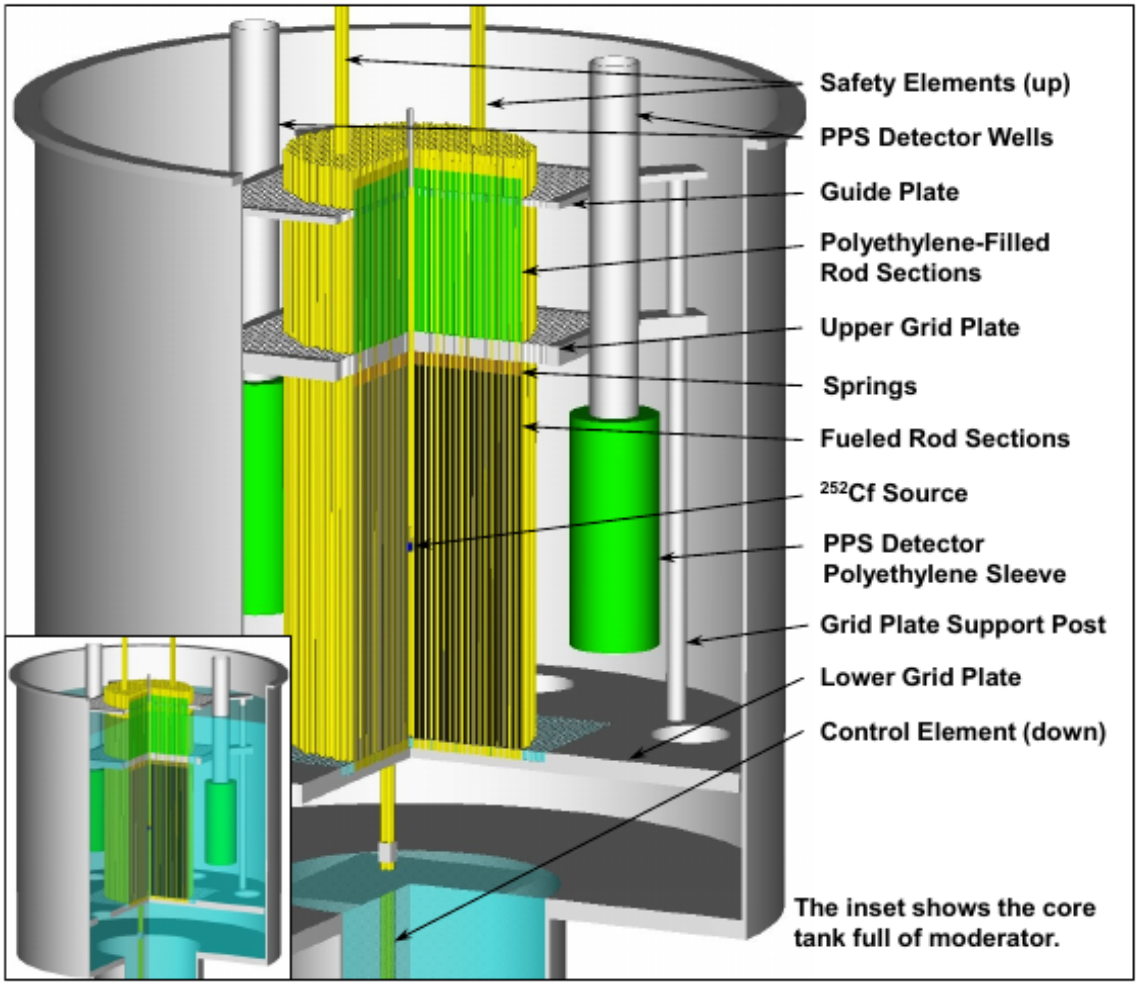

Figure 8.1: Cut-away view of the critical assembly core tank (case two) for LEU-COMP-THERM-078.

various configurations of water holes or water-displacing aluminum rods. Full details for all of the experiments are outside the scope of this dissertation.

The results of running the fifteen benchmark models with KENO-V.a are shown in Table 8.1. MCNP results were taken directly from the evaluation and compared with the KENO results that were run locally. As can be seen in the table, even with a slight temperature error (around 7 K), the results with problem-dependent Doppler broadening enabled (DBX = 2) are more accurate those without (DBX = 0). The

Table 8.1: Benchmark results LEU-COMP-THERM-078 ($\sigma = 0.0002$).

Case	Benchmark	MCNP		KENO		KENO	
		k_{eff}	Ratio	DBX = 0	Ratio	DBX = 2	Ratio
1	0.9995	0.9984	-1.1	0.9977	-1.8	0.9986	-0.9
2	0.9999	0.9990	-0.9	0.9987	-1.2	0.9991	-0.8
3	0.9990	0.9975	-1.5	0.9974	-1.6	0.9979	-1.1
4	0.9986	0.9974	-1.2	0.9973	-1.3	0.9975	-1.1
5	0.9980	0.9970	-1.0	0.9972	-0.8	0.9973	-0.7
6	0.9974	0.9960	-1.4	0.9960	-1.4	0.9964	-1.0
7	0.9994	0.9979	-1.5	0.9979	-1.5	0.9984	-1.0
8	0.9987	0.9973	-1.4	0.9972	-1.5	0.9978	-0.9
9	0.9978	0.9962	-1.6	0.9962	-1.6	0.9968	-1.0
10	0.9969	0.9956	-1.3	0.9953	-1.6	0.9957	-1.2
11	0.9994	0.9981	-1.3	0.9977	-1.7	0.9984	-1.0
12	0.9993	0.9983	-1.0	0.9978	-1.5	0.9980	-1.3
13	0.9993	0.9980	-1.3	0.9976	-1.7	0.9982	-1.1
14	0.9991	0.9981	-1.0	0.9979	-1.2	0.9984	-0.7
15	0.9996	0.9991	-0.5	0.9988	-0.8	0.9989	-0.7
Average			-1.2		-1.4		-1.0

ratio of the error is given as the k_{eff} of the model in MCNP or KENO divided by the benchmark k_{eff}. By using pre-broadening, the ratio is increased from -1.4 to -1.0, which is an improvement over both the original MCNP and KENO results.

8.1.2 LEU-COMP-THERM-026 Evaluation

The second evaluation examined is the LEU-COMP-THERM-026 benchmark [44]. This evaluation contains critical approach experiments with zirconium-clad UO_2 fuel rods (4.92 wt.% ^{235}U) in a water-filled tank. They were performed in the early 1990s in a facility at the Institute of Physics and Power Engineering in Russia.

Cases one through four were modeled in KENO for use in this dissertation. Cases one and two have fuel rods arranged in hexagonal lattices with a pitch of 1.29 cm,

Table 8.2: Sample calculation results LEU-COMP-THERM-026.

Case	Benchmark	MCNP ENDF/B-V	KENO ENDF/B-VII.0 DBX = 0	KENO ENDF/B-VII.0 DBX = 2
1	1.0000 ± 0.0034	0.9977 ± 0.0003	1.0029 ± 0.0003	1.0032 ± 0.0003
2	0.9996 ± 0.0034	0.9980 ± 0.0002	1.0018 ± 0.0003	1.0031 ± 0.0003
3	1.0018 ± 0.0062	0.9982 ± 0.0003	1.0055 ± 0.0003	1.0058 ± 0.0003
4	0.9978 ± 0.0062	0.9960 ± 0.0002	0.9991 ± 0.0002	1.0015 ± 0.0003

and cases three and four have hexagonal lattices with a pitch of 1.09 cm. For each pitch there is a "cold" (∼20^{o}C) and "hot" (about 200^{o}C) case. Odd numbered cases are the cold cases and even numbered cases are the hot cases. Figure 8.2, taken from the evaluation, shows the configuration of the critical assembly. Figure 8.3 shows a cutaway of the KENO 3D model for case two of this evaluation. Figure 8.4 shows a close-up in KENO 3D of the bottom of the fuel. In this figure the zircalloy plugs and lattice structure can be clearly seen. More details on the fuel and lattice structure can be found in the evaluation documentation.

Table 8.2 shows results comparing the evaluation k_{eff} and MCNP results with those obtained from KENO with Doppler broadening disabled and enabled. As can be seen from the table, biases for the hot case are only consistent with the cold case when problem-dependent Doppler broadening is turned on. As an example, for the 1.09 cm pitch cases (three and four) the difference between the benchmark and calculated result is consistently around 400 pcm with Doppler broadening. Without Doppler broadening the k_{eff} for case four (the hot case) is much too low.

Table 8.3 shows the same cases, but run with the direct $S(\alpha, \beta)$ method enabled. The results obtained using direct $S(\alpha, \beta)$ are generally within one standard deviation of the results obtained using the double differential cross sections, with the caveat

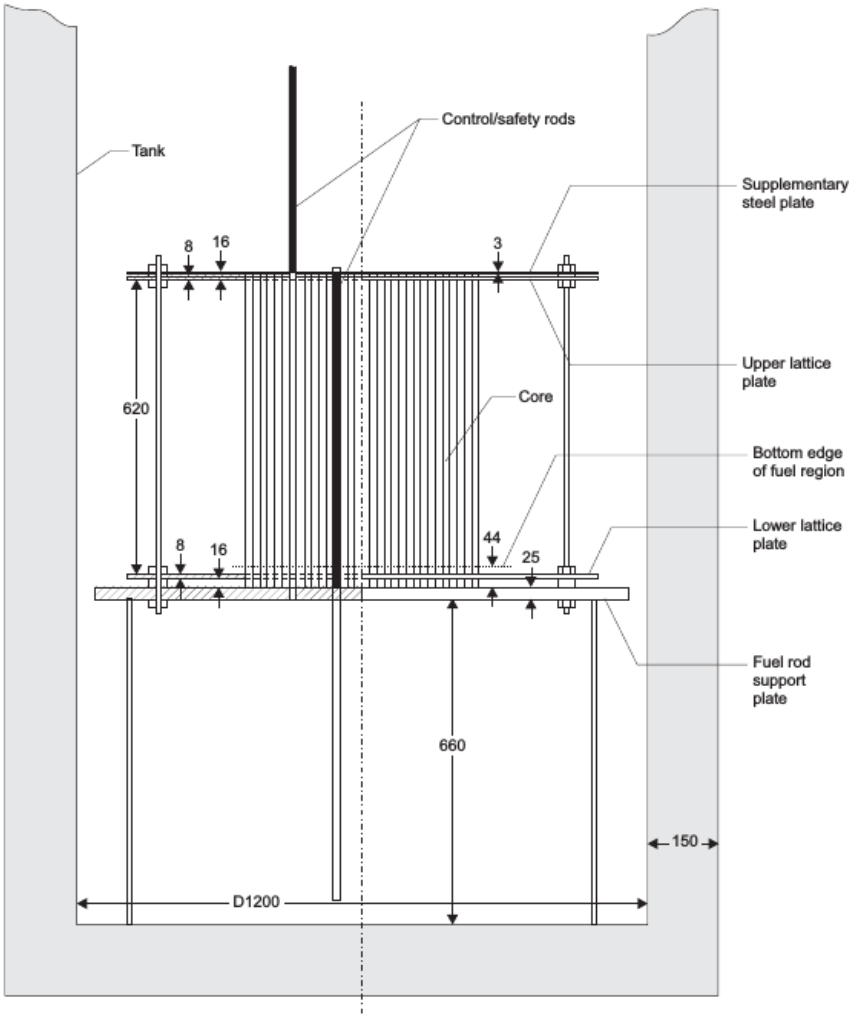

Figure 8.2: Configuration of the critical assembly for LEU-COMP-THERM-26 (dimensions in mm).

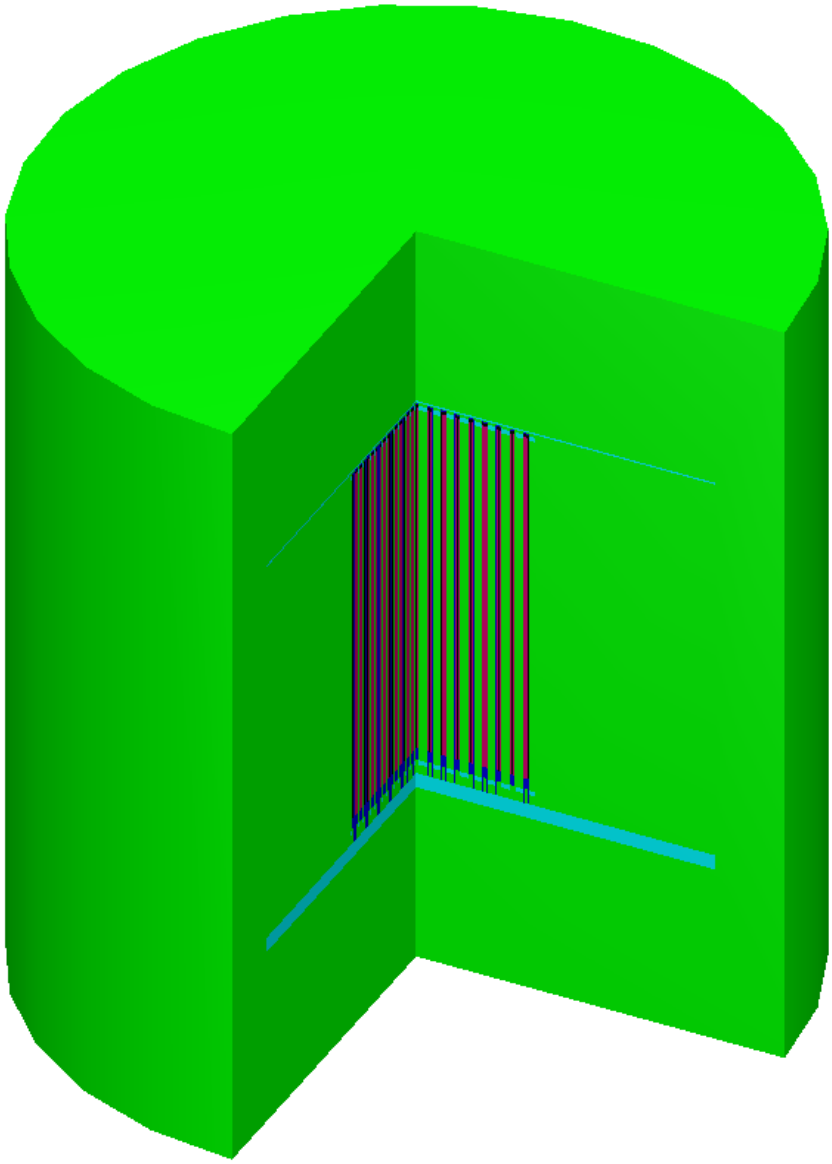

Figure 8.3: KENO 3D representation of case two for evaluation LEU-COMP-THERM-026.

Table 8.3: Sample calculation results LEU-COMP-THERM-026 (with direct $S(\alpha, \beta)$).

Case	Benchmark	KENO ENDF/B-VII.0 DBX = 0	KENO ENDF/B-VII.0 DBX = 2
1	1.0000 ± 0.0034	1.0028 ± 0.0003	1.0030 ± 0.0003
2	0.9996 ± 0.0034	1.0009 ± 0.0003	1.0028 ± 0.0003
3	1.0018 ± 0.0062	1.0051 ± 0.0003	1.0054 ± 0.0003
4	0.9978 ± 0.0062	0.9988 ± 0.0003	1.0020 ± 0.0003

that they are also consistently lower. All results for all methods within one standard deviation of the benchmark k_{eff}.

8.2 Reactor Physics Benchmarks

This section details the results obtained from two different KRITZ reactor evaluations. The KRITZ reactor operated at Studsvik, Sweden during the first half of the nineteen-seventies. It comprised of fuel rods in square-pitched lattices in a 5-m-high, 1.5-m-diameter cylindrical pressure tank. The "KRITZ experiments," performed in the period from September 1972 through February 1973, included several series of criticality experiments on light-water-moderated lattces with uranium dioxide rods, mixed-oxide rods, or both, at room temperature and at temperatures up to ∼250 ^{o}C. [45]

8.2.1 KRITZ-LWR-RESR-001 Evaluation

The first KRITZ evaluation, also known as KRITZ-2:19, is an experiment with mixed-oxide rods at an 18.00 mm pitch. Criticality was obtained by controlling the boron content in the water and by adjusting the water level. A schematic top view of the core, taken from the evaluation, is given in Figure 8.5. As can be seen in the

schematic, the fuel is offset from the center of the tank. The square inner tank is filled with water up to the level needed to achieve criticality. The space beetween the inner tank and the cylindrical outer tank serves as a dump area and is effectively filled with steam.

The numbering of the pin cells taken from the evaluation is shown in Figure 8.6. The figure colors certain pins that have fission rate measurements taken. Certain pins that have high uncertainty are marked with a question mark. Unfortunately, the reference pin at 14,14 has a high uncertainty for the high temperature case. Since fission rates are normalized to this pin, it causes a cascading level of uncertainty that we will see when pin fission rates are calculated with MCNP and KENO.

The experimental, measured, and benchmark-model k_{eff} are given in Table 8.4. As a critical reactor, it is expected that the experimental and measured k_{eff} will be unity. The uncertainty in the measured k_{eff} arises from the erorr in actually measuring the k_{eff} of the reactor. The uncertainty in the experimental k_{eff} arises from the uncertainties of the various parameters in the experimeent such as materials, temperature, and geometry. Due to simplifications made in the model, it was determined that the benchmark k_{eff} will actually be slightly above unity. The benchmark k_{eff} is the value expected to be calculated with the Monte Carlo codes. Table 8.5 shows the benchmark results from MCNP (obtained from the evaluation report) and from KENO. MCNP uses a weighted mixture of cross sections from the two closest temperature libraries to obtain cross sections that are accurate at the desired temperatures. KENO is fairly close to the MCNP results for the cold case when they are both using the ENDF 7.0 library. When the 7.1 library is used, the eigenvalue falls slightly, but is still within two standard deviations of the benchmark. For the hot case, KENO is extremely close to the MCNP JEFF result only when Doppler broadening is enabled. This is expected since the temperature of the hot case is 510 K, which is sufficiently far from the closest library (565 K) to introduce error. The table also shows results when the direct $S(\alpha, \beta)$ method is used. Results

with direct $S(\alpha, \beta)$ are slightly lower than those without, but still very close to the original double differential results.

The KRITZ evaluation also contains fission rate data for a subset of fuel pins at both hot and cold temperatures. Table 8.6 shows the benchmark and calculated fission rates for the cold case. The KENO fission rates are fairly close to the MCNP fission rates, except for pins on the periphery of the core. The pins in the periphery region cause the average difference between the calculated results and the benchmark to be slightly higher for the KENO model. For this case Doppler broadening does not need to be enabled since the fuel is at room temperature.

Table 8.7 shows the fission rates obtained from the evaluation for the hot case. Many of the pins have large error due to the fact that the pin the fission rates are normalized to has a large uncertainty. Table 8.8 shows the fission rates as calculated by KENO. Again, pins in the periphery region have slightly higher errors and all errors are higher than in the cold case due to the high uncertainty of the pin used to normalize the results. However, the KENO results are mostly consistent with those obtained by MCNP and included in the benchmark. More importantly, by enabling the problem dependent Doppler broadening, the error is decreased and becomes closer to the benchmark. The difference between the non-Doppler broadened and Doppler broadened KENO runs is not as stark for the fission rates as it was for k_{eff} since the pin that is being normalized to is also affected by the Doppler broadening.

8.2.2 KRITZ-LWR-RESR-002 Evaluation

The second KRITZ evaluation, also known as KRITZ-2:1, is a rectangular array of low enriched uranium Zircalloy-2 fuel rods in light water. [46] Again, criticality was achieved by regulating the concentration of boron in water and by adjusting the water level. A schematic top view of the core, taken from the evaluation, is given in Figure 8.7. As seen in the schematic, the fuel lattice here is much larger than that in

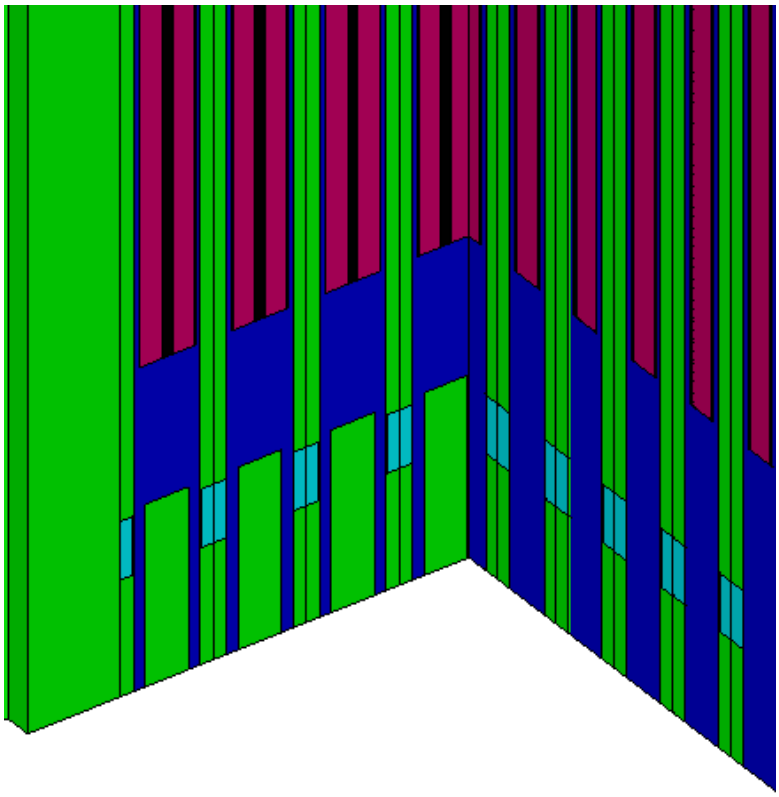

Figure 8.4: KENO 3D of bottom of fuel pins for LEU-COMP-TERM-026 case two.

Table 8.4: Experimental, Measured, and Benchmark-model k_{eff} for KRITZ-LWR-RESR-001.

Case	Measured k_{eff}	Experimental k_{eff}	Benchmark-model k_{eff}
Cold	1.0000 ± 0.0001	1.0000 ± 0.0015	1.0077 ± 0.0030
Hot	1.0000 ± 0.0001	1.0000 ± 0.0019	1.0055 ± 0.0027

Table 8.5: Benchmark results for KRITZ-LWR-RESR-001.

	Cold		Hot	
	k_{eff}	$\frac{C}{E} - 1$ (%)	k_{eff}	$\frac{C}{E} - 1$ (%)
MCNP JEFF 3.1	1.0023 ± 0.0001	-0.54	1.0011 ± 0.0001	-0.44
MCNP ENDF/B-VII.0	1.0031 ± 0.0001	-0.44	-	-
KENO ENDF/B-VII.0 DBX = 0	1.0027 ± 0.0001	-0.50	0.9991 ± 0.0001	-0.64
KENO ENDF/B-VII.0 DBX = 2	-	-	1.0010 ± 0.0001	-0.45
KENO ENDF/B-VII.1 DBX = 0	1.0019 ± 0.0001	-0.58	0.9986 ± 0.0001	-0.69
KENO ENDF/B-VII.1 DBX = 2	-	-	1.0005 ± 0.0001	-0.50
KENO - Direct $S(\alpha, \beta)$ ENDF/B-VII.0 DBX = 0	1.0024 ± 0.0001	-0.52	0.9987 ± 0.0001	-0.68
KENO - Direct $S(\alpha, \beta)$ ENDF/B-VII.0 DBX = 2	-	-	1.0007 ± 0.0001	-0.48

Table 8.6: Fission rates (from benchmark and calculated) normalized to rod (14,14) for KRITZ-LWR-RESR-001 cold case.

Fuel Rod Coordinates		Benchmark	MCNP ENDF/B-VII.0		KENO ENDF/B-VII.0	
X	Y	Result	Calculated	$\frac{C}{E}-1$ (%)	Calculated	$\frac{C}{E}-1$
2	14	0.5571 ± 0.0083	0.5620 ± 0.0015	0.9	0.5251 ± 0.0016	-5.7
3	14	0.5360 ± 0.0080	0.5323 ± 0.0015	-0.7	0.5225 ± 0.0016	-2.5
5	14	0.6412 ± 0.0096	0.6415 ± 0.0017	0.0	0.6470 ± 0.0017	0.9
7	14	0.7648 ± 0.0114	0.7751 ± 0.0019	1.4	0.7784 ± 0.0019	1.8
9	14	0.8688 ± 0.0129	0.8812 ± 0.0019	1.4	0.8870 ± 0.0021	2.1
11	14	0.9731 ± 0.0145	0.9610 ± 0.0020	-1.2	0.9569 ± 0.0021	-1.7
13	14	0.9774 ± 0.0146	0.9997 ± 0.0021	2.3	0.9980 ± 0.0023	2.1
16	14	0.9591 ± 0.0143	0.9845 ± 0.0021	2.7	0.9809 ± 0.0022	2.3
18	14	0.9344 ± 0.0139	0.9254 ± 0.0020	-1.0	0.9257 ± 0.0022	-0.9
20	14	0.8359 ± 0.0125	0.8387 ± 0.0019	0.3	0.8387 ± 0.0020	0.3
22	14	0.7063 ± 0.0105	0.7137 ± 0.0018	1.0	0.7162 ± 0.0019	1.4
23	14	0.6406 ± 0.0095	0.6414 ± 0.0017	0.1	0.6464 ± 0.0018	0.9
25	14	0.5265 ± 0.0078	0.5286 ± 0.0015	0.4	0.5248 ± 0.0016	-0.3
26	14	0.5580 ± 0.0083	0.5656 ± 0.0015	1.4	0.5255 ± 0.0016	-5.8
14	6	0.7697 ± 0.0115	0.7332 ± 0.0018	-4.7	0.7364 ± 0.0019	-4.3
14	8	0.8493 ± 0.0127	0.8565 ± 0.0020	0.8	0.8532 ± 0.0021	0.5
14	10	0.9275 ± 0.0138	0.9417 ± 0.0021	1.5	0.9418 ± 0.0021	1.5
14	12	0.9772 ± 0.0146	0.9901 ± 0.0021	1.3	0.9892 ± 0.0022	1.2
14	14	1.0000 ± 0.0149	1.0000 ± 0.0021	0.0	1.0000 ± 0.0022	0.0
14	15	0.9970 ± 0.0149	0.9879 ± 0.0021	-0.9	0.9898 ± 0.0022	-0.7
14	17	0.9367 ± 0.0140	0.9473 ± 0.0021	1.1	0.9429 ± 0.0021	0.7
14	19	0.8522 ± 0.0127	0.8550 ± 0.0020	0.3	0.8545 ± 0.0020	0.3
14	21	0.7369 ± 0.0110	0.7334 ± 0.0018	-0.5	0.7313 ± 0.0019	-0.8
14	22	0.6641 ± 0.0099	0.6601 ± 0.0017	-0.6	0.6624 ± 0.0018	-0.3
14	23	0.5941 ± 0.0089	0.5930 ± 0.0016	-0.2	0.5964 ± 0.0017	0.4
			Average	1.0		1.6

Table 8.7: Fission rates (from benchmark) normalized to rod (14,14) for KRITZ-LWR-RESR-001 hot case.

Fuel Rod Coordinates		Benchmark	MCNP JEFF 3.1	
X	Y	Result	Calculated	$\frac{C}{E} - 1$ (%)
2	14	0.6953 ± 0.0104	0.7115 ± 0.0017	2.3
3	14	0.5985 ± 0.0089	0.6212 ± 0.0016	3.8
5	14	0.6535 ± 0.0097	0.6830 ± 0.0017	4.5
7	14	0.7644 ± 0.0114	0.7958 ± 0.0019	4.1
9	14	0.8583 ± 0.0128	0.8917 ± 0.0020	3.9
11	14	0.9297 ± 0.0139	0.9572 ± 0.0020	3.0
13	14	0.9486 ± 0.0141	0.9919 ± 0.0021	4.6
16	14	0.9217 ± 0.0139	0.9858 ± 0.0021	7.0
18	14	0.9015 ± 0.0134	0.9344 ± 0.0021	3.7
20	14	0.8170 ± 0.0122	0.8548 ± 0.0020	4.6
22	14	0.7045 ± 0.0105	0.7442 ± 0.0018	5.6
23	14	0.6511 ± 0.0097	0.6920 ± 0.0017	6.3
25	14	0.6054 ± 0.0090	0.6350 ± 0.0017	4.9
26	14	0.6898 ± 0.0103	0.7335 ± 0.0018	6.3
14	6	0.7354 ± 0.0110	0.7568 ± 0.0018	2.9
14	8	0.8216 ± 0.0122	0.8642 ± 0.0019	5.2
14	10	0.8917 ± 0.0133	0.9441 ± 0.0021	5.9
14	12	0.9384 ± 0.0140	0.9873 ± 0.0021	5.2
14	14	1.0000 ± 0.0149	1.0000 ± 0.0021	0.0
14	15	0.9459 ± 0.0141	0.9907 ± 0.0021	4.7
14	17	0.9230 ± 0.0138	0.9466 ± 0.0021	2.6
14	19	0.8329 ± 0.0124	0.8715 ± 0.0019	4.6
14	21	0.7277 ± 0.0108	0.7683 ± 0.0018	5.6
14	22	0.6856 ± 0.0102	0.7109 ± 0.0018	3.7
14	23	0.6435 ± 0.0096	0.6631 ± 0.0017	3.0
			Average	4.1

Table 8.8: Fission rates (calculated) normalized to rod (14,14) for KRITZ-LWR-RESR-001 hot case.

Fuel Rod Coordinates		KENO - DBX = 0		KENO - DBX = 2	
X	Y	Calculated	$\frac{C}{E} - 1$ (%)	Calculated	$\frac{C}{E} - 1$ (%)
2	14	0.6211 ± 0.0017	-10.7	0.6183 ± 0.0017	-11.1
3	14	0.5995 ± 0.0017	0.2	0.5968 ± 0.0017	-0.3
5	14	0.6880 ± 0.0018	5.3	0.6840 ± 0.0018	4.7
7	14	0.8053 ± 0.0020	5.4	0.7984 ± 0.0020	4.5
9	14	0.9004 ± 0.0021	4.9	0.8931 ± 0.0021	4.0
11	14	0.9629 ± 0.0021	3.6	0.9604 ± 0.0022	3.3
13	14	0.9961 ± 0.0022	5.0	0.9933 ± 0.0022	4.7
16	14	0.9880 ± 0.0021	7.2	0.9833 ± 0.0022	6.7
18	14	0.9409 ± 0.0021	4.4	0.9358 ± 0.0021	3.8
20	14	0.8610 ± 0.0020	5.4	0.8551 ± 0.0020	4.7
22	14	0.7513 ± 0.0019	6.6	0.7485 ± 0.0019	6.2
23	14	0.6965 ± 0.0018	7.0	0.6923 ± 0.0018	6.3
25	14	0.6127 ± 0.0017	1.2	0.6092 ± 0.0017	0.6
26	14	0.6410 ± 0.0017	-7.1	0.6381 ± 0.0017	-7.5
14	6	0.7624 ± 0.0019	3.7	0.7596 ± 0.0019	3.3
14	8	0.8715 ± 0.0020	6.1	0.8667 ± 0.0021	5.5
14	10	0.9495 ± 0.0021	6.5	0.9440 ± 0.0021	5.9
14	12	0.9928 ± 0.0023	5.8	0.9913 ± 0.0022	5.6
14	14	1.0000 ± 0.0022	0.0	1.0000 ± 0.0022	0.0
14	15	0.9918 ± 0.0022	4.9	0.9898 ± 0.0021	4.6
14	17	0.9495 ± 0.0022	2.9	0.9483 ± 0.0021	2.7
14	19	0.8745 ± 0.0020	5.0	0.8695 ± 0.0020	4.4
14	21	0.7683 ± 0.0019	5.6	0.7683 ± 0.0019	5.6
14	22	0.7137 ± 0.0019	4.1	0.7101 ± 0.0019	3.6
14	23	0.6608 ± 0.0019	2.7	0.6565 ± 0.0018	2.0
		Average	4.8		4.5

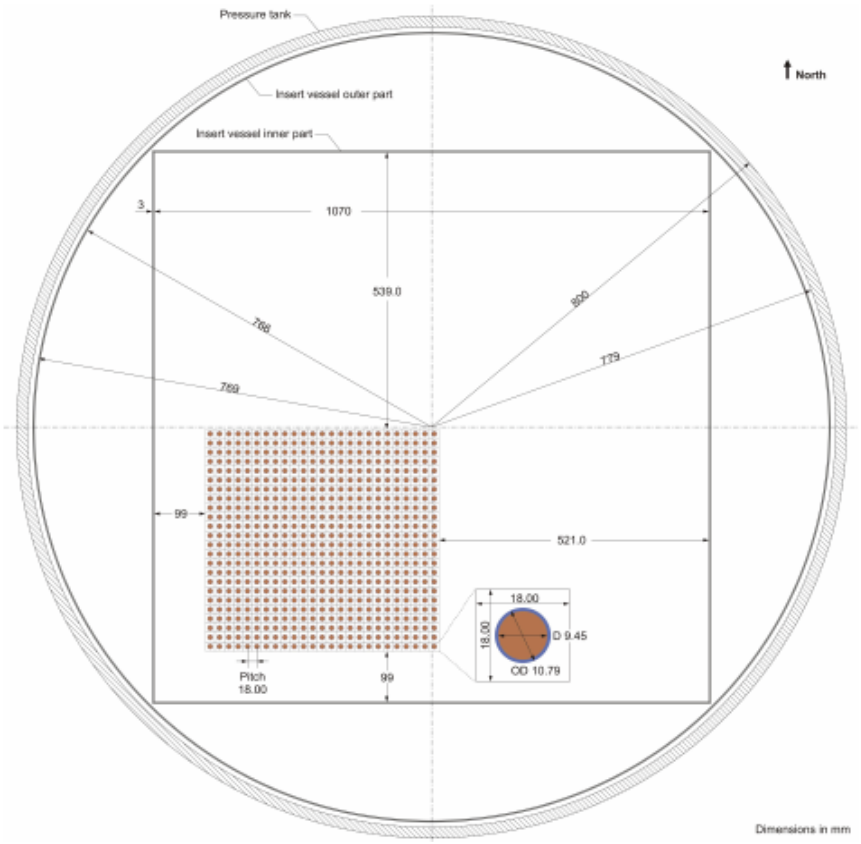

Figure 8.5: Schematic top view of the KRITZ-2:19 core.

KRITZ-2:19 (see Section 8.2.1). A cut-away drawing of the core done in KENO 3D is shown in Figure 8.8.

The numbering of the pin cells taken from the evaluation is shown in Figure 8.9. The figure colors certain pins that have fission rate measurements taken. Certain pins that have high uncertainty are marked with a question mark. Unlike the previous KRITZ model, the pin the fission rates are normalized to does not have a high uncertainty. This should make the fission rates calculated with MCNP and KENO closer to the benchmark values.

Table 8.9: Experimental, Measured, and Benchmark-model k_{eff} for KRITZ-LWR-RESR-002.

Case	Measured k_{eff}	Experimental k_{eff}	Benchmark-model k_{eff}
Cold	1.0000 ± 0.0001	1.0000 ± 0.0018	1.0025 ± 0.0020
Hot	1.0000 ± 0.0001	1.0000 ± 0.0026	1.0024 ± 0.0028

The experimental, measured, and benchmark-model k_{eff} are given in Table 8.9. The statements regarding the k_{eff} values made in regards to KRITZ-2:19 (Section 8.2.1) also apply for this KRITZ case. Table 8.10 shows the benchmark results from MCNP (obtained from the evaluation report) and from KENO. Again, MCNP uses a weighted mixture of cross sections from the two closest libraries to obtain cross sections that are accurate at the desired temperatures. For the cold case, KENO is actually slightly closer to the benchmark values than MCNP. For the hot case, KENO is slightly further away from the benchmark than MCNP. Without Doppler broadening, the KENO results are particularly off the benchmark. Enabling Doppler broadening increases the k_{eff} by ∼150 pcm and makes the results closer to the benchmark. Like previous cases, enabling direct $S(\alpha, \beta)$ lowers the k_{eff} by ∼10 pcm, which is generally within one standard deviation.

This evaluation also contains fission rates, but only for the hot case. Fission rates obtained from the evaluation for MCNP are shown in Table 8.11. Fission rates calculated by KENO are shown in Table 8.12. The KENO results are mostly consistent with the MCNP results. The highest error, in pin (15,30), occurs in a pin that has been marked as having a high degree of uncertainty. The error is slightly decreased when enabling the problem dependent Doppler broadening, but since the pins are normalized the overall differences are not large.

Table 8.10: Benchmark results for KRITZ-LWR-RESR-002.

	Cold		Hot	
	k_{eff}	$\frac{C}{E} - 1$ (%)	k_{eff}	$\frac{C}{E} - 1$ (%)
MCNP JEFF 3.1	0.9975 ± 0.0001	-0.50	0.9992 ± 0.0001	-0.33
MCNP ENDF/B-VII.0	0.9981 ± 0.0001	-0.43	-	-
KENO ENDF/B-VII.0 DBX = 0	0.9990 ± 0.0001	-0.35	0.9958 ± 0.0001	-0.66
KENO ENDF/B-VII.0 DBX = 2	-	-	0.9973 ± 0.0001	-0.51
KENO - Direct $S(\alpha, \beta)$ ENDF/B-VII.0 DBX = 0	0.9989 ± 0.0001	-0.36	0.9957 ± 0.0001	-0.67
KENO - Direct $S(\alpha, \beta)$ ENDF/B-VII.0 DBX = 2	-	-	0.9971 ± 0.0001	-0.53

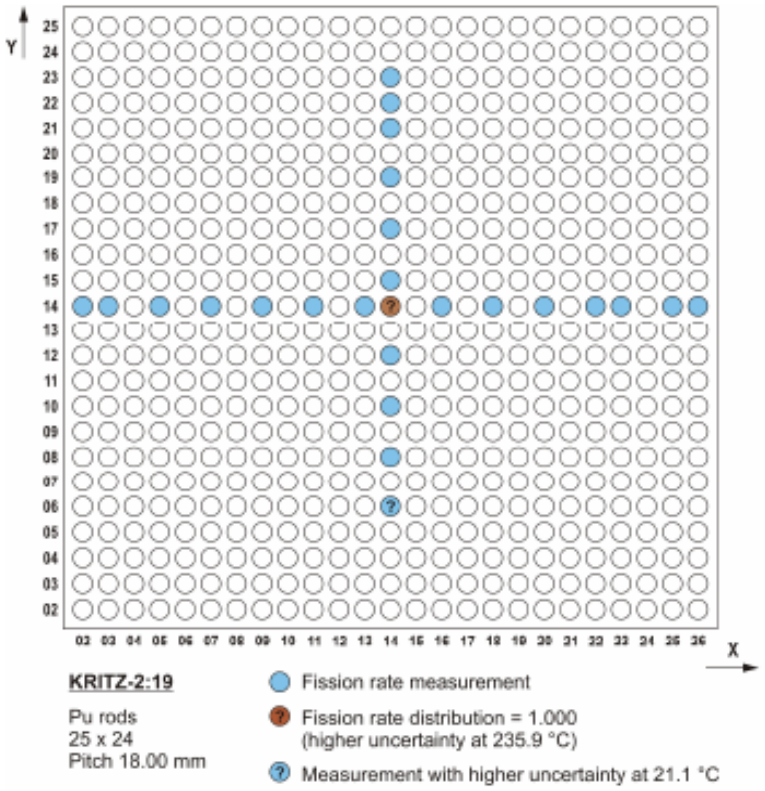

Figure 8.6: Numbering of the fuel-rod columns and rows for the KRITZ-2:19 core.

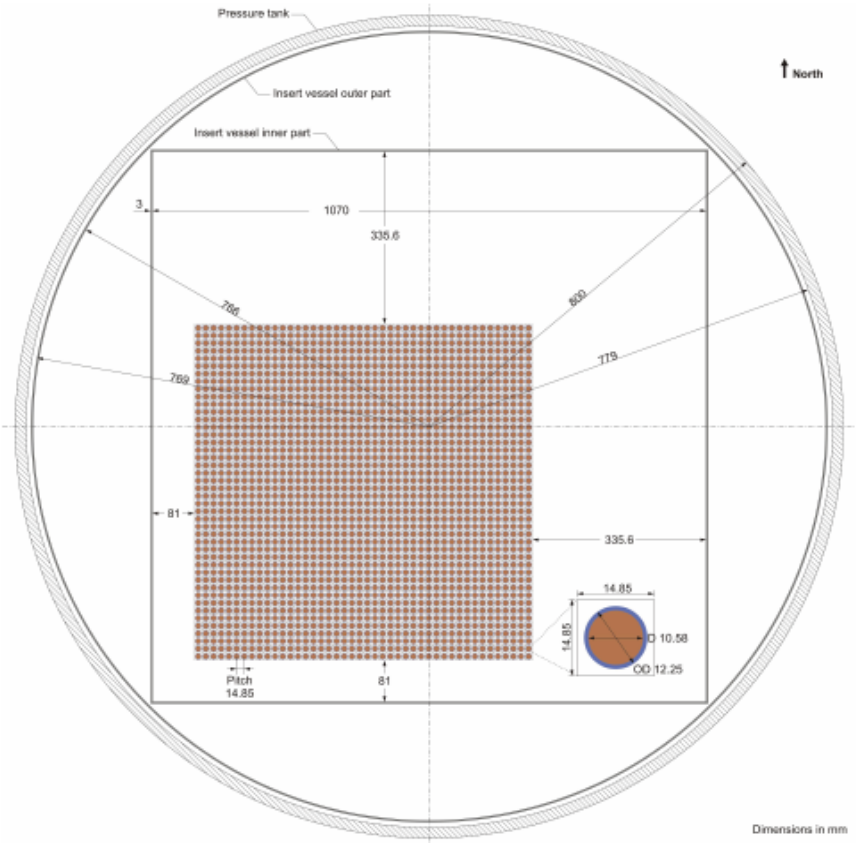

Figure 8.7: Schematic top view of the KRITZ-2:1 core.

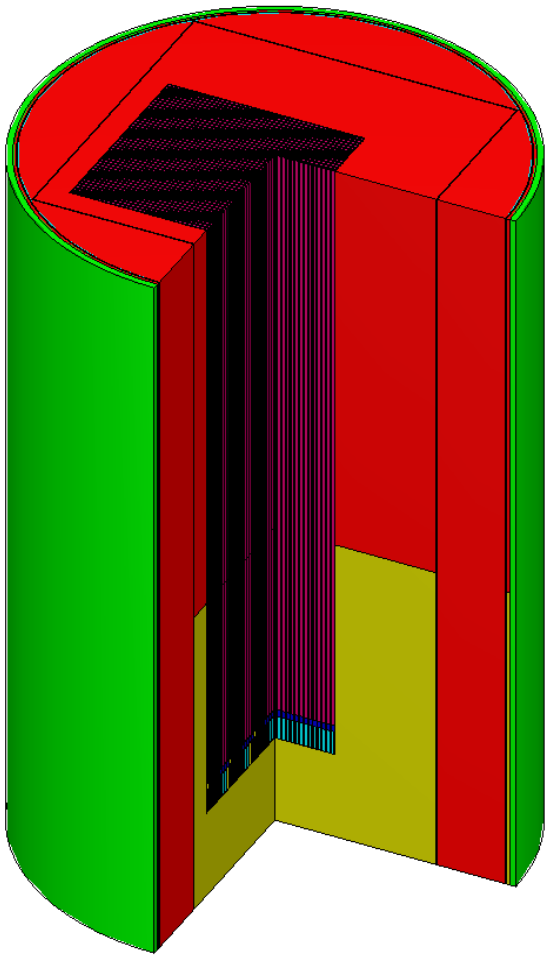

Figure 8.8: Cut-away of KRITZ-2:1 core done in KENO 3D.

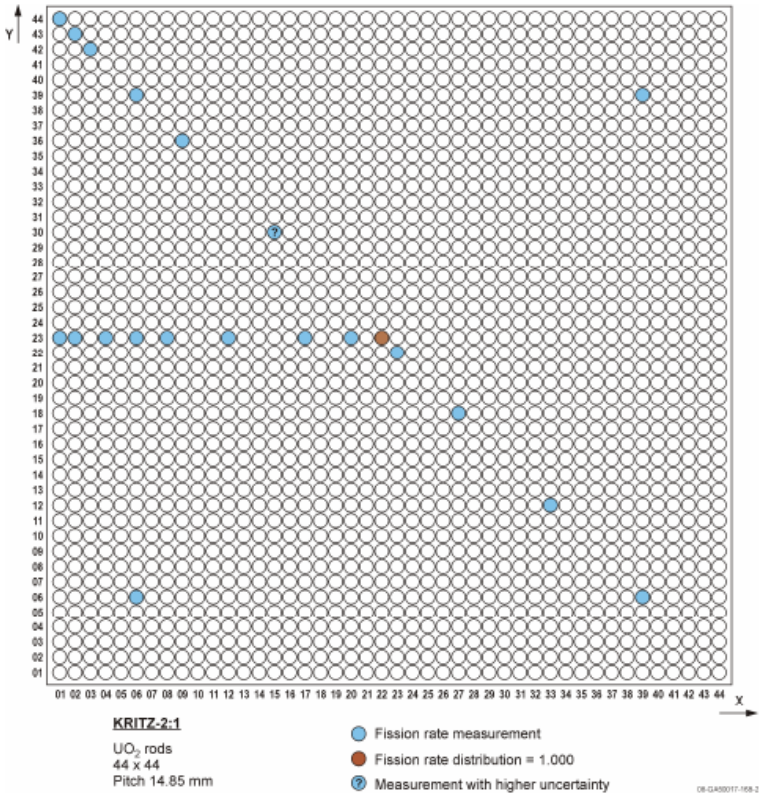

Figure 8.9: Numbering of the fuel-rod columns and rows for the KRITZ-2:1 core.

Table 8.11: Fission rates (from benchmark) normalized to rod (22,23) for KRITZ-LWR-RESR-002 hot case.

Fuel Rod Coordinates		Benchmark	MCNP	
X	Y	Result	Calculated	$\frac{C}{E} - 1$ (%)
1	23	0.7133 ± 0.0098	0.7229 ± 0.0024	1.35
1	44	0.4309 ± 0.0059	0.4385 ± 0.0019	1.76
2	23	0.5899 ± 0.0081	0.5890 ± 0.0021	-0.15
2	43	0.3431 ± 0.0047	0.3424 ± 0.0016	-0.19
3	42	0.3140 ± 0.0043	0.3107 ± 0.0015	-1.07
4	23	0.5689 ± 0.0078	0.5495 ± 0.0020	-3.41
6	6	0.3763 ± 0.0053	0.3768 ± 0.0016	0.13
6	23	0.6231 ± 0.0085	0.6132 ± 0.0021	-1.60
6	39	0.3954 ± 0.0054	0.3874 ± 0.0016	-2.01
8	23	0.7074 ± 0.0097	0.6926 ± 0.0022	-2.09
9	36	0.5653 ± 0.0077	0.5416 ± 0.0019	-4.19
12	23	0.8602 ± 0.0118	0.8320 ± 0.0024	-3.28
15	30	0.7902 ± 0.0108	0.8426 ± 0.0024	6.63
17	23	0.9670 ± 0.0132	0.9553 ± 0.0026	-1.21
20	23	0.9868 ± 0.0135	0.9886 ± 0.0026	0.18
22	23	1.0000 ± 0.0137	1.0000 ± 0.0026	0.00
23	22	0.9965 ± 0.0137	0.9973 ± 0.0026	0.08
27	18	0.9679 ± 0.0133	0.9367 ± 0.0025	-3.23
33	12	0.7071 ± 0.0097	0.7056 ± 0.0022	-0.21
39	6	0.3832 ± 0.0052	0.3839 ± 0.0016	0.17
39	39	0.4025 ± 0.0055	0.3942 ± 0.0017	-2.06
			Average	1.67

Table 8.12: Fission rates (calculated) normalized to rod (22,23) for KRITZ-LWR-RESR-002 hot case.

Fuel Rod Coordinates		KENO - DBX = 0		KENO - DBX = 2	
X	Y	Calculated	$\frac{C}{E} - 1$ (%)	Calculated	$\frac{C}{E} - 1$ (%)
1	23	0.7141 ± 0.0026	0.11	0.7133 ± 0.0025	0.05
1	44	0.4277 ± 0.0020	-0.75	0.4284 ± 0.0020	-0.57
2	23	0.5805 ± 0.0022	-1.60	0.5825 ± 0.0022	-1.26
2	43	0.3353 ± 0.0017	-2.28	0.3366 ± 0.0017	-1.90
3	42	0.3065 ± 0.0016	-2.39	0.3063 ± 0.0016	-2.45
4	23	0.5471 ± 0.0021	-3.84	0.5483 ± 0.0021	-3.62
6	6	0.3766 ± 0.0018	0.09	0.3753 ± 0.0017	-0.25
6	23	0.6146 ± 0.0022	-1.36	0.6102 ± 0.0022	-2.07
6	39	0.3823 ± 0.0018	-3.30	0.3848 ± 0.0018	-2.67
8	23	0.6877 ± 0.0024	-2.79	0.6907 ± 0.0023	-2.36
9	36	0.5395 ± 0.0020	-4.57	0.5383 ± 0.0020	-4.78
12	23	0.8306 ± 0.0027	-3.45	0.8284 ± 0.0025	-3.69
15	30	0.8372 ± 0.0026	5.95	0.8339 ± 0.0026	5.53
17	23	0.9520 ± 0.0027	-1.56	0.9459 ± 0.0028	-2.18
20	23	0.9944 ± 0.0028	0.77	0.9839 ± 0.0028	-0.29
22	23	1.0000 ± 0.0029	0.00	1.0000 ± 0.0028	0.00
23	22	0.9962 ± 0.0028	-0.03	0.9975 ± 0.0028	0.10
27	18	0.9366 ± 0.0027	-3.23	0.9372 ± 0.0027	-3.17
33	12	0.6971 ± 0.0024	-1.41	0.6994 ± 0.0023	-1.09
39	6	0.3803 ± 0.0018	-0.75	0.3832 ± 0.0017	0.01
39	39	0.3928 ± 0.0018	-2.41	0.3940 ± 0.0017	-2.36
		Average	2.03		1.93

Chapter 9

Conclusions

9.1 Summary of Conclusions

The primary goal of the research and development presented in this dissertation is to enable temperature correction and Doppler broadening in the SCALE Monte Carlo code KENO. Accomplishing this goal involved surveying the current research in the field, analyzing how it could be successfully applied, and developing additional new methods. Current thermal scattering techniques generally assume that the target nuclide is stationary. It was shown that this can cause a significant impact on the resultant eigenvalue when certain heavy nuclides are used. The DBRC method was implemented into KENO in order to remove this assumption. While ^{238}U seems to be the primary heavy nuclide of interest, other nuclides and isotopes were modeled with DBRC to show their impact. It was shown that as the temperature increases, the impact of DBRC becomes more and more pronounced. For high temperature reactors, the change in the eigenvalue due to the DBRC method can be as high as 500 pcm based on results herein shown.

Temperature dependence of cross-section data was also examined. Typically reactor analysis tools ship with only a subset of temperatures that a reactor physics analyst needs in order to accurately model a problem. A one-dimensional method

to Doppler broaden cross sections was expanded and coded into KENO. By using this method, cross sections can be Doppler broadened to any temperature that the user selects. Doppler broadening is done before neutron transport begins, therefore it has been christened as problem-dependent Doppler pre-broadening. This method differs from ongoing research in other codes such as MCNP where fits are established versus temperature data and cross sections are calculated "on-the-fly." Using the temperature corrected data shows an immediate impact when a temperature that is not on a library is used. Having correct temperatures for each fuel and moderator region will become increasingly important as Monte Carlo is used to model full reactors. It is also a paramount ability if accurate coupling to thermal-hydraulic codes is desired.

In addition to Doppler broadening the one-dimensional cross sections, temperature correcting the two-dimensional kinematics data was also examined. Currently KENO uses CDFs of the double differential scattering cross section in order to calculate the exit energy and scattering cosine of a neutron undergoing a scatter with a thermal moderator. These are based on data provided by ENDF files and exist at a set of fixed temperatures. Like the one-dimensional cross sections, an inaccurate eigenvalue can be obtained if a temperature desired is not one of the temperatures provided. A unit-base interpolation scheme was devised and implemented for the energy and scattering cosine CDFs. It was shown that by using this method more accurate results could be obtained at the intermediate temperatures.

Incoherent inelastic scattering provides a unique case to solve. Parameters for the double differential cross section in this case are generally provided using $S(\alpha, \beta)$ values. A proof-of-concept method was developed to interpolate on these $S(\alpha, \beta)$ values before generating the scattering cosine and exit energy CDFs. The results from this method were promising, but it added unnecessary complexity to the code base and slows down the start of the problem more than any of the other methods. One unique way that incoherent inelastic scattering can be modeled is by using the $S(\alpha, \beta)$ data directly. This method is called the direct $S(\alpha, \beta)$ method and utilizes

$S(\alpha, \beta)$ CDFs instead of the exit energy and scattering cosine CDFs used for the double differential method. The main benefit of using this method is that the α CDFs can be calculated as needed, and therefore do not need to be saved for every β on the cross-section library. This results in a much lower storage requirement, but is balanced by a slightly longer run-time (about 10%). Test cases were run using the direct $S(\alpha, \beta)$ method and they compared favorably with the original results. The α and β CDFs can also be interpolated using the same unit-base interpolation scheme as used on the exit energies and scattering cosines in order to correct for temperature dependence.

To verify the accuracy of the new methods a variety of benchmarks taken from evaluations in the IHECSBE and IHERPhBE were used. Efforts were made to find evaluations that contained cases that were run at an elevated temperature in order to test the effectiveness of the Doppler broadening mechanisms. Overall, the results became more accurate when the Doppler broadening methods were used. This is not unexpected as without Doppler broadening, the incorrect cross sections are used. However, it is still interesting and vital to see the impact that the temperature has on both the eigenvalue and fission rates. In the future, as model complexity and multi-physics couplings increase, it will become more and more important to have accurate cross section and scattering methodology.

9.2 Suggestions for Future Work

There remains a significant amount of additional research and development that can be accomplished to enhance the hereto described methods and capabilities. Selected additional work includes:

1. Additional methods to correct for the thermal motion of a target nuclide have been developed other than DBRC. It should be possible to implement these methods into KENO and see their impact and compare them with the DBRC method.

2. Work can be done on implementing the exact scattering kernel into the multigroup codes developed at ORNL. Some work has been done previously in order to try and develop a method for calculating the exact scattering kernel and tying it into the AMPX code, but this work is incomplete. By introducing the exact scattering kernel into multigroup codes, users would have a quick way to access this feature without having to rely on the sometimes slow-running Monte Carlo method. It would also serve as a way to test the implementation of DBRC and other methods.

3. While the methods developed in this dissertation cover Doppler *pre*-broadening, it should be possible to develop them into a true "on-the-fly" method. In this method, cross sections would be Doppler broadened as they are needed. While it could be difficult for the finite difference method to adapt, other methods could be explored which would be more suited for this type of application.

4. The direct $S(\alpha, \beta)$ method can continue to be refined. Currently the meshing technique used to create the α and β grids is very coarse. Thinning these meshes should provide immediate benefits in terms of memory consumption and speed. Work to eliminate the run-time overhead associated with calculating the α CDFs would also be beneficial. Ideas including using some of the double differential data along side the $S(\alpha, \beta)$ data could decrease the run-time while maintaining the memory benefits associated with the direct $S(\alpha, \beta)$ method.

5. ORNL is currently developing a next generation Monte Carlo code named SHIFT [47]. Work could be done to implement the methods that were developed and implemented into KENO into SHIFT. As the popularity of SHIFT increases, it will become more desirable to have feature parity among ORNL codes.

References

[1] Oak Ridge National Laboratory, Oak Ridge, Tennessee, *Scale: A Comphrehensive Modeling and Simulation Suite for Nuclear Safety Analysis and Design*, June 2011. ORNL/TM-2005/39. xiii, 31, 34

[2] J. J. Duderstadt and L. J. Hamilton, *Nuclear Reactor Analysis*. Wiley, 1976. 6, 17

[3] E. E. Lewis, *Computational Methods of Neutron Transport*. Wiley-Interscience, 1993. 6, 25, 29

[4] W. M. Stacey, *Nuclear Reactor Physics (Second edition)*. Wiley-VCH, 2007. 6

[5] A. Trkov, M. Herman, and D. Brown, "ENDF-6 Formats Manual," tech. rep., Report BNL-90365-2009 Rev. 2, Brookhaven National Laboratory, Upton, New York, 2011. 7, 20, 21

[6] M. Dunn and N. Greene, "Ampx-2000: A cross-section processing system for generating nuclear data for criticality safety applications," *Trans. Am. Nucl. Soc*, vol. 86, pp. 118–119, 2002. 9

[7] Oak Ridge National Laboratory, *SCALE: A Modular Codes System for Performing Standardized Computer Analyses for Licensing Evaluation*, I–III ed., June 2011. Version 6, ORNL/TM-2005/39. 9, 66

[8] D. E. Cullen and C. R. Weisbin, "Exact doppler broadening of tabulated cross sections," *Nuclear Science and Engineering*, vol. 60, no. 3, pp. 199–229, 1976. 9

[9] D. Hollenbach, L. Petrie, S. Goluoglu, N. Landers, and M. Dunn, "KENO-VI: A general quadratic version of the keno program," tech. rep., Oak Ridge National Laboratory, Oak Ridge, TN, 2011. 11, 32

[10] N. M. Greene, "BONAMI: Resonance self-shielding by the Bondarenko method," Tech. Rep. ORNL/TM-2005/39, Oak Ridge National Laboratory, June 2011. Version 6.1, Sect. F1. 13, 16

[11] M. L. Williams and D. F. Hollenbach, "CENTRM: A one-dimensional neutron transport code for computing pointwise energy spectra," Tech. Rep. ORNL/TM-2005/39, Oak Ridge National Laboratory, June 2011. Version 6.1, Sect. F18. 13

[12] M. L. Williams and D. F. Hollenbach, "PMC: A program to produce multigroup cross ssection using pointwise energy spectra from CENTRM," Tech. Rep. ORNL/TM-2005/39, Oak Ridge National Laboratory, June 2011. Version 6.1, Sect. F19. 16

[13] K. D. Kok, ed., *Nuclear Engineering Handbook (Mechanical and Aerospace Engineering Series)*. CRC Press, 2009. 18

[14] E. P. Wigner and J. Wilkins Jr, "Effect of the temperature of the moderator on the velocity distribution of neutrons with numerical calculations for h as moderator," Tech. Rep. AECD-2275, Oak Ridge National Laboratory, 1944. 24

[15] W. Rothenstein and R. Dagan, "Two-body kinetics treatment for neutron scattering from a heavy maxwellian gas," *Annals of Nuclear Energy*, vol. 22, no. 11, pp. 723–730, 1995. 40, 54

[16] W. Rothenstein, "Neutron scattering kernels in pronounced resonances for stochastic doppler effect calculations," *Annals of Nuclear Energy*, vol. 23, no. 4, pp. 441–458, 1996. 40

[17] W. Rothenstein and R. Dagan, "Ideal gas scattering kernel for energy dependent cross-sections," *Annals of Nuclear Energy*, vol. 25, no. 4, pp. 209–222, 1998. 40, 41, 54

[18] W. Rothenstein, "Proof of the formula for the ideal gas scattering kernel for nuclides with strongly energy dependent scattering cross sections," *Annals of Nuclear Energy*, vol. 31, no. 1, pp. 9–23, 2004. 40

[19] R. Dagan and C. Broeders, "On the effect of resonance dependent scattering-kernel on fuel cycle and inventory," *PHYSOR-2006, Vancouver, Canada*, 2006. 41

[20] B. Becker, R. Dagan, and G. Lohnert, "Proof and implementation of the stochastic formula for ideal gas, energy dependent scattering kernel," *Annals of Nuclear Energy*, vol. 36, no. 4, pp. 470–474, 2009. 41, 43, 54, 58

[21] G. Arbanas, M. E. Dunn, N. M. Larson, L. C. Leal, M. L. Williams, B. Becker, and R. Dagan, "Computation of temperature-dependent legendre moments of a double-differential elastic cross section," in *Proceedings of International Conference on Mathematics and Computational Methods Applied to Nuclear Science and Engineering,(Rio de Janeiro, Brazil)*, 2011. 41, 42

[22] M. Ouisloumen and R. Sanchez, "A model for neutron scattering off heavy isotopes that accounts for thermal agitation effects," *Nuclear Science and Engineering;(United States)*, vol. 107, no. 3, 1991. 41, 42, 45

[23] S. Ghrayeb, M. Ouisloumen, A. Ougouag, and K. Ivanov, "Multigroup computation of the temperature-dependent resonance scattering model (rsm) and its implementation," tech. rep., American Nuclear Society, Inc., 555 N. Kensington Avenue, La Grange Park, Illinois 60526 (United States), 2012. 44

[24] D. Lee, K. Smith, and J. Rhodes, "The impact of ^{238}u resonance elastic scattering approximations on thermal reactor doppler reactivity," *Annals of Nuclear Energy*, vol. 36, no. 3, pp. 274–280, 2009. 44, 66

[25] G. Yesilyurt, W. R. Martin, and F. Brown, "On-The-Fly Doppler Broadening for Monte Carlo Codes," in *International Conference on*

Mathematics, Computational Methods & Reactor Physics, (Saratoga Springs, New York), ANS, 2009. May 3–7. 46

[26] G. Yesilyurt, W. R. Martin, and F. B. Brown, "On-the-Fly Doppler Broadening for Monte Carlo Codes," *Nuclear Science and Engineering*, vol. 171, no. 3, pp. 239–257, 2012. 46

[27] F. B. Brown, W. R. Martin, G. Yesilyurt, and S. Wilderman, "Progress with On-The-Fly Neutron Doppler Broadening in MCNP," in *Transactions of the American Nuclear Society*, (Chicago, Illinois), ANS, 2012. June 24–28. 46

[28] W. R. Martin, S. Wilderman, F. B. Brown, and G. Yesilyurt, "Implementation of On-the-Fly Doppler Broadening in MCNP," in *International Conference on Mathematics and Computational Methods Applied to Nuclear Science & Engineering*, (Sun Valley, Idaho), ANS, 2013. May 5–9. 46, 48

[29] T. Trumbull and T. Fieno, "Temperature interpolation of thermal neutron incoherent inelastic scattering data in monte carlo calculations," *Trans. Am. Nucl. Soc*, vol. 107, pp. 991–997, 2012. 48

[30] C. T. Ballinger, "The direct $S(\alpha, \beta)$ method for thermal neutron scattering," in *Proceedings of the International. Conference on Mathematics and Computation, Reactor Physics, and Environmental Analysis*, pp. 134–143, 1995. 48, 107

[31] R. J. Doyas and S. T. Perkins, "Interpolation of tabular secondary neutron and photon energy distributions," *Nucl. Sci. Eng*, vol. 50, pp. 390–392, 1973. 49, 90

[32] X-5 Monte Carlo Team, "MCNP–a general purpose monte carlo n-particle transport code," Tech. Rep. LA-UR-03-1987, Los Alamos National Laboratory, April 2003. Version 5. 51, 105

[33] M. Lee, H. Joo, D. Lee, and K. Smith, "A feasibility study of cmfd acceleration in monte carlo eigenvalue calculation," in *Trans. of KNS Autumn Meeting, CD-ROM*, 2009. 57

[34] M. Jessee and M. DeHart, "Newt: A new transport algorithm for two-dimensional discrete-ordinates analysis in non-orthogonal geometries," Tech. Rep. ORNL/TM-2005/39, Oak Ridge National Laboratory, June 2011. Version 6.1, Sect. F21. 58

[35] E. A. Villarino, R. J. Stammler, A. A. Ferri, and J. J. Casal, "Helios: angularly dependent collision probabilities," *Nucl. Sci. Eng*, vol. 112, no. 161992, p. 3, 1992. 65

[36] M. A. Jessee and M. D. DeHart, "TRITON: A multipurpose transport, depletion, and sensitivity and uncertainty analysis module," Tech. Rep. ORNL/TM-2005/39, Oak Ridge National Laboratory, June 2011. Version 6.1, Sect. T1. 66

[37] R. D. Mosteller, "The doppler-defect benchmark: Overview and summary of results," *Fuel*, vol. 239, no. 240Pu, p. 241Pu, 2007. 67

[38] L. C. Leal and R. Hwang, "A Finite Difference Method for Treating the Doppler Broadening of Neutron Cross Sections," in *American Nuclear Society*, (Los Angles, CA), Nov 1987. 71

[39] F. Bischoff, M. Yeater, and W. Moore, "Monte carlo evaluation of multiple scattering and resolution effects in double-differential neutron scattering cross-section measurements," *Nucl. Sci. Eng*, vol. 48, pp. 266–280, 1972. 106

[40] G. M. Borgonovi, "Neutron scattering kernels calculations at epithermal energies," Tech. Rep. GA-9950, Gulf General Atomic, Mar 1970. 111

[41] J. B. Briggs *et al.*, "International handbook of evaluated criticality safety benchmark experiments," *Report NEA/DOC (95)*, vol. 4, 2004. 126

[42] N. N. S. Committee *et al.*, "International handbook of evaluated reactor physics benchmark experiments," tech. rep., NEA/NSC/DOC, 2006. 126

[43] G. A. Harms, "Water-Moderated Square-Pitched U(6.90)o_2 Fuel Rod Lattices with 0.52 Fuel-to-Water Volume Ratio," Tech. Rep. LEU-COMP-THERM-078, Sandia National Laboratories, July 2013. 127

[44] A. Tsiboulia, Y. Rozhikhin, and V. Lependin, "Water-Moderated U(4.92)o_2 Fuel Rods in 1.29, 1.09, and 1.01 cm Pitch Hexagonal Lattices at Different Temperatures," Tech. Rep. LEU-COMP-THERM-026, Institute of Physics and Power Engineering, September 2003. 129

[45] L. Snoj and J. C. Gehin, "KRITZ-2:19 Experiment on Regular H_2O/Fuel Pin Lattices with Mixed Oxide Fuel at Temperatures 21.1 and 235.9 ^{o}C," Tech. Rep. KRITZ-LWR-RESR-001, Jozef Sefan Institute and Oak Ridge National Laboratory, March 2009. 133

[46] L. Snoj and J. C. Gehin, "KRITZ-2:1 Experiment on Regular H_2O/Fuel Pin Lattices with Low Enriched Uranium Fuel at Temperatures 248.5 ^{o}C," Tech. Rep. KRITZ-LWR-RESR-002, Jozef Sefan Institute and Oak Ridge National Laboratory, March 2009. 135

[47] N. C. Sly, B. T. Mervin, S. W. Mosher, T. M. Evans, J. C. Wagner, and G. I. Maldonado, "Verification of the shift monte carlo code with the c5g7 reactor benchmark," in *Advances in Reactor Physics: Linking Research, industry, and Education (PHYSOR 2012)*, (Knoxville, TN), Apr. 15–20 2012. 153

Appendix

A SαβRE Binary File Format

This appendix describes the binary file format used by the newly created SαβRE module of AMPX. It is used for storing the α "F Factors" and β CDFs used for the direct $S(\alpha, \beta)$ method implemented in KENO. In addition, it stores some supplementary data that is used for sizing the arrays.

The structure of the Fortran-formatted little-endian binary file is given in Table A.1. In this table "DP" stands for double precision.

Table A.1: Data file format for SαβRE binary file.

Number of Records	Data Type	Number of Values	Data
1	Integer	2	No. of Betas - *nB* No. of F Factors - *nFF*
1	DP Real	*nFF*	Alphas
nB	DP Real	1 + *nFF*	Beta F Factors for this Beta
1	Integer	2	No. of SCT Betas - *nBsct* No. of SCT F Factors - *nFFsct*
1	DP Real	1	SCT Energy Cutoff - *eSCT*
1	DP Real	*nFFsct*	SCT Alphas
nBsct	DP Real	1 + *nFFsct*	SCT Beta F Factors for this Beta
1	Integer	1	No. of Incident E. - *nEin*
1	DP Real	*nEin*	Incident Energies
2 * *nEin*	Integer DP Real	1 2 * *nBein*	No. of Betas - *nBein* Betas CDFs

Vita

Shane Hart was born in Toronto, Ontario, Canada, to parents Peter Hart and Pamela Peterson-Hart. He is the oldest of three children; brother Alexander Hart, and sister Rebecca Hart. He originally attended Cornation Public School in Oshawa, Ontario, before moving to Burketon and attending Eniskillen Public School. He later graduated on to M.J. Hobbs Senior Public School in Hampton, Ontario and finally Cartwright High School in Blackstock, Ontario. After graduation, he was awarded a scholarship to attend the brand new University of Ontario Institute of Technology in Oshawa, Ontario, where he studied Nuclear Engineering. After graduating, he went to work for Atomic Energy of Canada Limited in Mississauga, Ontario in the Reactor Physics Branch. After less than two years there, he had the desire to attend graduate school and approached Dr. G. Ivan Maldonado at the University of Tennessee. He obtained his Masters of Science in May 2010 and decided to continue on to work on his Doctor of Philosophy degree. He has worked on a variety of reactor physics related projects both at AECL and ORNL in pursuit of his educational goals.